Efficient and Ultra Low Mass Harmonic Radar Transponders for Insect Tracking Applications

by

Ramin Ala

Bachelor of Science in Electrical Engineering, University of Isfahan, 2007
Master of Science in Electrical Engineering, K.N. Toosi University of Technology, 2010

A DISSERTATION SUBMITTED IN PARTIAL FULFILLMENT OF THE REQUIREMENTS FOR THE DEGREE OF

Doctor of Philosophy

In the Graduate Academic Unit of Electrical and Computer Engineering

Supervisors:	Chris Rouse, Ph.D., P.Eng., Electrical and Computer Engineering Bruce Colpitts, Ph.D., P.Eng., Electrical and Computer Engineering
Examining Board:	Brent Petersen, Ph.D., P.Eng., Electrical and Computer Engineering Zahra Khatami, Ph.D., P.Eng., Electrical and Computer Engineering Shabnam Jabari, Ph.D., P.Eng., Geodesy and Geomatics Engineering
External Examiner:	Weimin Huang, Ph.D., P.Eng., Electrical and Computer Engineering Memorial University of Newfoundland

This dissertation is accepted by the
Dean of Graduate Studies

THE UNIVERSITY OF NEW BRUNSWICK

November, 2023

© Ramin Ala, 2023

Abstract

The design, construction, and performance of a harmonic radar transponder with a total mass of approximately 530 µg is presented. The transponder is intended for insect tracking applications and consists of very fine wire and a small Schottky diode. It is designed for fundamental and harmonic frequencies of 10 GHz and 20 GHz, respectively. Compared to existing harmonic radar transponders, this transponder is easy to construct because the loop inductor can be implemented with a simple bend in the dipole conductor without degrading performance. Through careful design optimization, the conversion loss of the transponder is not impacted by the measures taken to minimize its mass. The expected harmonic power versus the transmitted power is estimated based on the link analysis between the transmitter and receiver of the radar, with the link analysis itself being performed via calculation, harmonic balance simulation, and full-wave simulation. The link analysis simulation predicted a received power of -66.4 dBm for a transmitted power of +22 dBm and a range of 2.4 m. The measured received power level at the harmonic frequency, obtained from the broadside of the transponder in an anechoic test chamber, is approximately -70 dBm, which agrees well with the link analysis. Simulated and measured transponder radiation patterns are also compared and show good agreement. A transponder with reduced mass compared to previous generations enables the tracking of smaller insects without diminishing their lifespan or undermining their natural flying abilities at various altitudes and ranges. The interplay between power at the fundamental

and harmonic frequencies within the transponder depends on the properties of the connected diode. By conducting simulations, the relationship between these powers can be determined and formulated, enabling the optimization of the transponder's performance. Given the fragile structure of a low mass transponder, it is crucial to assess the impact of transponder deformation on detection performance. The extent of deformation impacts the transponder's performance, manifesting in both positive and negative effects. However, it is worth noting that the deformed transponder exhibits altered polarization, which has the potential to enhance its performance.

Dedication

★ Ayda ❤ Beeta ☺ ★

Acknowledgements

I wish to express my heartfelt gratitude to my supervisors, Dr. Chris Rouse and Dr. Bruce Colpitts, for their unwavering support and invaluable guidance throughout my journey toward obtaining this degree. Dr. Colpitts served as my supervisor during the initial two years, and I am grateful for the opportunity to have had Dr. Rouse join as my co-supervisor for the latter two years.

The initial phase of my study delves into both broad, overarching experiences and personal, unique moments. The emergence of the COVID-19 pandemic significantly constrained students' access to laboratories, presenting an unprecedented challenge. On a more personal note, I was also blessed with the arrival of my daughter during this period. These challenges undoubtedly posed limitations to my progress, and I am deeply appreciative of Dr. Colpitts for his unwavering advice and profound understanding throughout this period.

In the ensuing two years, I dedicated myself to rigorous research endeavors, and the inclusion of Dr. Rouse proved to be a substantial boon. Our collaborative endeavors significantly advanced my degree's successful completion. Candidly, I must acknowledge that my graduation would not have been attainable without the profound scientific and technical guidance generously provided by Dr. Rouse.

I would also like to thank Dr. Brent Petersen for his support and valuable feedback. My thanks extend to my lab mates who made the work environment a joy: James McMurtrie and Quinn Selby in our room and Sarah Siddiqua, Alex Colpitts,

Nick Kozma, and Amit Uppin next door. I enjoyed talking and collaborating with them and have learned a lot from them.

Lastly, I extend my gratitude to my parents back in my home country, as well as my wife and daughter who have been by my side here. They are truly my greatest treasure.

Table of Contents

Abstract ii

Dedication iv

Acknowledgments v

Table of Contents vii

List of Tables x

List of Figures xi

List of Abbreviations and Symbols xv

1 Introduction 1

1.1 Contributions 2

1.2 Organization of the Thesis 3

2 Background 5

2.1 Harmonic Radar 5

2.1.1 Harmonic Radar Transceivers 6

2.1.2 Transponders 11

2.2 Transponder Performance Metrics and Assessment Methods 15

2.3 Literature Review 17

3 An Extra Low-mass Harmonic Radar Transponder for Insect Tracking Applications 23

3.1 Introduction . . . 23

3.2 Transponder Model and Design . . . 24

3.3 Link Analysis for a Harmonic Radar System . . . 27

3.4 Experiment and Discussion . . . 33

3.4.1 Specifications of the Transponder . . . 33

3.4.2 Measuring the Broadside Harmonic Amplitude . . . 35

3.4.3 Measuring Radiation Pattern . . . 37

3.4.4 Transponder Axial Ratio . . . 39

3.4.5 Estimated Maximum Detection Range . . . 40

3.5 Conclusion . . . 42

4 Diode Analysis and Performance Evaluation in Transponders 44

4.1 Introduction . . . 44

4.2 Two Regions of Transponder Operation . . . 45

4.2.1 Transponder Conversion Loss versus Drive Level . . . 47

4.2.2 Diode SPICE Parameters and Knee Point . . . 47

4.3 Transponder Performance in the High Power Region . . . 50

4.4 Schottky Diode Selection Criteria . . . 54

4.5 Design of Experiment . . . 57

4.5.1 A Suitable Range for each SPICE Parameter . . . 57

4.5.2 Generating the Database by Simulation . . . 58

4.5.3 Implementing DOE using R . . . 59

4.6 Conclusion . . . 61

5 The Impact of Transponder Deformation on Detection Performance 62

5.1 Introduction . . . 62

5.2 Definition and Modeling of the Bend 64
5.3 Deformation and Impedance Matching 64
5.4 Deformation and the Radiation Pattern 67
5.4.1 Deformation and Transponder Polarization 68
5.4.2 A Sharp Bend at one Arm and the Radiation Pattern 69
5.4.3 A Curved Bend at one Arm and the Radiation Pattern 75
5.4.4 Bends at both Arms and the Radiation Pattern 77
5.5 Measurement 79
5.6 Conclusion 83

6 Conclusion **84**
6.1 Future Work 86

Bibliography **100**

A Design of Experiment: Implementing R Code **101**

Vita

List of Tables

3.1 Comparing some harmonic transponders. 24

3.2 General shape of the radiation pattern in terms of dipole length. . . . 26

3.3 SPICE parameters of the MACOM MA4E2501L-1290 diode. 30

3.4 Summary of steps in the harmonic radar transceiver link for a range of $R = 2.4\,\mathrm{m}$. 32

4.1 SPICE parameters of the Skyworks Schottky diode, SMS7630-079LF. 52

4.2 Key SPICE parameters for some selected Schottky diodes and two selected ranges for DoE. 58

4.3 The dataset of CL versus diode SPICE parameters for DOE analysis. 59

5.1 Impedances at f_0 and f_h and resulting CL for a mildly deformed transponder ($L = 9$ mm, $R = 0.05$ mm, $\theta = 45°$). 67

5.2 IF Bandwidth and corresponding noise floor. 81

List of Figures

2.1 Diagram of a typical harmonic radar link where the transponder's non-linearity generates harmonics in the received power. 7

2.2 A harmonic radar transponder 13

3.1 Transponder balanced and unbalanced equivalent circuits. 29

3.2 Simulation of matching between dipole and diode: (a) schematic, (b) reflection coefficient plot. 30

3.3 The harmonic balance simulation: (a) schematic, (b) magnitude of the first and second current harmonics. 31

3.4 Structure of transponder (a) dimensions, (b) loop and soldered diode, and (c) final transponder stuck on the scaled paper. 34

3.5 Testing setup (a) diagram (b) a transponder mounted on styrofoam (c) measurement setup. 36

3.6 Diagram of a typical harmonic radar link. 38

3.7 Normalized radiation pattern of transponder in two planes (a) elevation (b) azimuth. 39

3.8 Total radiation pattern measured at three different transmitted power levels. 40

3.9 Simulation result for the axial ratio at f_0 and f_h at the elevation plane. 41

3.10 Measured and simulated received power versus the transmitted power for a constant range of $R = 2.4\,\mathrm{m}$. Symbols on the plots are measured and simulated points. CL is also plotted in blue. 42

4.1 Received power as a function of transmitted power, with a dashed green line extending across regions. 46
4.2 CL plotted for two different V_{j} values in relation to a) V_{oc} and b) V_{oc} normalized by the corresponding V_{j} values. 48
4.3 Absolute value of the derivative of the CL over the V_{oc} for two values of V_{j}. 49
4.4 A SMS7630 schottky diode mounted on a 50 Ω microstrip transmission line a) testing board b) simulation setup. 51
4.5 Amplitude of the harmonic at 20 GHz versus the RF power at 10 GHz for the circuit in Figure 4.4a. 52
4.6 Simulated and measured derivative of diode harmonic power with respect to input RF power. 53
4.7 Simulated and measured CL against input power. 54
4.8 Transponder CL against V_{oc} for two values of a) C_{j0} b) V_{j} c) I_{s} d) R_{s} e) L_{s} f) C_{p}. 56
4.9 Relative importance of diode SPICE parameters in CL derived from a) range 1 b) range 2. 60

5.1 Modelling a simple bend in the transponder arm a) definition of three bend parameters, R, θ, and L b) a sharp bend with $\theta = 135°$ c) a complete curved bend with same θ. 65
5.2 Impedance characteristics of an undistorted transponder, where the blue and red lines represent the real and imaginary components, respectively. 66
5.3 Comparison of impedance characteristics between an intact transponder (blue lines) and a slightly deformed transponder (red lines). . . . 67
5.4 Comparison of impedance characteristics between an undistorted transponder (blue lines) and a highly deformed transponder (red lines). 68

5.5 Transponder featuring a sharp arm bend with bend parameters: $R =$ 0.05 mm, $L = 6$ mm, and $\theta = 90°$. 70
5.6 Elevation plane directivity pattern of a transponder with a sharp bend, utilizing radar antennas with linear polarization; dashed line is the non-deformed pattern. 71
5.7 Elevation plane directivity pattern of a transponder with a sharp bend, employing LHCP antennas in the radar system; dashed line is the non-deformed pattern. 72
5.8 Simulated axial ratio of a deformed transponder at two orthogonal elevation planes using LHCP radar antennas. The left and right columns depict frequencies f_0 and f_h, respectively. 73
5.9 Azimuth plane directivity pattern of a transponder featuring a sharp bend, with a linearly polarized radar antennas; dashed line is the non-deformed pattern. 74
5.10 Azimuth plane directivity pattern of a transponder with a pronounced bend, utilizing LHCP antennas in the radar system; dashed line is the non-deformed pattern. 75
5.11 Transponder featuring a curved arm bend with bend parameters: $R =$ 2.86 mm, $L = 9$ mm, and $\theta = 180°$. 75
5.12 Elevation plane directivity pattern of a transponder with a curved bend, employing a linearly polarized radar antennas; dashed line is the non-deformed pattern. 76
5.13 Elevation plane directivity pattern of a transponder featuring a curved bend, with radar employing two LHCP antennas; dashed line is the non-deformed pattern. 77
5.14 Transponder with bends at each arm, characterized by bend parameters: $R = 1.5$ mm, $L = 6$ mm, and $\theta = 90°$. 77

5.15 Elevation plane directivity pattern of a transponder featuring a single bend at each arm, utilizing linearly polarized radar antennas; dashed line is the non-deformed pattern. 78
5.16 Elevation plane directivity pattern of a transponder featuring a single bend at each arm, with two LHCP antennas on the radar system; dashed line is the non-deformed pattern. 79
5.17 Simulated axial ratio of a deformed transponder with bends at each arm, evaluated at the elevation plane. The plot depicts circular polarization at multiple points. 80
5.18 Placing the transponder on a sheet of paper to mitigate the impact of styrofoam on the radiation pattern. 81
5.19 Radiation pattern measurement for a deformed transponder: (a) Deformed transponder ($L = 7$ mm, $R = 1$ mm, and $\theta = 90°$) (b) Elevation pattern in two perpendicular planes, including simulation (dashed). . 82

List of Abbreviations and Symbols

ADS	Advanced Design System
ATC	Anechoic Test Chamber
AWG	American Wire Gauge
c	Speed of Light
cm	Centimetres
CL	Conversion Loss
CST	Computer Simulation Technology
C_{j}	Junction Capacitance
C_{j0}	Zero-bias Junction Capacitance
C_{p}	Parasitic Capacitance
dB	Decibels
dBi	Decibels Relative to an Isotropic Radiator
dBm	Decibels Relative to a Milliwatt
DC	Direct Current
DOE	Design of Experiment
f_0	Fundamental Frequency
f_{h}	Harmonic Frequency
FOM	Figure of Merit

GHz	Gigahertz
Hz	Hertz
HPBW	Half-power Beamwidth
IF	Intermediate Frequency
I_{s}	Saturation Current
k	Boltzmann Constant
kHz	Kilohertz
LHCP	Left Hand Circular Polarization
LPF	Low-Pass Filter
L_{s}	Parasitic Inductance
m	Metres
MDS	Minimum Detectable Signal
mm	Millimetres
mW	Milliwatts
MHz	Megahertz
µW	Microwatts
µg	Micrograms
PCB	Printed Circuit Board
Radar	Radio Detection and Ranging
RBW	Resolution Bandwidth
RCS	Radar Cross-section
RF	Radio Frequency
RFID	Radio-frequency Identification
R_{s}	Series Resistance
RHCP	Right Hand Circular Polarization
RX	Receiver

SMD	Surface Mount Device
SNR	Signal-to-Noise Ratio
SPICE	Simulation Program with Integrated Circuit Emphasis
TX	Transmitter
VNA	Vector Network Analyzer
V_{oc}	Antenna Open-circuit Voltage
V_{j}	Junction Potential
W	Watts
σ_{h}	Harmonic Radar Cross-Section

Chapter 1

Introduction

Harmonic radar is a type of radar in which the harmonics of a transmitted signal are detected. Semiconductor devices, such as diodes, exhibit nonlinear behavior that produces harmonics of the excitation signal. This enables the detection and tracking of objects that would otherwise be indistinguishable from background clutter [1] and can be achieved with a relatively straightforward system architecture that does not require complex signal processing, as described in [2].

Harmonic radar systems have limitations that impact their performance and effectiveness. They have a limited range, typically a few hundred meters, making them unsuitable for long-range tracking. Interference is another concern as they can be affected by electronic devices operating in the same frequency range, compromising accuracy and reliability. The transponders employed in harmonic radar systems also demonstrate a limited lifespan and fragility, thereby diminishing the overall durability of the transponder. This fragility makes transponders less suitable for rugged environments. Additionally, transponder visibility and orientation affect the radar system's ability to accurately detect and track targets. The high mass of transponders also makes them less suitable for insect tracking, their primary application. Finally, environmental conditions like heavy rain, dense foliage, or physical obstacles can impact

the performance of harmonic radar systems [3]. In this work, an efficient harmonic radar transponder is presented with a significant emphasis on achieving an ultra-low mass.

Section 1.1 outlines the contributions made by the thesis, encompassing three distinct aspects. Furthermore, Section 1.2 provides a brief overview of the subsequent chapters of the thesis and their interrelationships.

1.1 Contributions

This section introduces the three key areas of focus that this study seeks to address:

I. Minimizing the Overall Mass of the Harmonic Radar Transponder.

II. Enhancing Transponder Efficiency via Diode Selection Optimization.

III. Investigation into the Impact of Deformation on Harmonic Radar Transponders.

The primary focus of this research is the advancement of an ultra-low mass harmonic radar transponder for insect tracking applications that maintains a high level of performance. The transponder was constructed with copper wire of AWG#44 and a Schottky diode with a footprint of 0201, resulting in a total mass of approximately 530 µg, stands out as the lightest option currently known that maintains a high level of performance in terms of harmonic conversion efficiency: with an available power of approximately -20 dBm, a conversion loss (CL) of 4.5 dB was achieved, demonstrating an impressive performance for a passive transponder. A part of the contribution lies in the area of characterization and measurement, where a novel technique is employed to determine the transponder's radiation pattern. Instead of reporting separate radiation patterns, our proposed technique derives the transponder's total radiation pattern. Throughout the study, the measurements exhibited consistent alignment

with the simulations. Reducing the total mass of the transponder by 37% will facilitate the tracking of insects with masses in the range of a few milligrams, which are significantly smaller than what current state-of-the-art radio transmitters can accommodate [4]. The possibility and challenges associated with designing such a transponder are briefly studied in [5].

Measurements conducted on the developed transponder show a specific relationship between its harmonic power and the illuminated power density: by amplifying the transmitted power by 1 dB, the received harmonic power rises by 2 dB and 1 dB at the low and high transmitted power levels, respectively. This characteristic is thoroughly examined to identify the underlying factors that contribute to it, offering the potential for optimizing transponder performance. Additionally, by directing attention to the diode element within the transponder, new knowledge is gained regarding how to select the most suitable diode for optimal transponder functionality.

Finally, the influence of potential deformations on a specially designed low-mass transponder was examined [6]. This study investigated how deformation affects both the matching performance and the radiation pattern of the transponder. The findings shed light on how these alterations due to deformation impact the detectability of the low-mass transponder, providing valuable insights in this regard.

1.2 Organization of the Thesis

This thesis is organized into six chapters and one appendix. The subject areas under consideration and the relevant contributions resulting from these research efforts are presented in Chapter 1. Chapter 2 provides background information pertaining to harmonic radar systems and transponders. In the subsequent chapters, it is assumed that the reader is familiar with this background material in addition to the fundamentals of microwave engineering and antenna theory. A review of the most

significant and relevant literature is also provided.

Chapter 3 presents the design, construction, and performance of an ultra-low mass harmonic radar transponder, developed for insect-tracking purposes. The chapter explores the simulation of the transponder's *CL*, which is then verified through measurements. Furthermore, the radiation pattern of the transponder is both simulated and measured to gain insights into its directional characteristics. This chapter is largely based on our published paper in the IEEE Transactions on Radar Systems [4].

Chapter 4 explores the diode in-depth, studying the transponder's behavior under different power density conditions and analyzing the impact of various diode parameters on its performance. The Design of Experiment (DOE) method is employed to quantify the significance of these parameters.

Chapter 5 explores the ramifications of transponder deformation on detection performance. These deformations can easily occur when the transponder is attached to an insect, particularly when the antenna is constructed with very thin wire. By examining the simple types of deformation on the impedance and radiation pattern, valuable insights can be gained into the detectability of a deformed transponder.

Chapter 6 concludes the thesis, summarizing the most significant findings from Chapters 3, 4, and 5. Additionally, it discusses potential avenues for future research in each of the respective research areas.

Chapter 2

Background

This chapter introduces the fundamental concepts of harmonic radar systems and transponders. Wherever possible, the information is presented chronologically, offering a historical perspective on the topic. In light of the significant research conducted in this field, a comprehensive survey of the relevant scientific literature is provided in section 2.3.

2.1 Harmonic Radar

Harmonic radar is a technology that utilizes the principles of radar to track and locate objects, specifically small or elusive targets such as insects, birds, or even miniature drones. It operates by exploiting the unique harmonic signature or response generated by both static and moving targets when it interacts with a radar signal [7].

The history of harmonic radar is intertwined with the development of radar technology itself. The first successful radar (Radio Detection and Ranging) demonstration took place in 1935, led by Sir Robert Watson-Watt and his team in the United Kingdom. This innovation was further refined during World War II to serve as a method for aircraft detection and tracking [8].

The origins of nonlinear radar design and implementation can be identified as

early as 1976 when it was first utilized to detect metallic objects, like vehicles, that were concealed by foliage and situated in close proximity to the ground [9]. During the 1980s, researchers and scientists observed that by attaching reflective markers or miniature transponders to specific organisms such as insects or small birds, they could generate a harmonic response when exposed to radar signals. This enabled effective tracking and monitoring of these organisms using harmonic radar technology [10, 11]. Over the following decades, advancements in radar technology and miniaturization enabled the development of smaller and more sophisticated harmonic radar systems. These systems became increasingly capable of tracking smaller and more agile targets with greater precision and accuracy [12], allowing scientists to track the movement patterns and flight paths of insects, such as bees and butterflies. This technology contributed to a better understanding of insect migration, foraging habits, and pollination patterns.

Harmonic radar continues to be an active area of research and development. Scientists are working on improving the range, accuracy, and miniaturization of harmonic radar systems. The technology holds promise for various fields, including wildlife conservation, precision agriculture, and even potential applications in the emerging field of insect-sized robotics [13].

The majority of research endeavors are directed towards enhancing the performance of either the radar transceiver or the transponder. In the harmonic radar system, as the radar transceiver emits a signal and subsequently processes the echoed signal, the transponder generates harmonics through its nonlinear characteristics.

2.1.1 Harmonic Radar Transceivers

A harmonic radar system, similar to other radar systems, typically comprises several components: a transmitter (TX), antennas, receiver (RX), down-converter, filters, and a signal processing unit. A diagram illustrating a typical harmonic radar link

is shown in Figure 2.1. TX generates the radar signal at the fundamental frequency (f_0) and emits it into the surrounding environment. The associated transponder is specifically designed to efficiently receive the radar signal, generate the harmonic frequency (f_h), and efficiently re-radiate it. The harmonic radar transceivers consist of several modules aimed at enhancing the range and minimizing interference. To achieve this, the generated signal undergoes amplification and filtration before being emitted through the antenna. Thermal noise is the most significant noise source in harmonic radar systems, followed by self-interference. Hence, the filtering requirements in harmonic radar tend to be more aggressive [14]. It is important to note that the specific implementation and components of a harmonic radar system may vary depending on the application and desired performance. Nevertheless, the aforementioned structure provides a general overview of the key elements involved in tracking and locating targets using harmonic radar technology [8].

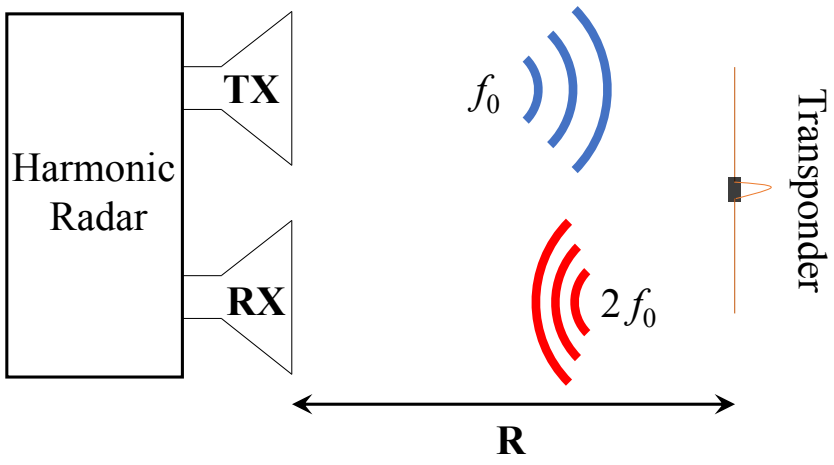


Figure 2.1: Diagram of a typical harmonic radar link where the transponder's nonlinearity generates harmonics in the received power.

Filters play a critical role in eliminating unwanted noise and interference from the received signal, thereby enhancing the clarity and accuracy of the radar system. In the case of using a single antenna for both transmitting and receiving, a diplexer is necessary, and it is crucial to either guarantee that the antenna possesses a minimum

bandwidth of one octave or is purposefully engineered to function optimally as a dual-frequency antenna.

An example of a compact microstrip antenna suitable for harmonic radar can be found in [15]. This particular antenna is designed to operate at frequencies of 3 GHz and 6 GHz. The compactness of this antenna comes at the expense of its gain, which is less than 4 dBi at each frequency. Generally, this level of gain is considered quite low for harmonic radar applications. Separate antennas for the TX and RX are commonly used to address challenges in designing a single antenna with sufficient bandwidth. Using two antennas also improves self-interference reduction.

The received signal is directed to RX, which captures the harmonic frequencies and converts them into an intermediate frequency (IF). Subsequently, the signal processing unit comes into play, analyzing and interpreting the received signals to extract relevant information about the transponder's position, speed, and direction. This unit may employ various algorithms and techniques for target tracking and localization.

The processed information is then conveyed to the user, allowing them to monitor and track the transponder or target in real-time. Additionally, the data can be recorded for subsequent analysis or scientific study.

A harmonic radar transceiver can be implemented using products from renowned manufacturers such as Furuno, a Japanese electronics company specializing in marine electronics [16], and companies like RECCO Technology, known for their portable solutions [17]. In certain studies, researchers have successfully constructed transceivers using readily available off-the-shelf components [18]. The choice between these options is typically determined by the specific application requirements and the available budget. One of the primary considerations in radar selection is deciding between a non-portable, large, and powerful system [18] versus a portable system that can be mounted on a drone [19] or carried by a human [20, 21]. This choice depends on various factors and requirements specific to the intended application.

A commonly used variant of harmonic radar is multitone radar. Multitone systems transmit multiple closely-spaced tones and receive both nonlinear mixing products and transmitted tones in the received signal. This method allows for further refinement and analysis of the received signals, enabling improved tracking and detection capabilities in certain scenarios [22].

A concise overview of the harmonic radar systems' terms and parameters is specifically essential for entomologists. The first parameter is the tracking range which is an important parameter in every radar system. Maximum tracking range ($R_{\max}$) refers to the maximum distance at which the radar can reliably detect and track a target. For unmodulated pulse radar systems with the pulse width of τ, the average power during the pulse is the peak transmit power (P_{t}). In this case, $R_{\max}$ depends on the radar TX antenna's gain (G_{t}), RX antenna's gain (G_{r}), minimum detectable received power ($S_{\min}$), and the target's radar cross-section (RCS) that is a measure of how reflective the target is to radar waves. Under the assumption of free-space as the transmission medium and the omission of losses related to components such as connectors, cables, and waveguides, the range equation is [14]

$$R_{\max} = \left[\frac{P_{\mathrm{t}} G_{\mathrm{t}} G_{\mathrm{r}} \lambda^2 \sigma_{\mathrm{t}}}{(4\pi)^3 S_{\min}}\right]^{1/4} \tag{2.1}$$

where σ_{t} is the RCS of the target and λ is the wavelength at the operating frequency. The next important parameter is the spatial resolution, which includes range and angular resolutions. Central to harmonic radar effectiveness is its precision in locating tagged insects [23]. In the context of an unmodulated pulse radar, the range resolution (Δ_{R}) is directly influenced by the radar's pulse width, τ [14]:

$$\Delta_{\mathrm{R}} = \frac{c\tau}{2} \tag{2.2}$$

where c is the speed of light. Considering tracking in the azimuth direction, the radar

angular resolution (Δ_ϕ), on the other hand, is a function of radar antenna Half-power Beamwidth (HPBW_ϕ) [14].

There is a trade-off between $R_{\max}$ and Δ_{R}. Since $S_{\min}$ is a function of minimum Signal-to-Noise Ratio ($\text{SNR}_{\min}$) and equivalent system noise temperature (T_{sys}) that represents the combination of all noise sources

$$S_{\min} = kT_{\text{sys}}B\,\text{SNR}_{\min} \tag{2.3}$$

in an unmodulated pulse radar, B is approximately proportional to $1/\tau$. Consequently, reducing τ leads to a decrease in $R_{\max}$, as indicated by Equation 2.1. Nonetheless, this reduction enhances the range resolution, as implied by Equation 2.2. Expressing the same idea in different terms, it can be stated that a smaller τ means a wider frequency bandwidth. However, a wider bandwidth results in increased system noise. Consequently, this trade-off leads to a reduction in the system's SNR, and subsequently, $R_{\max}$ is decreased. Because of the relationship between radar angular resolution and its HPBW, a narrow antenna beam enhances angular resolution. This improvement also translates to a higher SNR due to the higher gain of an antenna with a narrow beam. However, this enhancement comes with a trade-off: a narrower beam results in fewer pulses reaching the target for signal processing, and it necessitates the use of a larger antenna. In the context of a portable system, employing a narrow beam can pose challenges for manual tracking [24].

Harmonic radar systems are well-suited for tracking individual insects, rather than monitoring large groups. Similar to other radar systems, the capacity of a harmonic radar system to track multiple insects concurrently hinges on the intricacy of the tracking algorithm and the precision of localization parameters. Group tracking becomes feasible when insects are sufficiently spaced apart, signifying distinct targets. In such scenarios, and given sufficient processing power, the option for group tracking becomes viable [14, 25].

Harmonic radar systems serve a dual purpose: identifying and localizing tagged insects. The strength of their identification capability significantly outweighs their localization potential [26]. Illustratively, two instances can offer a preliminary gauge of harmonic radar systems' effectiveness in localizing tags. In one case, Tsai *et al.* conducted field experiments, showcasing the system's capacity to detect tagged objects up to 60 meters away with an accuracy of 1 m using a 1.75 W transmitting power [23]. In a separate investigation, the same accuracy was attained over a distance of 500 meters, leveraging a 1 kW transmitter and radar antennas featuring enhanced gain [12]. Both of these studies harnessed sophisticated radar algorithms to achieve their results. In these two examples, the disparity in the range is evidently attributable to variations in transmitted power. The equal resolution in these two cases can be attributed to factors like the radar pulse duration and the methodologies employed. For instance, the utilization of the pulse compression technique is exemplified in [12], whereas the code-positioning technique is implemented in [23].

2.1.2 Transponders

Transponders are another part of harmonic radar systems. Unlike conventional radars that detect a variety of distinct objects, harmonic radar systems focus on specialized targets. These targets are purposefully designed objects with the capability to produce harmonic(s) of the incoming signal. Harmonic radar transponders can be divided into two distinct categories based on their specific features and applications. Passive transponders do not require an internal power source and rely solely on the energy received from the incoming radar signal. These transponders reflect a harmonic signal back to the radar system, enabling the detection and tracking of the target. Passive transponders are generally lightweight, making them popular in insect-tracking applications. In contrast, active transponders incorporate an internal power source, such as a battery, to amplify and transmit the harmonic signal. This

results in a stronger response compared to passive transponders, allowing for longer detection ranges and improved tracking accuracy [27]. However, active transponders tend to be bulkier and heavier due to the additional components and power source, which can limit their practical applications in certain scenarios.

Passive harmonic radar transponders are constructed using a combination of electronic components, with a diode playing a crucial role in generating harmonic signals [28]. Figure 2.2 illustrates the simplest form of a transponder, which is also the lightest in weight. This figure clearly depicts the Schottky diode, dipole, and loop as the matching circuit. However, due to the simplicity of its structure, designed to reduce mass, this transponder suffers from efficiency issues. This limitation results in a reduced maximum detection range compared to a typical radar system. The transponder has a smaller harmonic radar cross-section (σ_{h}) compared to the RCS of an object with a similar shape and material. These inefficiencies are rooted in power losses caused by the mismatch between the diode and the dipole, the power loss during the conversion from f_0 to f_{h}, and the requirement for a minimum drive level [29].

The design process encompasses various essential stages. The first is selecting a diode capable of producing significant harmonic signals under relatively low drive levels. Considerations include low turn-on voltage and appropriate size for the intended application [30]. The transponder requires an optimized antenna that can receive the incoming radar signal and re-radiate a harmonic signal back to the radar system. The antenna design aims to achieve the best impedance match with the diode at two harmonically related frequencies [31]. Extra circuitry may be added to enhance the transponder's performance by improving power transfer between the antenna and diode. This can range from modifications in the antenna structure [32] to the inclusion of lumped element or microstrip matching circuits [33]. Another important consideration is the method of mounting the transponder on the carrier or object of

interest. This can involve various techniques, such as adhesive mounting, mechanical fastening, or integration into the target's structure.

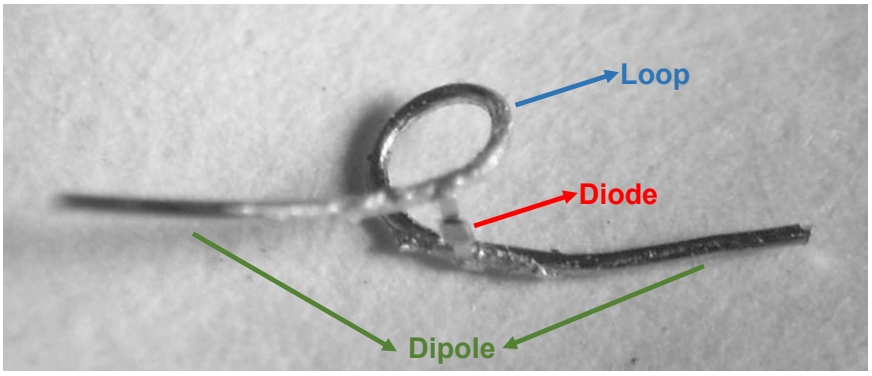


Figure 2.2: A harmonic radar transponder [34].
© [2004] *IEEE Transactions on Antennas and Propagation.*

In the case of a harmonic radar transponder, the relationship between the incident and reradiated power density exhibits non-linearity. This non-linearity can be explained by the Shockley diode equation [35]:

$$i_{\mathrm{D}} = I_{\mathrm{s}}(e^{\frac{v_{\mathrm{D}}}{\eta V_{\mathrm{T}}}} - 1) \tag{2.4}$$

where i_{D} is the diode current, I_{s} is the saturation current, also known as scale current, V_{T} is the thermal voltage, n is the ideality factor, also known as the quality factor or emission coefficient, and v_{D} is the voltage across the diode, which is dependent on the characteristics of the signal transmitted by the radar system. Assuming a sinusoidal source with an angular frequency of ω_0

$$v_D = v_0 \cos(\omega_0 t) \tag{2.5}$$

if $e^{\frac{v_D}{nV_T}} \gg 1$, the forward diode current can be approximated as

$$i_{\mathrm{D}} = I_{\mathrm{s}} e^{\frac{v_{\mathrm{D}}}{nV_{\mathrm{T}}}}, \tag{2.6}$$

which can be approximated using the Taylor series expansion as

$$i_{\mathrm{D}} = \sum_{k=0}^{\infty} a_k v_{\mathrm{D}}^k = a_0 + a_1 v_{\mathrm{D}} + a_2 v_{\mathrm{D}}^2 + \dots \tag{2.7}$$

where a_k is the Taylor series coefficient.

By substituting the expression from Equation 2.5 into Equation 2.7, i_{D} can be expressed as:

$$\begin{aligned} i_{\mathrm{D}} &= a_0 + a_1 v_0 \cos(\omega_0 t) + a_2 v_0 \cos^2(\omega_0 t) + a_3 v_0 \cos^3(\omega_0 t) + \cdots \\ &= a_0 + \frac{1}{2} a_2 {v_0}^2 + \left(a_1 v_0 + \frac{3}{4} a_3 {v_0}^3 \right) \cos(\omega_0 t) + \frac{1}{2} a_2 {v_0}^2 \cos(2\omega_0 t) + \\ &\frac{1}{4} a_3 {v_0}^3 \cos(3\omega_0 t) + \cdots \end{aligned} \tag{2.8}$$

This demonstrates the relationship between the diode current and its voltage at both f_0 and f_{h}, assuming a sinusoidal voltage source is applied directly across the diode.

When it comes to generating harmonics using a diode, the *CL* is defined as the disparity between the output power at the harmonic frequency and the input power at the fundamental frequency.

$$CL = P_0 - P_{\mathrm{h}} \tag{2.9}$$

where both powers are in dBm.

The polarization of the transponder and its relation to radar polarization significantly impact its detectability. The axial ratio, denoted as AR, describes the polarization characteristics of an antenna, measuring the ellipticity of its radiation pattern and indicating its ability to transmit or receive circularly polarized signals. It is defined as the ratio between the maximum and minimum field strengths of the circularly polarized wave. Typically expressed in dB, a low axial ratio signifies superior circular polarization performance, while a high axial ratio suggests the presence of significant linear polarization components. Circular polarized antennas are commonly

categorized by axial ratios under 3 dB [36].

Given that the harmonic radar formulation involves substituting σ_{h} for σ_{t}, the transponder's specifications impact some of the radar system parameters like $R_{\max}$. Optimizing the performance of a harmonic radar transponder becomes synonymous with maximizing σ_{h}. This study centers around the transponder component of a harmonic radar system, with a specific emphasis on the dual objectives of maximizing σ_{h} while concurrently minimizing the overall mass.

2.2 Transponder Performance Metrics and Assessment Methods

The performance of a transponder must be adequately assessed through calculation, simulation, or standardized testing methods to ensure it will satisfy the requirements of the associated harmonic radar implementation. This process entails verifying the generation of harmonic signals, assessing reflection levels, and ensuring compatibility with the radar system. The maximum detection range is generally evaluated during this stage.

Enhancing the design and evaluating the effectiveness of harmonic transponders presents a measurement challenge due to the absence of a suitable location to connect a measurement cable to the transponder antennas [37]. This challenge arises from the small size of transponders and their impedance mismatch with conventional $50\,\Omega$ RF systems. Similarly, due to the aforementioned challenges, it becomes difficult to measure the impedance matching of these transponders with nonlinear loads. The radiation pattern of the transponders can often be measured using the intermodulation response technique, as described in [38]. It can also indirectly indicate the level of matching between the antenna and the diode.

Defining a Figure of Merit (FOM) for the detectability of a transponder is use-

ful in assessing its effectiveness and could be used for optimization purposes. Unlike a conventional radar target, which is characterized by the RCS, the concept of RCS is not applicable to a harmonic radar transponder due to its internal frequency converter. Harmonic radar cross-section, σ_{h}, and nonlinear cross-section are interchangeable terms that effectively illustrate both the non-linearity of the transponder and the power loss attributed to frequency conversion [39, 40]. Alternatively, the *CL* or conversion efficiency could be reported for harmonic transponders [41, 42]. It is important to note that these parameters, like RCS, exhibit significant variations with frequency. Harmonic transponder performance is also influenced by the incident power density and operating frequency [43], making their characterization more complex.

Regardless of the chosen FOM, it is important to report it in relation to an appropriate input parameter. One option is to use incident power density, as it allows for easy comparison of transponder performance regardless of radar specifications and range. Selecting TX power may result in a more straightforward interpretation, but it would require additional calculations to convert the values and ensure comparability. Regardless, when comparing the FOM of transponders, it is important to ensure that the comparison is made under similar power conditions. This means that the transponders should be evaluated and compared using the same drive levels to accurately assess their performance.

The most practically valuable method for testing and evaluating a transponder is to measure its maximum detectable range both in a controlled field environment and when the transponder is carried by an insect [44]. It should be noted that the ultimate achievable range is contingent upon the capabilities of both the radar transceiver and the transponder. This approach allows for evaluating the transponder's performance under realistic conditions and assessing its effectiveness in real-world scenarios. By conducting range tests in the field and specifically examining the transponder's per-

formance when attached to an insect, researchers can obtain valuable data on the transponder's functionality, reliability, and overall effectiveness [45]. This testing method also enables researchers to assess the migratory and foraging movements of the species under test [46].

Alternatively, testing can be conducted in a regular room [47], but for more accurate measurements, an anechoic test chamber (ATC) is often utilized [38]. An ATC is specifically designed to simulate free-space conditions by minimizing unwanted interactions with the surroundings. It achieves this by absorbing or diffusing reflections of electromagnetic waves, thereby reducing interference and providing a controlled testing environment. However, it is important to note that the absorption properties of RF absorbers used in an ATC are optimized for a specific frequency range. This means that the ATC has a limited range of frequencies over which it can effectively absorb and dissipate electromagnetic waves. The specific frequency range of an ATC depends on the design and characteristics of the RF absorbers employed within the ATC. In addition to the frequency limitation, the ATC's limited space imposes a constraint on the range.

2.3 Literature Review

Radio transmitters are getting smaller and offer much better performance than radar solutions. As a result, harmonic radar is best suited to applications that involve animals and insects that are far too small for even state-of-the-art radio transmitters. In the case of insects, the transponder must have an extremely low mass so as not to significantly affect their behavior and mobility [48]. The maximum mass that insects can carry depends on the season because during periods of high activity, their body mass tends to decrease, thus reducing their carrying capacity [49]. Optimal transponder design involves striking a balance between low mass, high fundamental-

to-harmonic conversion efficiency, and ease of fabrication.

Existing harmonic radar transponders have a mass of approximately 1 mg and higher. Capaldi *et al.* reported a transponder mass of 800 µg using a dipole and diode structure, which was used to track honeybees within a range of 700 m [50]. Although the information needed to assess transponder efficiency, *e.g.*, the transmitted power and frequency, was not provided, the achieved mass is impressive. The same mass of 800 µg was achieved by connecting 8 cm of the super elastic nitinol wire to a Schottky diode using UV-activated adhesive. The resulting transponder was light enough to mount on Tephritid fruit flies [51]. A mass of 800 µg was also achieved for a 9.41 GHz transponder using AWG#42 wire and a relatively bulky diode [52]. In [34], a transponder mass of approximately 3 mg was achieved with a similar structure but thicker wire. A more complicated structure consisting of a patch antenna printed on a substrate and with a mass of 20 mg was presented in [23] for tracking bees. In [53] a printed bow-tie antenna was selected for a better matching to the diode impedance, resulting in a 20 mg transponder for snail tracking. Milanesio *et al.* combined two dipoles and diodes in a cross configuration to make a dual-polarized transponder that weighs approximately 12 mg [18]; this was estimated from the length, thickness, and material of the wire, as well as the mass of the diode, which is summarized in [5].

Developing a detailed model for the transponder enables both structural and performance optimization. A key performance metric is the ratio of re-radiated power density at the harmonic frequency to the incident power density at the fundamental. This depends on the antenna impedance and electrical characteristics of the diode, the latter of which are typically summarized in the corresponding SPICE model. Rasilainen *et al.* derived an analytical equation using equivalent circuits for the diode and antenna that yields the harmonic response in terms of the transponder antenna's received power [54]. In another work, a printed transponder equipped with a matching circuit was analytically modeled to derive the conversion efficiency from f_0 to

$f_h = 2f_0$, defined as power at f_h divide by power at f_0. Numerical results were also compared with harmonic balance simulations performed in PathWave Advanced Design System (ADS) [55]. In [56], Lavrenko *et al.* derived an equation to relate the transponder output current in terms of a voltage source as an input signal. The resulting exponential function can then be explicitly solved in both the small- and large-signal regimes using the Lambert function. A simplified approach that considers the Schottky diode as a complex load is presented in [57], and the transponder conversion efficiency is expressed in terms of dipole and diode impedances. The effect of the dipole arm ratio and wire thickness on the impedance, as well as the bending of the arms on the radiation pattern, were examined in [6] by full-wave simulation.

In practice, the orientation of the transponder relative to the incident electromagnetic wave is unknown, which raises the need for acquiring the radiation pattern. However, due to the lack of a measurement port, conventional radiation pattern measurement methods are not applicable to the transponder. An alternative technique based on intermodulation response can be derived from a similar method used to measure the radiation patterns of Radio-frequency Identification (RFID) transponders [58]. This technique was suggested by Rasilainen *et al.* to measure the individual radiation patterns of a transponder at f_0 and f_h [37].

Although insect tracking remains a primary application of harmonic radar, the versatile nature of the technology has led to successful implementations in a wide range of fields. For example, harmonic radar has demonstrated effectiveness in detecting RF surveillance equipment [59], enabling remote temperature sensing [60], monitoring human vital signs [61], supporting healthcare applications [62], and even making valuable contributions to the automotive industry [63]. These diverse applications highlight the adaptability and potential of harmonic radar technology beyond its initial scope, paving the way for further innovations and advancements in various sectors.

To formulate a range equation tailored to harmonic radar systems, one can adopt the conventional radar range equation with the alteration that σ_{h} is employed in place of RCS. This alteration allows the calculation of the harmonic radar's maximum range, denoted as $R_{\max}$ [34, 64].

$$R_{\max} = \left[\frac{P_{\mathrm{t}} G_{\mathrm{t}} G_{\mathrm{r}} \lambda_{\mathrm{h}}^2 \sigma_{\mathrm{h}}}{(4\pi)^3 P_{\mathrm{r,min}}} \right]^{1/4} \tag{2.10}$$

where G_{t} and G_{r} represent the transmit and receive antenna gains of the harmonic radar, respectively, the wavelength at f_{h} is denoted as λ_{h}, and $P_{\mathrm{r,min}}$ is the minimum detectable power by harmonic radar transceiver.

Selecting the transmitting and receiving frequencies is of utmost importance in harmonic radar systems. When choosing the transmitting frequency, the designer needs to take into account various factors, such as the availability of components, the feasibility of designing microwave components like filters and antennas, and the frequency allocation regulations specific to the operating area [65]. Short-range communication applications, like inventory management, often employ low-frequency systems. Conversely, higher frequency systems, such as UHF or microwave frequencies, offer an extended detection range [66]. These considerations are critical to ensure the proper functioning and regulatory compliance of the radar system. Different frequency bands are selected for the construction of harmonic radar and transponders based on their application. These bands include UHF [67, 68], L [69], S [70, 71], C [72], and most prominently, the X band [73]. X band is popular for several reasons. It enables the development of compact and portable radar systems, making it ideal for insect-tracking applications [74]. Additionally, it exhibits reduced susceptibility to interference from atmospheric conditions, enhancing radar system reliability and performance in diverse weather conditions [75]. Lastly, X band benefits from well-regulated frequency ranges, ensuring compatibility and availability of resources for harmonic radar applications [76]. Particularly, its application in marine radar proves

to be highly beneficial.

In certain scenarios, there is a need for a broad operating bandwidth [77] or multi-band harmonic radar systems [78] in order to encompass the entire range of frequencies used in a given application. In [79], a radar antenna is demonstrated, capable of simultaneous detection and tracking of three transponders using harmonic Doppler radar. Having a transponder design with a broader bandwidth can also be beneficial in single-frequency applications as it mitigates performance issues caused by frequency drift resulting from manufacturing tolerances. However, it is important to note that achieving a wideband structure generally increases complexity and size.

While there have been a limited number of studies on radars designed to track intermodulation tones [80], the majority of research has focused on the harmonics of the transmitted signal. The second harmonic is generally selected [81, 82] because it is usually the strongest harmonic returned from the transponder, but the third or even fourth harmonics are sometimes of interest and examined [83, 84].

Gaining a comprehensive understanding of the diode's characteristics and performance is crucial for optimizing the performance of the transponder. Schottky diodes are commonly used due to their fast switching speed. They are often employed in applications such as harmonic radar, mixers, and frequency multipliers. Their low forward voltage drop and minimal recovery time make them suitable for generating large harmonics [85]. Gu *et al.* [55] present the derivation of analytical models that demonstrate the correlation between the SPICE parameters of a diode and the conversion efficiency of transponders. Criteria for selecting diodes to optimize the detection range while minimizing the *CL* are discussed in [86]. Additionally, the study examines the impact of temperature on harmonic transponders based on Schottky diodes. For a comprehensive analysis of this topic, further investigations can be found in studies focusing on the design of harmonic mixers. Jiang *et al.* [87] presented a modeling approach that utilizes a Schottky diode for designing a harmonic mixer specifically

operating in the millimeter wave band. The study systematically investigates the performance of the diode's harmonic mixers across multiple frequency bands. To accomplish this, a three-dimensional model of the diode is developed, accounting for its material properties, and a co-simulation is conducted using electromagnetic field circuit software. Furthermore, the study includes a plot showcasing the relationship between the *CL* of the mixer and the frequency. The plot reveals an optimal point characterized by the lowest *CL*.

In recent studies, the Schottky diode has been replaced with alternative elements. For instance, to enhance performance, researchers in [88] substituted the diode with a field-effect transistor (FET). The designed transponder was evaluated at the fundamental and harmonic frequencies of 9.4 GHz and 18.8 GHz, demonstrating an improvement compared to the transponder utilizing a commercial Schottky diode. An intermodulation sensor was also developed utilizing reconfigurable graphene field-effect transistors (GFETs) [89].

In several studies, researchers attempted different antenna shapes to increase readability or reduce the total size of the structure. For instance, by simply bending the wire and making a W-shaped transponder, the shape of the wire allowed the transponder to be detected in more orientations [90]. In order to reduce the size of the transponder, a successful practice is to bend a long patch into four half-wavelength radiating elements, as demonstrated in [91], which is a capacitively coupled patch antenna. The design consideration of these antennas is provided in related studies [92].

However, when it comes to ultra-low-mass transponders, determining the precise shape of the antenna is challenging due to their inherent susceptibility to bending and deformation. Limited research has been conducted on examining such deformations. Nevertheless, the authors of [93] studied the influence of bending on the impedance matching of the transponder through full-wave simulation.

Chapter 3

An Extra Low-mass Harmonic Radar Transponder for Insect Tracking Applications

3.1 Introduction

In this Chapter, the design and performance of an extra low-mass transponder is presented. A simple arrangement consisting of a dipole and a diode has been chosen. Despite the efficiency challenges associated with this configuration, it still offers the advantage of the lowest mass. This structure was studied experimentally at both S- and X-band with TX output powers of 3 W and 10 W, respectively [94]. Here, the transponder consists of AWG#44 wire and a low-barrier Schottky diode with a footprint of 0201. The transponder performance is optimized by selecting a diode with low zero-bias Junction Capacitance (C_{j0}) and parasitic inductance (L_{s}) as well as optimizing the dipole length for a better impedance match. Table 3.1 summarizes the specifications of some harmonic transponders including their antenna structure, f_0, and total mass, along with proposed transponder, which exhibits the

lowest mass while maintaining low *CL*. Comparing the RF performance of the proposed transponder with a similar structure in this table reveals that the reduction in mass has not compromised its RF performance. In [34], a σ_h of 40 mm^2 was obtained. Comparing with the ideal σ_h of 320 mm^2 yields an estimated *CL* of roughly 9 dB; however, it is important to note that the antenna gain at f_h was assumed to be +3.8 dBi in [34], whereas, in this work, simulation results indicate a broadside antenna gain of -0.45 dBi at f_h. Combined with a broadside antenna gain at f_0 of approximately +2.5 dBi and the *CL* of 4.5 dB found here, our transponder exhibits a σ_h of approximately 40.7 mm^2—a slight improvement in σ_h and a significant reduction in mass. The transponder model and design are described in Section 3.2. In Section 3.3, transponder performance is estimated by a link analysis that accounts for all power loss and gain in the link considering a specific distance and transmitted power. Section 3.4 presents measurements performed in an ATC to determine the received harmonic amplitude and transponder radiation pattern. For validation purposes, measurements were performed under similar conditions to those of the link analysis simulations. Finally, Section 3.5 offers concluding remarks.

Table 3.1: Comparing some harmonic transponders.

Design	Antenna structure	f_0	Mass
[50, 51]	dipole	Not Specified	800 µg
[52]	dipole	9.41 GHz	800 µg
[34]	dipole	9.41 GHz	3 mg
[23]	microstrip patch	9.4 GHz	20 mg
[18]	cross dipoles	9.41 GHz	12 mg
This Work	dipoles	10 GHz	530 µg

3.2 Transponder Model and Design

The design of the transponder's antenna requires simultaneous consideration of several factors, including the characteristics of the attached diode, desired radiation

pattern(s), acceptable degree of complexity, and total mass. If mass reduction is the priority, the best option is a dipole with a loop that works as both a direct current (DC) path and a simple matching structure. The antenna should be conjugate matched to the diode at both f_0 and f_h for maximum power transfer between the antenna and diode. This reduces the *CL*, which is defined as the ratio of available power at f_0 to re-radiated power at f_h.

The impedance of a Schottky diode at a given frequency is mainly determined by its C_{j0}, dynamic, ohmic, or series resistance (R_s), parasitic or package elements, and drive level. Therefore, each diode performs best with a specifically designed antenna, and this multi-factor design process does not have a unique solution [95]. Since the harmonic radar transponder is a non-linear device, impedance matching solutions must consider the voltage driving the diode. Generally, the voltage corresponding to the maximum radar range is considered to ensure the transponder works well at the lowest incident power density.

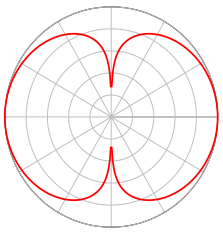
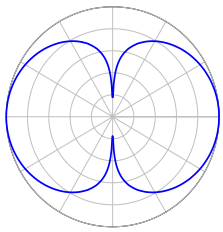
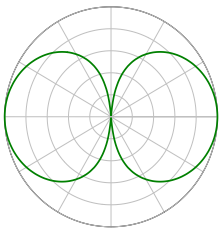
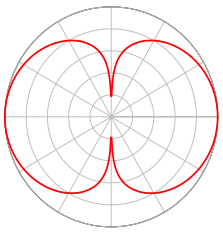
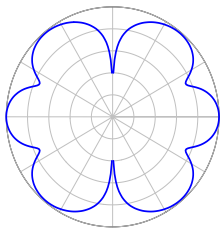
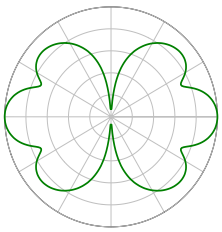
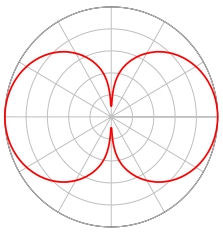
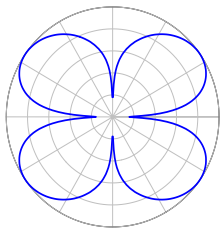
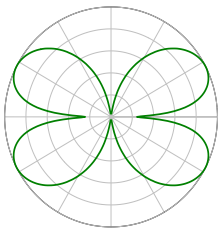
Another consideration in antenna design is its radiation pattern, which, for a dipole, is largely governed by its length. A longer dipole has a higher broadside gain but lower HPBW. Table 3.2 shows the radiation pattern on a logarithmic scale at f_0 and f_h, in terms of the dipole's electrical length at f_0. The harmonic radar range equation generally has a common term as the product of gain at the f_0 and f_h [34].

$$\sigma_h = \frac{\lambda_0^2}{4\pi} G_0 G_h \tag{3.1}$$

where λ_0 represents the wavelength at f_0, while G_0 and G_h denote the transponder gains corresponding to f_0 and f_h, respectively. Therefore, the sum of patterns at f_0 and f_h on the logarithmic scale can be taken to represent the total radiation pattern of the transponder. This is shown in the rightmost column of the table. If the antenna length exceeds approximately $0.55\lambda_0$, side lobes appear at the f_h, and the total pattern loses the traditional donut shape. These side lobes make the

transponder more detectable when the radar and transponder are at significantly different heights, *e.g.*, if the radar is mounted on a drone. When the electrical length approaches λ_0, a null is observed in the broadside direction of total pattern, which is generally undesired. The designed transponder in this work measures approximately $0.7\lambda_0$, *i.e.*, each arm is approximately $0.35\lambda_0$, which exhibits acceptable matching with the selected diode. With this length of dipole, side lobes are expected at f_h and in the total radiation patterns.

Table 3.2: General shape of the radiation pattern in terms of dipole length.

Dipole length at f_0	Pattern at f_0	Pattern at f_h	Total Pattern
$L < 0.55\lambda_0$			
$0.55\lambda_0 < L < 0.85\lambda_0$			
$0.85\lambda_0 < L < 1.1\lambda_0$			

The length of the loop providing a DC short across the diode in the design requires careful consideration. Simulation results indicate that increasing its length increases its inductance at both the f_0 and f_h. However, surpassing a certain threshold length result in a capacitive impedance, leading to a notable impact on *CL*. In this case, a length between 2 to 3 mm keeps the *CL* within an acceptable range. Similar findings

have been reported in [96].

3.3 Link Analysis for a Harmonic Radar System

The typical method for calculating received power versus transmitted power in a telecommunication link is the link analysis, which accounts for all the power gains and losses that the signal experiences. In contrast to conventional radars, a harmonic radar link encompasses two harmonically related frequencies in the forward and return paths, resulting in different gains and aperture areas for the radar antennas and transponder. Since the conventional RCS concept is not applicable in this scenario, the attenuation associated with the transponder can be estimated through simulation.

The available power at the transponder antenna terminals, P_{a}, is given by

$$P_{\mathrm{a}} = SA_{\mathrm{e}} \tag{3.2}$$

where S is the incident power density and A_e is the effective area of the transponder at f_0, which is in turn given by

$$A_{\mathrm{e}} = \frac{{\lambda_0}^2}{4\pi} G_0 \tag{3.3}$$

Where G_0 is the gain of the transponder antenna at f_0. P_{a} will only be delivered to the diode under perfect conjugate matching conditions. In practice, the power delivered to the diode, referred to as the *delivered power* and denoted by P_{d}, is given by.

$$P_{\mathrm{d}} = P_{\mathrm{a}} \frac{4R_{\mathrm{d}}R_{\mathrm{a}}}{(R_{\mathrm{a}} + R_{\mathrm{d}})^2 + (X_{\mathrm{a}} + X_{\mathrm{d}})^2} \tag{3.4}$$

where R_{d} and X_{d} are the resistance and reactance presented by the diode at f_0, respectively; and R_{a} and X_{a} are the resistance and reactance presented by the antenna

at f_0, respectively. Note that the antenna consists of the combination of the dipole and loop in this case.

Since the behavior of a harmonic radar transponder depends upon the incident power density, a specific transmitted power and range are considered for simulation purposes. A range of $R = 2.4\,\text{m}$ fits within ATC used for experimental validation while ensuring the transponder is in the far-field region of both the transmit (TX) and receive (RX) antennas. Consider the transponder at a range of $R = 2.4\,\text{m}$ from a harmonic radar system with a transmitted power of 22 dBm and transmit and receive antenna gains of 15.8 dBi at $f_0 = 10\,\text{GHz}$ and 24.5 dBi at $f_\text{h} = 20\,\text{GHz}$, respectively. This pair of frequencies was primarily selected based on practical considerations, such as the available TX and RX hardware, *e.g.*, antennas and harmonic rejection low pass filter (LPF). Working at higher frequencies is advantageous when building low-mass transponders with low *CL*, but achieving higher peak powers is challenging at higher frequencies. Since the overall concept will remain the same, the frequency pair can be adjusted based on the table of frequency allocations in the location of use.

In the link analysis, the transponder gains at f_0 and f_h are needed to determine the amount of power collected at f_0 and reradiated at f_h. Reflection losses due to impedance mismatches are considered separately, and the transponder is assumed to be polarization-aligned with both radar antennas, *i.e.*, polarization mismatch is neglected. This assumption is justifiable because, with the assumption of a tilt angle of θ_0 between two linear waves, polarization mismatch loss will be given by:

$$PL = 20\log(\cos\theta_0) \tag{3.5}$$

Assuming a 15° tilt in both transmission and reception, which is much higher than expected in a controlled experiment, the polarization mismatch loss will be 0.3 dB in each direction, as well as a maximum of 0.3 dB increase in conversion loss. The sum of these values is 0.9 dB, which is acceptable.

The gain pattern was simulated using Computer Simulation Technology (CST) Studio Suite and the result was similar to the middle row of Table 3.2. In the following calculations, the broadside gain of the transponder is considered, which is +2.5 dBi at f_0 and -0.45 dBi at f_h. The reason for a relatively low gain at f_h is the existence of side lobes in the radiation pattern due to the transponder length that is longer than $0.5\lambda_0$. This directs a part of the energy to these lobes.

The available power at the transponder antenna terminals, attenuated by an impedance mismatch between the dipole and diode, yields the transponder's received power. An equivalent circuit for the antenna is needed to derive this value, which could be balanced or unbalanced as shown in Figure 3.1. Considering the symmetry of dipole, for a very large value of ground impedance, Z_g, in the balanced circuit, ground currents can be neglected. Therefore, the single-ended antenna open circuit voltages, V_{oc1} and V_{oc2}, and impedances, Z_{a1} and Z_{a2}, are in series. Thus,

$$\begin{cases} V_{oc} = V_{oc1} + V_{oc2} \\ Z_a = Z_{a1} + Z_{a2} \end{cases} \tag{3.6}$$

and the circuits can be used interchangeably.

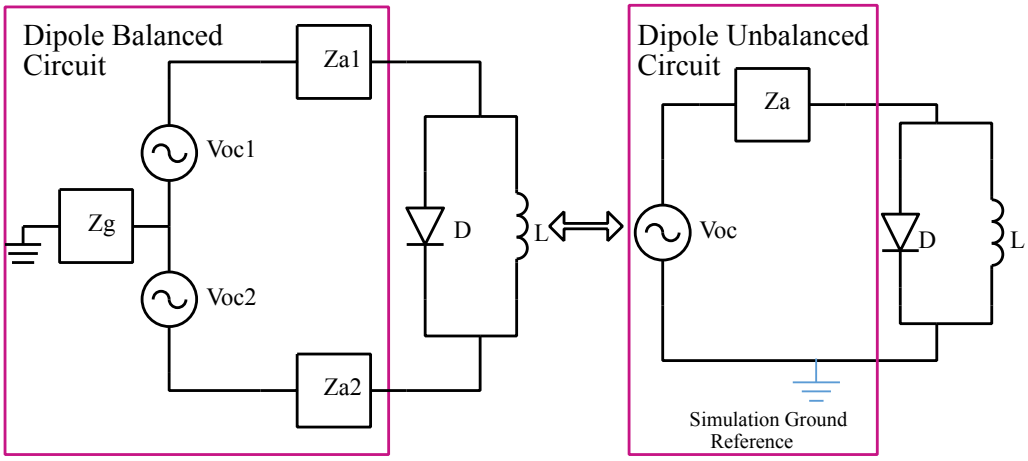


Figure 3.1: Transponder balanced and unbalanced equivalent circuits.

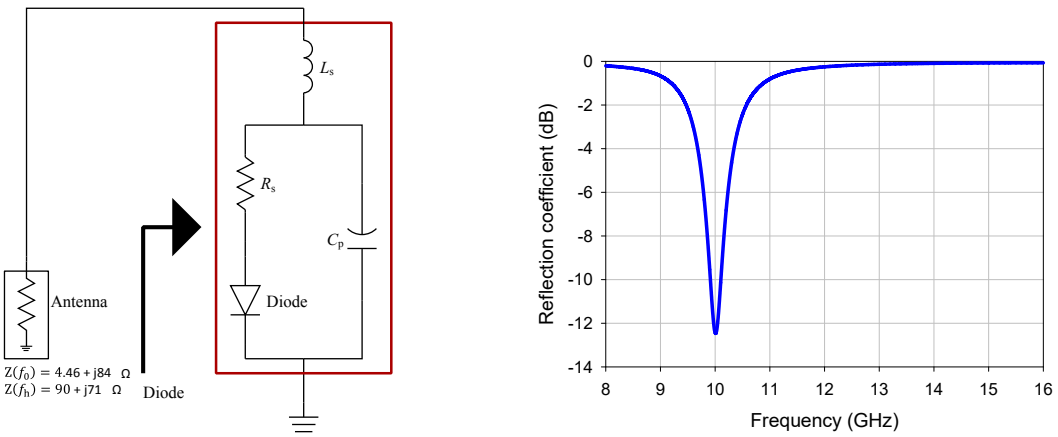
S-parameter analysis, based on the ADS schematic shown in Figure 3.2a, yields

the associated reflection coefficient. For this simulation, the SPICE model of the diode is employed, encompassing package elements, as summarized in Table 3.3. The model incorporates parasitic capacitance (C_p), L_s, and R_s to account for packaging effects. The schematic also features a frequency-dependent port representing the impedance of the dipole and loop at both f_0 and f_h.

Table 3.3: SPICE parameters of the MACOM MA4E2501L-1290 diode.

Parameter	Value
R_s	$10\,\Omega$
C_j0	$0.12\,\mathrm{pF}$
V_j	$0.08\,\mathrm{V}$
I_s	$26\,\mathrm{nA}$
L_s	$0.55\,\mathrm{nH}$
C_p	$0.02\,\mathrm{pF}$

Figure 3.2b shows the magnitude of the reflection coefficient, $|\Gamma|$, in dB between a silicon schottky diode (MA4E2501L-1290) and the discussed dipole antenna. Good matching value of -12.5 dB is observed at f_0. Considering the antenna impedance of $Z_\mathrm{a}(f_0) = 4.46 + j84\,\Omega$ and diode impedance of $Z_\mathrm{d}(f_0) = 7.25 - j84.28\,\Omega$, evaluation of (3) yields a ratio of 0.943 for P_r over P_a, which translates to a mismatch loss of 0.25 dB.



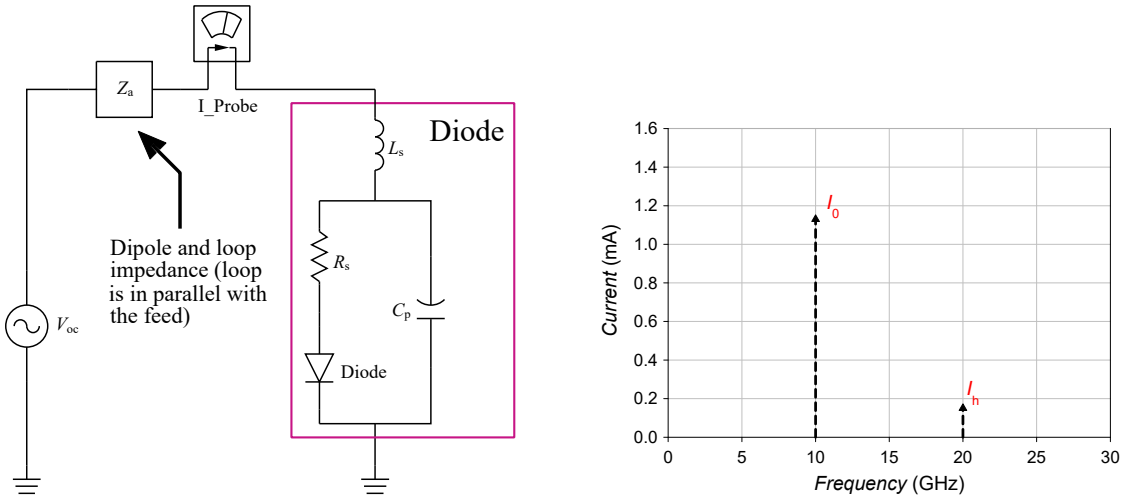
(a) (b)

Figure 3.2: Simulation of matching between dipole and diode: (a) schematic, (b) reflection coefficient plot.

The next step in the link analysis is finding the amplitude of current at the f_{h} using a harmonic balance simulation, as shown by the ADS schematic in Figure 3.3a. An unbalanced copy of the antenna impedance derived from full-wave analysis in CST Studio Suite is in series with the diode, and the circuit is driven by an open-circuit voltage (V_{oc}) which can be expressed as [34, 54]

$$V_{\mathrm{oc}} = \sqrt{8 R_{\mathrm{a}} P_{\mathrm{a}}}. \tag{3.7}$$

Taking into account the TX power, its antenna gain, the distance between the TX and the transponder, and the effective aperture of the transponder, the available power is calculated to be -19.7 dBm, which corresponds to $P_{\mathrm{a}} = 10.71, \mu\mathrm{W}$. Plugging this and $R_{\mathrm{a}} = 4.46\,\Omega$ into 3.7 yields $V_{\mathrm{oc}} = 19.55\,\mathrm{mV}$. The harmonic balance simulation results are depicted by Figure 3.3b as the magnitude of current at both frequencies.



(a) (b)

Figure 3.3: The harmonic balance simulation: (a) schematic, (b) magnitude of the first and second current harmonics.

The harmonic *CL* of the transponder can be expressed as

$$L_{\mathrm{h}} = 10 \log_{10} \frac{R_{\mathrm{rad},0} |I_0|^2}{R_{\mathrm{rad,h}} |I_{\mathrm{h}}|^2} \tag{3.8}$$

where I_0 and I_h are the amplitude of current at f_0 and f_h, respectively. In this case, $I_0 = 1.13\,\text{mA}$, $I_h = 0.15\,\text{mA}$, $R_{rad,0} = 4.46\,\Omega$, and $R_{rad,h} = 89.98\,\Omega$, which translates to a harmonic *CL* of 4.5 dB. This value is governed by the power density incident upon the transponder, operating frequency, impedance matching between dipole and diode, as well as electrical specifications of diode. Specifically, C_{j0} and C_p of the diode significantly impact the achievable *CL*—lower capacitances translate to lower *CL*. Selecting a diode with a low barrier junction is another necessity to ensure that a very low induced voltage can turn the diode on [96].

Finally, the received harmonic signal is changed by the gain of transponder antenna, path loss, and radar receive antenna effective aperture at f_h. Table 3.4 summarizes each step in the harmonic radar transceiver link. In the examined case, a transmitted power of +22 dBm at 10 GHz translates to a received power of -66.4 dBm at 20 GHz.

Table 3.4: Summary of steps in the harmonic radar transceiver link for a range of $R = 2.4\,\text{m}$.

Parameter	Value	Unit
TX power (f_0)	22	dBm
TX antenna gain (f_0)	15.8	dBi
Path loss (f_0)	60	dB
Transponder gain (f_0)	2.5	dBi
Mismatch loss (f_0)	0.25	dB
Harmonic *CL*	4.5	dB
Transponder gain (f_h)	-0.45	dBi
Path loss (f_h)	66	dB
RX antenna gain (f_h)	24.5	dBi
RX power (f_h)	-66.4	dBm

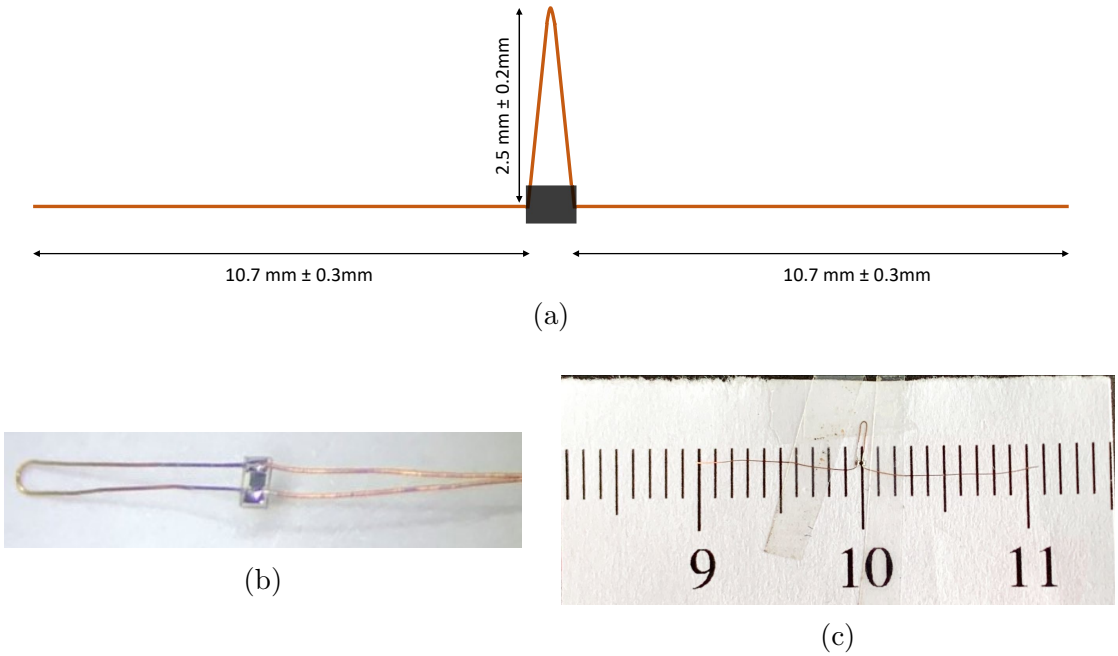
3.4 Experiment and Discussion

3.4.1 Specifications of the Transponder

Figure 3.4a shows the dimensions of the proposed transponder. The specified tolerances are indicated due to the transponder being affixed to a piece of paper with a printed ruler. Based on experience, manual cutting in this context could potentially result in a total error of up to 1 mm.The mass is reduced mainly by using thinner wire for the antenna. Although it is more prone to deformation, careful design can ensure transponder detectability is not sacrificed for mass reduction, as discussed in the next section.

Building this transponder does not require special tools—only a soldering iron with a very fine tip. A long wire is folded and soldered to the diode terminals at the desired locations, as shown in Figure 3.4b. Next, the wire is cut from each end to the desired length, which was achieved by adhering the transponder to a piece of paper with a printed ruler as depicted in Figure 3.4c. The diode used to make this transponder, the MACOM MA4E2501L-1290, has dimensions of $0.6 \times 0.3 \times 0.15\,\mathrm{mm}$.

The antenna is made with AWG#44 wire, which is readily available in steel and copper. Although steel is sturdier and more durable, the strength of copper is acceptable for this application and preferred for ease of soldering. Copper has an electrical conductivity of $\sigma = 5.8 \times 10^7$ S/m. This electrical conductivity is sensitive to changes in temperature, with a temperature coefficient of resistance of 0.393 % per degree Celsius. Furthermore, the density of copper is $\rho = 8.96\,\mathrm{g/cm^3}$. It is also influenced by variations in temperature, with a temperature coefficient of $\alpha = 3.93 \times 10^{-3}\,\mathrm{K^{-1}}$. Considering the length and density of copper, the dipole weighs approximately 460 µg. While the datasheet does not specify the diode's mass, it is estimated to be less than 70 µg based on its volume and the density of its dominant material, glass. Consequently, the transponder has a mass of nearly 530 µg which, to the best of our



(a)

(b)

(c)

Figure 3.4: Structure of transponder (a) dimensions, (b) loop and soldered diode, and (c) final transponder stuck on the scaled paper.

knowledge, is the lightest available harmonic radar transponder. A certain degree of tolerance exists in the specified mass, primarily originating from possible variations in arm lengths due to manual cutting and fluctuations in loop length. The antenna's mass is calculated by multiplying the copper density with the wire volume, taking into account both its length and cross-sectional area. Each of these values carries an associated tolerance, collectively contributing to an overall tolerance in the final mass calculation. The density of copper is denoted by ρ and is equal to 8.96 g/cm^3, with a tolerance of zero assumed for the purposes of this calculation. Referring to the datasheet from MWS Wire Industries, the diameter and its associated tolerance for the AWG#44 copper wire are given as $D = 0.0508 \pm 0.00254$ mm [97], while the wire length is 26.4 ± 1 mm, as discussed earlier. By applying error propagation, the impact of uncertainties in the variables is computed, revealing an error of $\pm 50\,\mu$g, which corresponds to a 10% variation.

The mass of the transponder is also determined using the ER-182A analytical

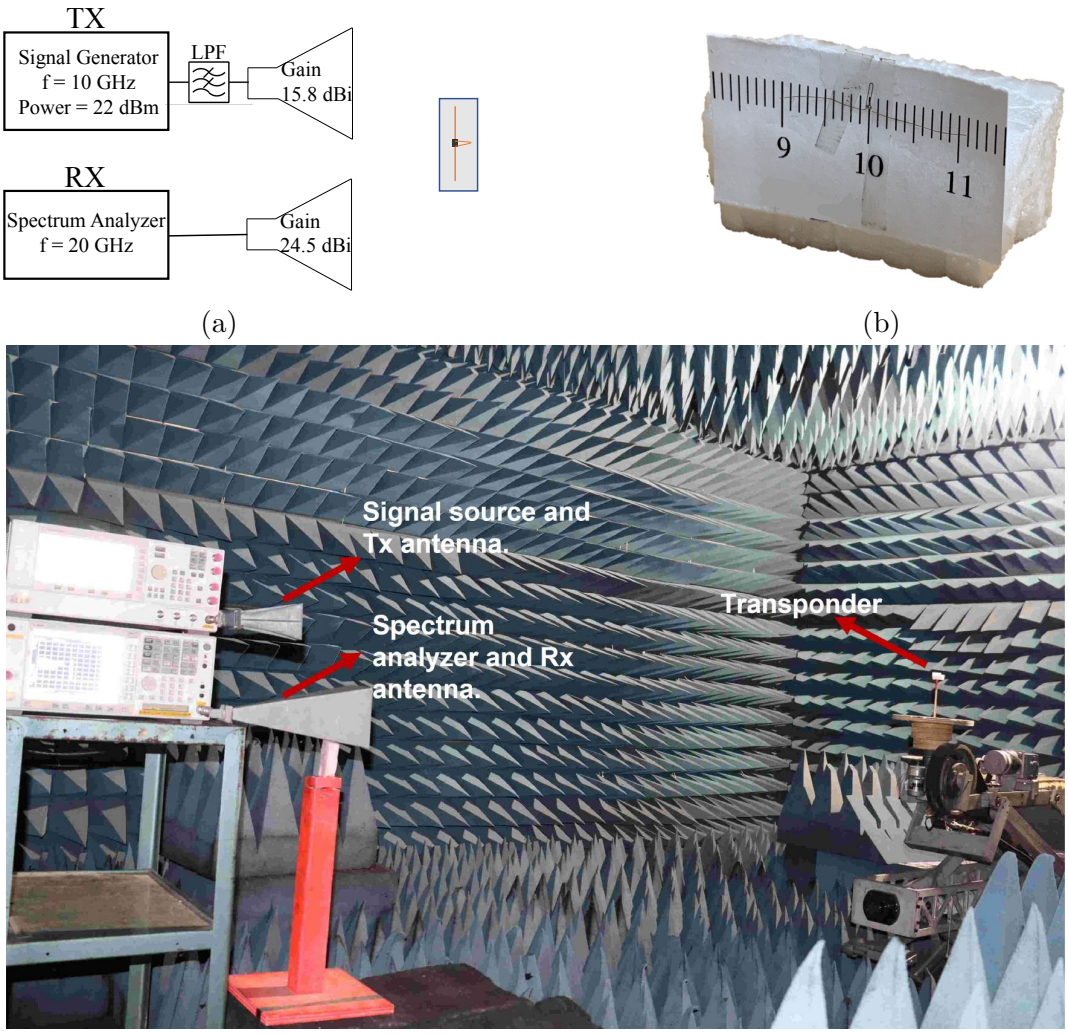
balance from A&D Company. This model has a maximum capacity of 180 g and a division of 100 µg, allowing for measurements with an error margin of ±50 µg. The measurements were conducted five times, resulting in values of 500 µg in four instances and 600 µg in one measurement. These results closely align with the calculated mass of 530 µg.

In practice, attaching a transponder to an insect should be carefully evaluated on a case-by-case basis. While glue may be a feasible option that adds minimal mass, it is important to consider potential toxic interactions between certain adhesives and specific insect species.

3.4.2 Measuring the Broadside Harmonic Amplitude

The test setup to measure the transponder's broadside harmonic amplitude included an Agilent E8257C signal generator configured to produce a 10 GHz signal and an Agilent E4440A spectrum analyzer to capture the harmonic signal at 20 GHz. As shown in Figure 3.5a, a LPF was used between the signal generator and transmitting antenna to suppress harmonics produced by the generator. The receiving antenna was directly connected to the spectrum analyzer without down-conversion or signal processing. To minimize power loss, cables were substituted with low-loss adapters for all connections. The power delivered to the transmit antenna port was measured to be +22 dBm and -90 dBm at f_0 and f_h, respectively. To maintain the desired orientation, the transponder was adhered to a piece of paper, which was in turn mounted on a piece of Styrofoam, as shown in Figure 3.5b. It is important to note that this mounting structure attenuates the received signal, especially if it is between radar and transponder. Figure 3.5c shows the measurement setup in ATC.

Initially, the transponder antenna had a length of more than $2\lambda_0$. The wire was gradually trimmed from each end while the amplitude of the received harmonic was measured to find the optimal length. Cutting continued until the length was less than



(a) (b)

(c)

Figure 3.5: Testing setup (a) diagram (b) a transponder mounted on styrofoam (c) measurement setup.

$0.5\lambda_0$. Transponders with unequal arm lengths, including a 2:1 ratio, were considered; however, a length of $0.7\lambda_0$ with equal arms provided the maximum harmonic power. With the transponder placed 2.4 m from the radar antenna apertures, the power at the receive antenna port was measured to be approximately -70 dBm, which agrees with the simulation result of approximately -66.4 dBm.

There are several sources of measurement error. Calibration by connecting the signal generator directly to the spectrum analyzer was not possible because the transmitted and received frequencies are different. As a result, the spectrum analyzer's

power measurements at each frequency were assumed to be accurate. There may also be small error margins on the measured antenna gains. The transponder may not have been perfectly positioned in the direction of maximum gain for both radar antennas and may not have been perfectly broadside to the radar. The adaptors were assumed to exhibit negligible insertion loss. Finally, the transponder was hand-made, resulting in somewhat limited control over its dimensions.

3.4.3 Measuring Radiation Pattern

Although individually plotting the transponder's radiation pattern at f_0 and f_h is useful in the design stage, the summation of these patterns is more relevant to the overall performance of the transponder. Figure 3.6 illustrates the setup for measuring this radiation pattern. The received signal at f_h is measured using an Agilent N5242A PNA-X vector network analyzer (VNA). Since the transmitted and received signals are not at the same frequency, the VNA source port could not be used as TX. Instead, an external signal generator was connected to the transmitting antenna, and the unused VNA port was match-terminated. To capture the radiation pattern, the receive antenna was connected to port 1 of VNA and S_{12} was measured while the transponder was rotated in the desired planes. Synchronization of the signal generator and VNA was achieved by connecting the signal generator's 10 MHz reference output to the VNA's external reference port. This allows the selection of a lower IF bandwidth within the VNA, which translates to a lower noise floor. Thus, the received harmonic signal was above the noise floor and easily detectable in most orientations. The associated increase in sweep time can be accommodated by reducing the rotation speed or decreasing the angular resolution.

Figure 3.7a and Figure 3.7b show the normalized elevation- and azimuth-plane radiation patterns of the transponder as solid curves. The summation of fundamental and harmonic patterns obtained in simulation are added to these plots as dashed

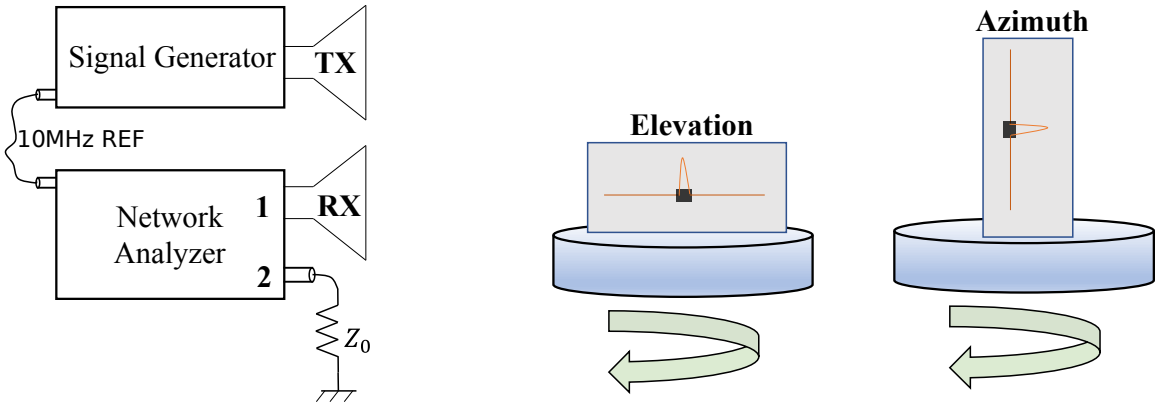
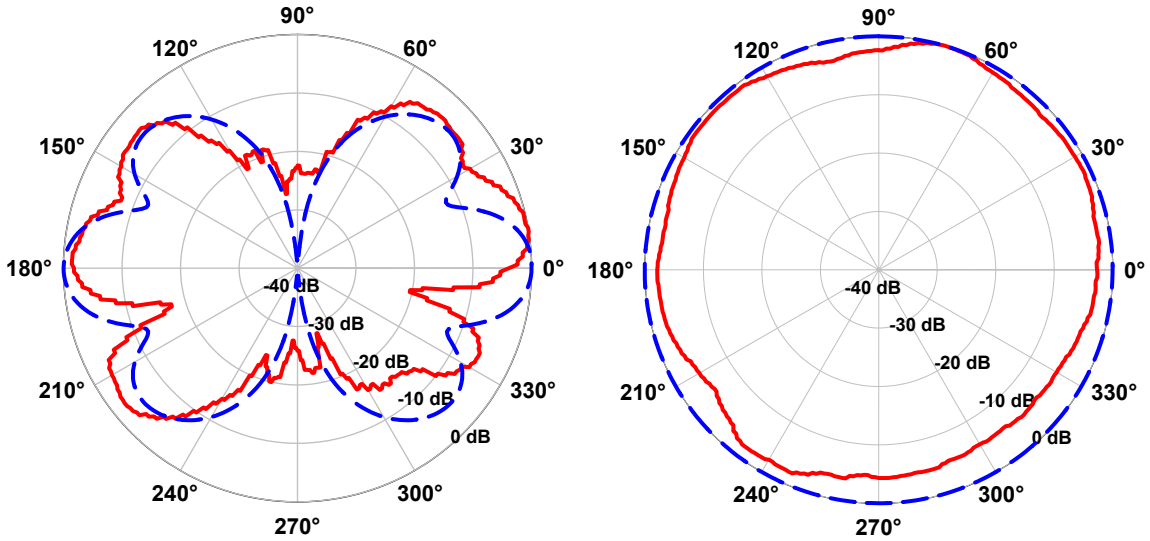


Figure 3.6: Diagram of a typical harmonic radar link.

curves. The measured radiation pattern generally fits the summation of simulated patterns at f_0 and f_h. There are several reasons for the discrepancies. First, deep nulls are buried under the noise floor of the receiving instrument. In this measurement, the main lobe is roughly 25 dB higher than the Minimum Detectable Signal (MDS). The mounting structure of the transponder affects both transmitted and radiated signals, especially when it is between the transponder and antennas. This effect is more considerable in the azimuth radiation pattern and caused up to 5 dB of loss in some directions. Although it would not be considered a measurement error, the insect's body would have a similar impact on the results. Finally, the transponder might be slightly misaligned or deformed compared to the simulated structure.

Because of the nonlinear behavior of the Schottky diode, characteristics such as its impedance and the corresponding harmonic magnitude are functions of the drive level. Therefore, the radiation pattern is expected to change slightly by changing the transmitted power, range, and relative orientation of the transponder. However, the patterns have a similar shape regardless of incident power density, particularly the existence and locations of the main and side lobes. This was verified via radiation pattern measurements for transmitted powers of +22, +12, and +7 dBm as shown in Figure 3.8. To reduce the noise floor at the power levels of +12 and +7 dBm, the IF bandwidth was set to 3 Hz, and the received harmonic was sampled at two-



(a) (b)

Figure 3.7: Normalized radiation pattern of transponder in two planes (a) elevation (b) azimuth.

degree intervals. A lower TX power was also attempted, but the main lobes were not noticeably above the noise level. These plots show a similar total radiation pattern over a power level range of 15 dB.

3.4.4 Transponder Axial Ratio

Since the dipole antenna used in this transponder is linearly polarized, a polarization mismatch between the transponder and radar will affect the power at both f_0 and f_h. Cross-polarization, therefore, results in an extremely low received harmonic signal. During measurements, a cross-polarized transponder was not detectable. Figure 3.9 shows the axial ratio at frequencies of f_0 and f_h at the elevation plane. It shows that cross-polarization leads to signal losses of more than 40 dB in the main lobe at both frequencies—more than 80 dB in total. Circularly polarized radar antennas could be considered to maintain an uninterrupted received signal at the cost of maximum range and transponder mass.

The transponder is made with thin copper wire and is easily bent. While such

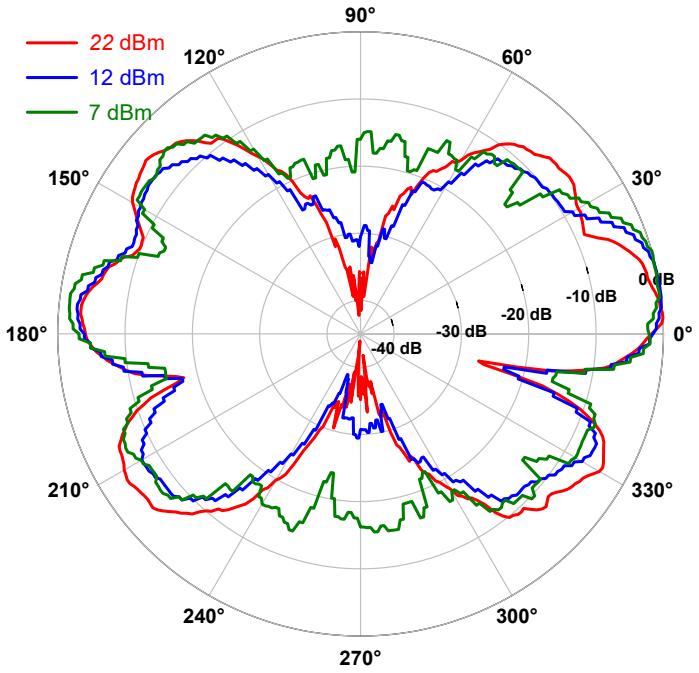


Figure 3.8: Total radiation pattern measured at three different transmitted power levels.

bends in one or both dipole arms would not have a significant effect on the impedance match with the diode, the transponder radiation pattern would be affected [6]. However, a deformed transponder would also exhibit a smaller axial ratio, potentially improving performance under polarization mismatches.

3.4.5 Estimated Maximum Detection Range

It is important to note that the received signal was measured for a low power TX and short range. In practical harmonic radar systems, much higher transmit power is used to extend the detection range. Of course, the maximum detection range would be governed by both radar specifications and the performance of the transponder. There is a great deal of variation in the composition of harmonic radar systems, *e.g.*, a portable system with lower gain antennas and limited transmit power versus a stationary system with large antenna and much more power. On the RX side, MDS has always been a problem for harmonic radar systems as they are limited by self-

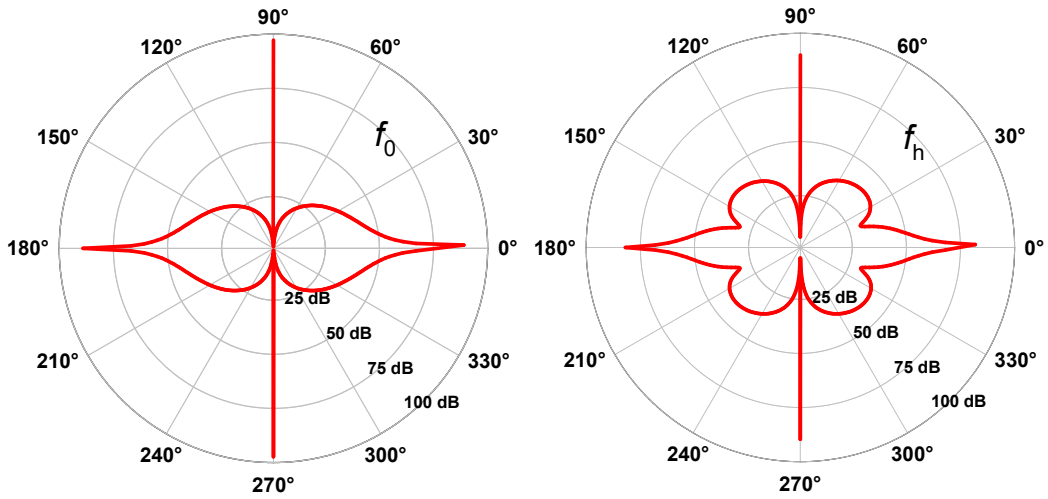


Figure 3.9: Simulation result for the axial ratio at f_0 and f_h at the elevation plane.

interference. A received harmonic signal as low as -100 dBm might be detectable if the dwell time on target is unlimited, but in practical cases it is much less sensitive. This encourages the application of advanced modulation and demodulation schemes to minimize the impact of self-interference.

To provide a better insight of the transponder performance under the different incident power densities or, equivalently, different radar ranges, the measured and simulated received power versus the transmitted power is plotted by sweeping the TX power as shown in Figure 3.10. A plot of harmonic *CL* is also shown, represented by a blue curve and referred to the right y-axis. The dynamic range of these measurements was limited by the maximum available power of our signal generator, +22 dBm, and the spectrum analyzer noise floor, -115 dBm. Results were obtained by reducing the signal generator power in 1-dB steps until the received power was no longer distinguishable from noise. Simulations were also performed for transmitted powers in the range of -15 to +40 dBm. The measurement and simulation plots are in an acceptable agreement with a maximum error of 6 dB, which was justified earlier in 5.2. The slope of the measurement plot is approximately 2 and the simulation plot has the slope of approximately 2 over the measurement range, reducing to approximately 1 for higher transmitted powers. The slope at lower transmitted power agrees with

the findings in [98].

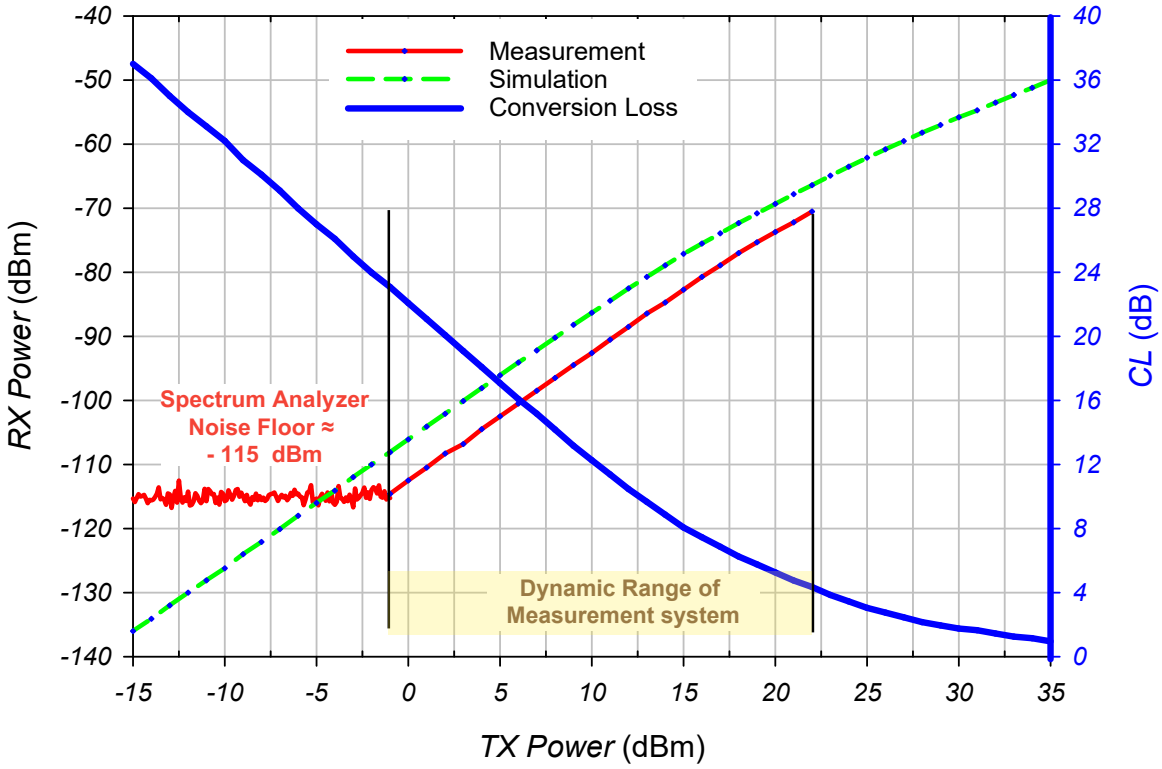


Figure 3.10: Measured and simulated received power versus the transmitted power for a constant range of $R = 2.4\,\text{m}$. Symbols on the plots are measured and simulated points. CL is also plotted in blue.

The link analysis presented above can be applied to a practical radar system, such as the one described in [18], to estimate a practical detection range. This radar consists of a 25 kW TX and TX and RX antenna gains of 28.5 and 27.4 dBi, respectively. The corresponding received power with the transponder presented in this Chapter is in a range of -70 to -90 dBm at a range of 150 to 450 m, which is enough for detection with an acceptable false alarm probability based on the noise floor and SNR of RX.

3.5 Conclusion

A harmonic radar transponder was constructed with copper wire of AWG#44 and a Schottky diode with a footprint of 0201, achieving a total mass of approximately

530 µg. As far as the available information indicates, this harmonic radar transponder stands out as the lightest option currently known. Construction is relatively easy as it requires soldering a diode to a wire and then cutting the wire to the proper length. At this specified length, optimal power transfer occurs due to the effective impedance matching between the dipole and diode, resulting in the maximization of received harmonic power. The transponder performance in terms of harmonic conversion efficiency has not been sacrificed by mass or structure. According to the simulation result, an available power of approximately -20 dBm led to a *CL* of 4.5 dB. Measurements performed in an ATC under similar conditions confirmed these results. The simulation predicted that transmitting a power of +22 dBm at a range of 2.4 m resulted in a received power of -66.4 dBm at the harmonic, which agreed well with the measured result of -70 dBm. The transponder's radiation pattern was measured with a new method: instead of measuring the transponder's radiation pattern at the first and second harmonics using the intermodulation technique, the total radiation pattern was measured by employing an external signal generator that was synchronized with VNA acting as RX. The measured pattern was in good agreement with the simulation. This transponder will enable the tracking of insects that are far too small to support the state-of-the-art radio transmitters. For future advancements in this area, it will be important to further investigate the mechanical robustness of the transponder.

Chapter 4

Diode Analysis and Performance Evaluation in Transponders

4.1 Introduction

This chapter provides a detailed examination of the diode, which serves as the nonlinear element in the transponder. The behavior of the transponder is first investigated under low- and high-power density conditions in Section 4.2. The transponder's response under very high power levels is then explored, including an analysis of the relationship between the diode's harmonic content and the RF power in Section 4.3.

In addition to selecting a diode with a small physical footprint, a thorough evaluation of the SPICE parameters is crucial for enhancing the detection range of the transponder. Section 4.4 focuses on the individual impact of various parameters, analyzing their significance. Subsequently, in Section 4.5, the importance of these parameters is quantified using DOE method. This approach enables a comprehensive assessment of the relative significance of each parameter, facilitating informed design decisions.

4.2 Two Regions of Transponder Operation

In Section 3.4.5, the relationship between the received power of the transponder and the transmitted power is explored. The corresponding plot in Figure 3.10 presents both the measured and simulated received power as a function of the transmitted power. This plot reveals two distinct regions that correspond to low and high received powers, providing valuable insights into the transponder's behavior.

A more detailed analysis of this plot is essential to uncover its significant features. Specifically, it is important to examine the impact of the diode's SPICE parameters on the plot. By studying the relationship between the received and transmitted powers, optimal design and operation points for a harmonic radar system can be determined. This plot serves as a valuable tool for evaluating and optimizing the performance of the transponder, aiding in the development of efficient and reliable radar systems.

Figure 4.1 presents a logarithmic plot of the RX versus TX power, providing valuable insights into the behavior of the system. Several features can be observed in this plot that require further explanation. The plot can be divided into two distinct regions, each characterized by a log-linear relationship: a low-power region, shaded in green, and a high-power region, shaded in red. In the low-power region, the slope is steeper, with a value of approximately 2, compared to the slope in the high-power region. As power increases in the high-power region, the slope gradually decreases until it eventually reaches values less than 1. A higher slope corresponds to a higher sensitivity of the system to the transponder drive level, while the lower slope in the high-power region indicates a reduced sensitivity. For slope comparison, each region's plot is extended with a dashed line onto the other region. As depicted in the Figure, the intersection of lines in the low and high-power regions forms a knee point. To illustrate the gradual slope transition, a red line has been included. For a given radar and range, the TX power corresponding to the knee point is determined by the diode's SPICE parameters. It is important to note that the sudden slope change depicted in

this illustration is for explanatory purposes. In practice, as the power level increases, the slope gradually decreases from 2 and approaches 1. This phenomenon is discussed further in Section 4.2.2.

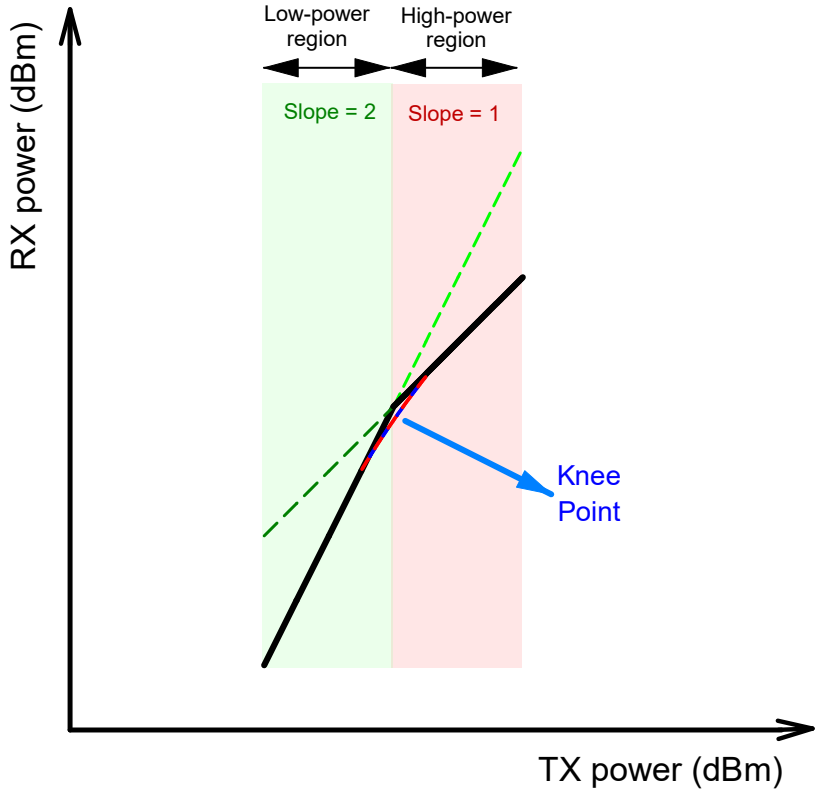


Figure 4.1: Received power as a function of transmitted power, with a dashed green line extending across regions.

The designer of the harmonic radar and transponder faces the task of determining the appropriate TX power based on the radar specifications and the desired detection range. Increasing TX power by using a high-power amplifier can extend the radar range, but it comes with drawbacks such as increased cost, size, and weight of the system. Additionally, high-power amplifiers require heat sinks and additional protective circuits, making them impractical for portable applications, such as small radar introduced in [21]. Consequently, the designer aims to identify an optimum TX power.

To minimize *CL*, it is generally recommended to set TX power in a way that en-

sures the transponder is excited at or above the knee point at the maximum expected range. This selection prevents the system from entering the low-power region.

4.2.1 Transponder Conversion Loss versus Drive Level

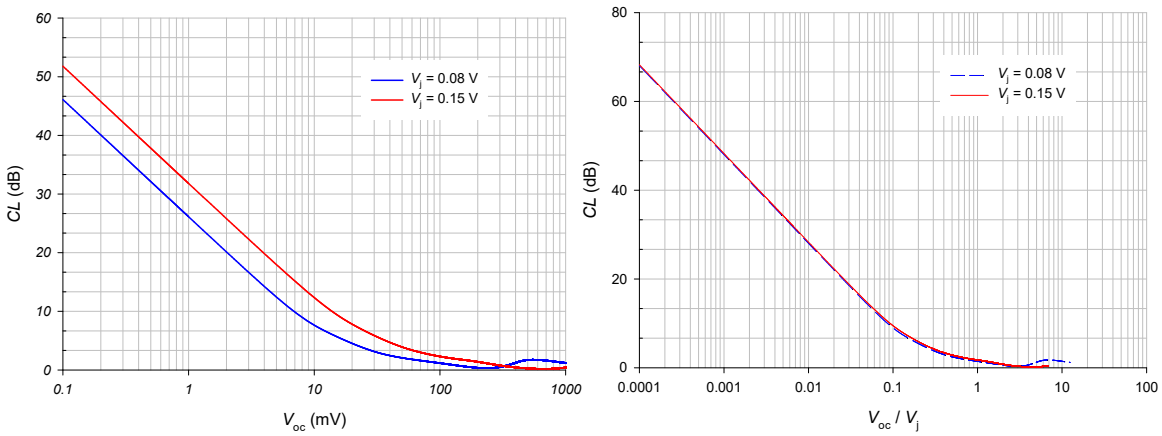
In Chapter 3, in the analysis of the transponder's generated harmonic power, the received power is plotted against the transmitted power at a specific range. An alternative approach is to plot the *CL* versus V_{oc}. The advantage of this approach is its simulation simplicity, as the harmonic balance simulation for this case employs an AC voltage source as the input signal. Consequently, it becomes possible to sweep the voltage and observe the corresponding *CL*. However, it is essential to establish a reasonable range for V_{oc} by considering the relationship between transmitted power and V_{oc}, as indicated in Equation 3.7.

4.2.2 Diode SPICE Parameters and Knee Point

A Schottky diode turns on when the voltage across its metal-semiconductor junction exceeds a threshold, which is determined based on the diode SPICE parameters. In the process of transponder design, opting for a diode categorized as *low-barrier* or *extremely low-barrier* will effectively reduce the minimum voltage necessary to trigger the diode. This adjustment facilitates the transponder's operation at a lower incident power density. V_{j} serves as the quantitative parameter that characterizes the barrier voltage in the diode.

The value of V_{oc} at the knee point is contingent on the value of V_{j}, as demonstrated in this section. Figure 4.2a shows the simulated *CL* versus V_{oc} for the transponder described in Chapter 3. The plot highlights the power characteristics of a transponder utilizing two identical diodes but with different V_{j} values: 0.08 V (represented by the blue line) and 0.15 V (represented by the red line). Regarding the blue plot, a slight increase in *CL* is observed when V_{oc} exceeds 300 mV. This phenomenon can

be attributed to the voltage-dependent nature of the diode junction capacitance (C_j) across the diode terminals. Furthermore, another study has demonstrated that as RF power is elevated to higher levels, the *CL* exhibits a corresponding increase as well [99]. Figure 4.2b shows the plotted *CL* against V_{oc} normalized by the corresponding V_j values. The normalization leads to similar plots for two different V_j values.



(a) (b)

Figure 4.2: *CL* plotted for two different V_j values in relation to a) V_{oc} and b) V_{oc} normalized by the corresponding V_j values.

Upon examining these graphs, it becomes apparent that a diode with a higher V_j, represented by the red line in this case, incurs a greater *CL* for the same drive level. This observation is logical since a real diode gradually turns on by increasing the voltage across its terminals. The red and blue lines converge as the transmitted power increases or, equivalently, the diode's driving voltage increases, as indicated by Figure 4.2a.

In Section 4.2, the knee point is defined as the intersection of the section with the slope of 1 and 2 in the receive versus transmit power plot. Here, by substituting V_{oc} for the transmitted power on the x-axis, the slopes may alter, yet they can still be accurately determined to ascertain the knee point. By taking the derivative of the *CL* with respect to $20\log(V_{oc}/V_j)$, as illustrated in Figure 4.3, it becomes feasible to pinpoint the knee point. Figure 4.3 displays a pink line indicating a derivative value

of 0.5, along with the corresponding x-axis value of approximately -14 dB. The slope of -0.5 is identified as the knee point (P_{k}), positioned halfway between the slope of -1 to 0. The value of -14 dB corresponds to approximately

$$P_{\mathrm{k}} = 0.2\, V_{\mathrm{j}} \tag{4.1}$$

which equates to 0.016 V and 0.03 V for $V_{\mathrm{j}} = 0.08$ and 0.15, respectively. This shows that the knee point is linearly related to the V_{j}. Since selecting a low-barrier diode is one of the preliminary requirements for transponder design, the simulation was not repeated for the higher values of V_{j}. However, the results could be generalized: a higher V_{j} means a higher knee point and *CL* for a given transmitted power.

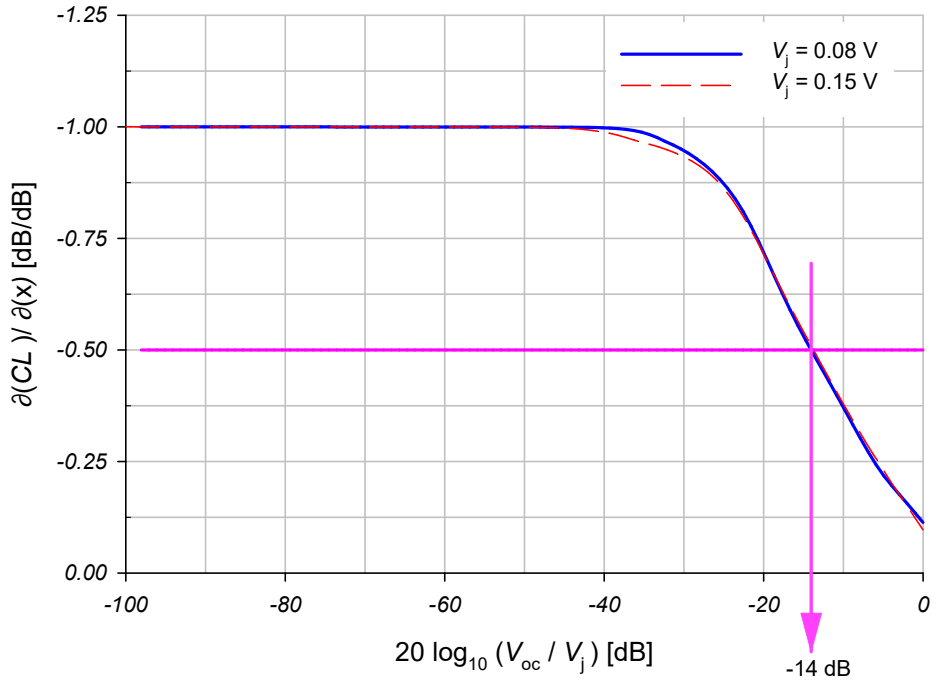


Figure 4.3: Absolute value of the derivative of the CL over the V_{oc} for two values of V_{j}.

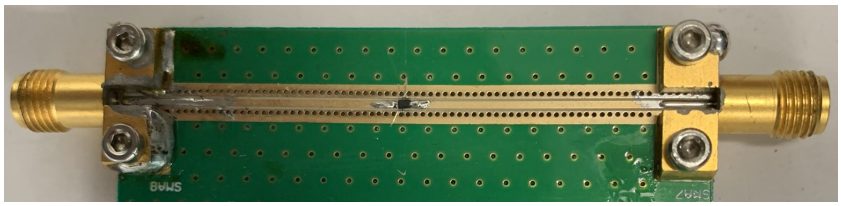
In the above discussion, the *CL* has been plotted by sweeping V_{oc} across a range of 55 dB of transmitted power. This range effectively covers both high-power and low-power regions. Utilizing the pair of V_{oc} and *CL* offers advantages as it eliminates the need to report radar specifications and ranges separately. The derived values can be

translated into various ranges and transmitted power levels as required. By replacing *CL* with σ_{h} and V_{oc} with incident power density, a more suitable representation can be obtained to assess the performance of a transponder. This approach eliminates the necessity of providing radar specifications and range when reporting these values. However, when it comes to assessing the performance of a diode in the transponder, the combination of V_{oc} and *CL* provides a more intuitive understanding.

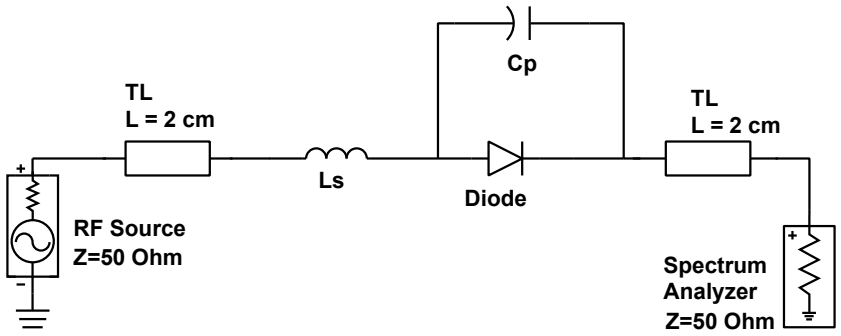
4.3 Transponder Performance in the High Power Region

The relationship between TX and RX power at low and high-power regions is examined in 3.4.5, with further details provided in Section 4.2.2. In the low-power region, it has been concluded that the TX versus RX power plot exhibits a slope of two. This slope has been confirmed by both simulations and measurements over a wide range of test powers. However, measuring in the high-power region was not feasible due to equipment constraints, *i.e.* power limitations. To assess the performance of a transponder under high incident power density, a test was conducted on the SMS7630-079LF, a Surface Mount Device (SMD) Skyworks silicon Schottky diode with an 0402 footprint. The diode was mounted to a printed circuit board (PCB) with microstrip transmission lines, as depicted in Figure 4.4a, utilizing a 50 Ω impedance configuration. Additionally, a simulation was performed using the ADS harmonic balance simulator based on the schematic shown in Figure 4.4b. For enhanced accuracy in modeling, the simulation incorporates RF microstrip traces at both the input and output. The diode's SPICE parameters, used in the simulation, are summarized in Table 4.1. In this test, a 10 GHz signal was applied to the anode-side terminal, and the magnitude of the generated 20 GHz harmonic was measured at the output terminal. An LPF was placed at the output of the RF source to suppress

unwanted harmonics. The filter exhibited less than 1 dB of attenuation at 10 GHz, while delivering over 40 dB of attenuation at 20 GHz. Otherwise, harmonics produced within the signal generator might be confused with those of the diode. Referring to the datasheet, the diode's absolute maximum breakdown voltage (V_b) is specified as $V_b = 2$ V. As a result, in order to prevent surpassing this limit, the maximum RF power input limited at approximately 10 dBm. Figure 4.5 shows the simulated and measured output harmonic versus the input signal at frequencies of 10 GHz and 20 GHz, respectively. The simulation range is -50 to +10 dBm, but measurements were performed for input powers in the range of -40 to +10 dBm, limited by the noise floor of the spectrum analyzer.



(a)



(b)

Figure 4.4: A SMS7630 schottky diode mounted on a 50 Ω microstrip transmission line a) testing board b) simulation setup.

In Figure 4.5, there is a good agreement between the measured and simulated plots for input power belows -10 dBm. The expected low power slope of two is also confirmed by this test in both simulated and measured plots. As input power

Table 4.1: SPICE parameters of the Skyworks Schottky diode, SMS7630-079LF.

Parameter	Value	Parameter	Value
R_s	20 Ω	I_s	5 μA
C_{j0}	0.14 pF	N	1.05
V_j	0.34 V	L_s	0.7 nH
M	0.4	C_p	0.15 pF
V_b	2	TT	10^{-11} sec

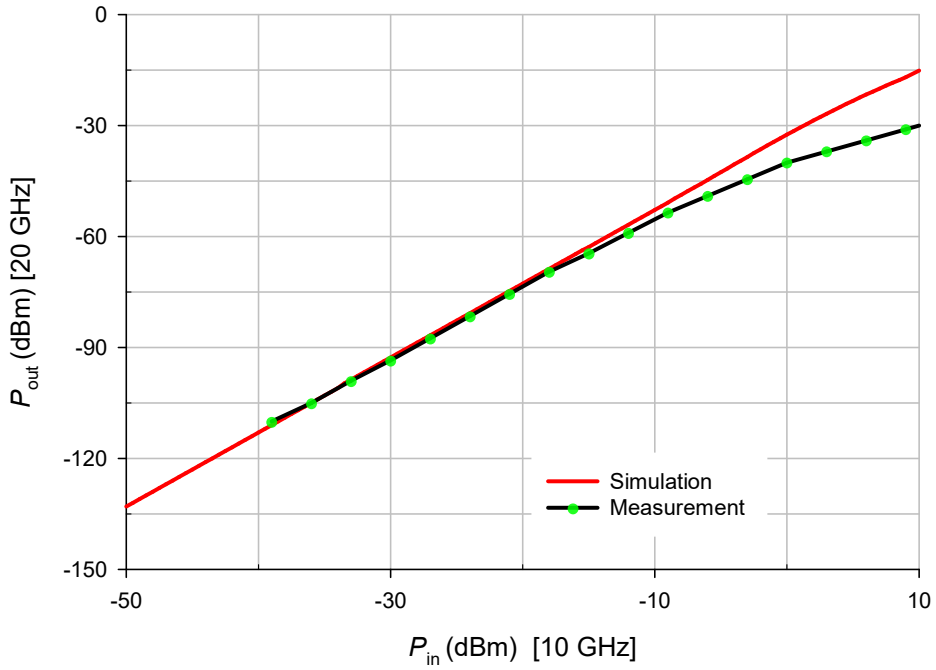


Figure 4.5: Amplitude of the harmonic at 20 GHz versus the RF power at 10 GHz for the circuit in Figure 4.4a.

increases, the simulation error is getting higher. It could be because the provided SPICE model is not sufficient for the large signal analysis. Reducing the value of the R_s in the SPICE parameters makes the simulated plot closer to the measurement plot at the large signal. Another possible reason for this discrepancy could be the high test frequency. The datasheet states that the model is valid up to 10 GHz, which is f_0 used in this test, and f_h is 20 GHz.

To have a better understanding of the transition between the low- and high-power regions, the slope of the measured and simulated plots of Figure 4.5 is provided in Figure 4.6. In the low-power region, both the simulated and measured have a slope

of two in both plots. Whereas in the simulated plot the slope starts dropping at an input power of -2 dBm, the measured plot start dropping at approximate power of -18 dBm. As input power gets higher, the slope of both simulated and measured plots reduces.

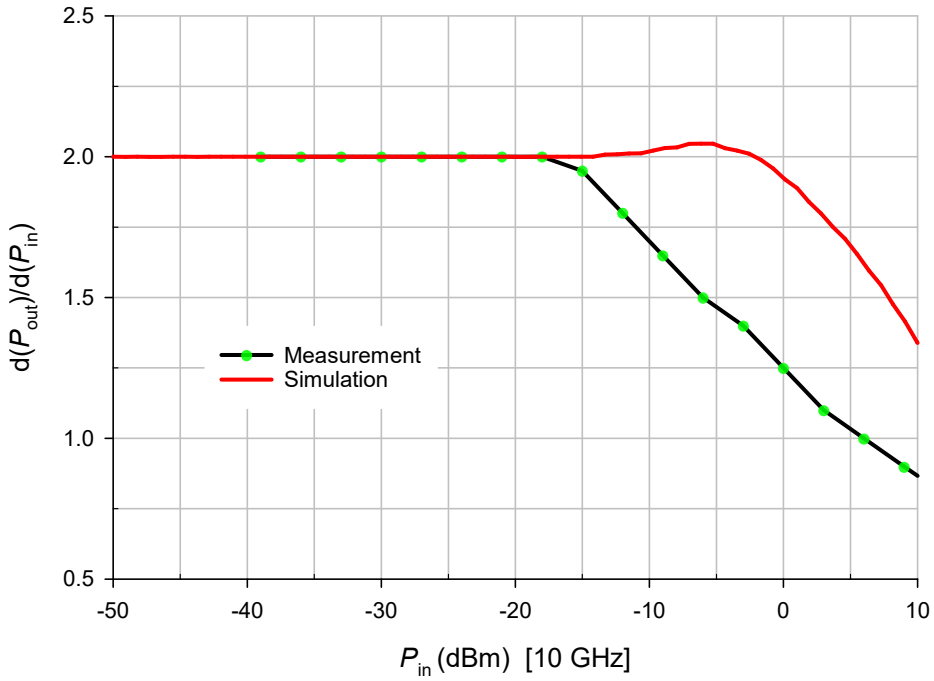


Figure 4.6: Simulated and measured derivative of diode harmonic power with respect to input RF power.

For the case of SMS7630-079LF Schottky diode, the simulated and measured *CL* versus the input power at the frequency of 10 GHz is plotted in Figure 4.7. As previously mentioned in this section, the RF power is limited to 10 dBm to prevent exceeding the designated $V_{\mathbf{b}}$ for the diode.

In practical scenarios, it is possible for a transponder to be subjected to a high power density. This can occur unintentionally when the distance between the radar and transponder becomes shorter than anticipated. If the power density received by a transponder is very high, it may lead to voltage and current levels that surpass the diode's absolute maximum rating as specified in the datasheet. This situation can potentially cause irreversible damage to the diode junction. As a consequence, the

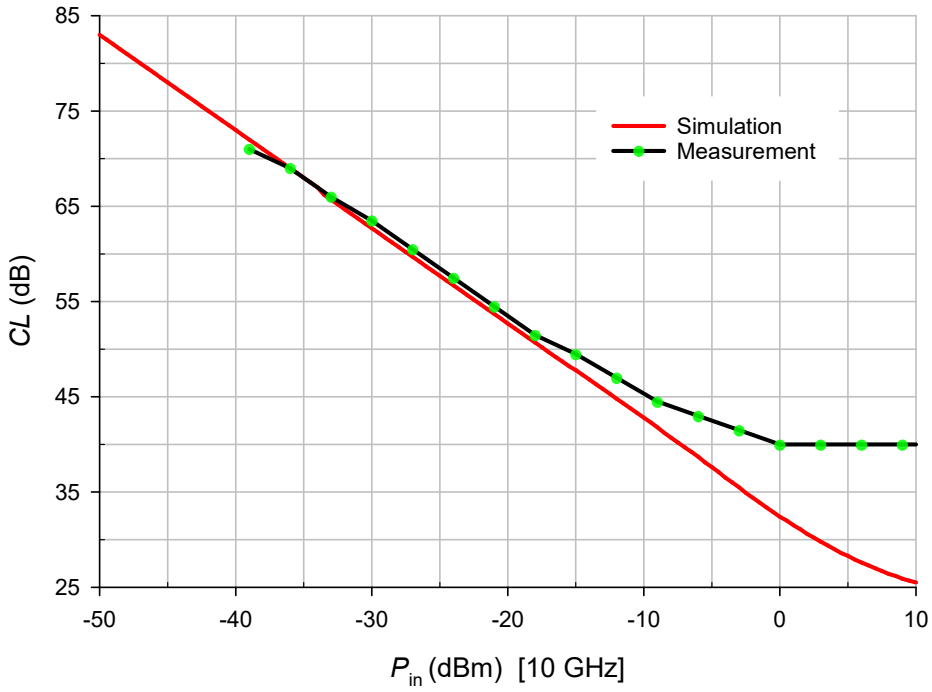


Figure 4.7: Simulated and measured CL against input power.

transponder will no longer generate the intended f_{h}, or the amplitude of the harmonic will be significantly diminished. To prevent this issue, the designer must ensure that, at the far-field boundary distance from the radar, V_{oc} and the diode short circuit current are significantly lower than their maximum ratings.

4.4 Schottky Diode Selection Criteria

In general, it appears that a diode that closely resembles an ideal diode exhibits better performance, characterized by lower V_{j}, R_{s}, and C_{j0}. Plotting the transponder CL against V_{oc} with different diode SPICE parameter values offers valuable insights into the impact of each parameter on transponder CL. To achieve this, a harmonic balance simulation, as described in Section 3.3, is performed. In this simulation, V_{oc} is swept over a range of 0.001 to 120 mV. The lower value of this range is determined based on the transmitted power of -60 dBm for the measurement system and transponder discussed in Chapter 3. However, the simulation does not extend up to

the upper value of 1500 mV in that range due to the limitations and inaccuracies of the simulation at very high values of V_{oc}.

Figures 4.8a to 4.8f depict the *CL* plotted against V_{oc}. Each figure includes two plots representing different values of a key SPICE parameter for the MA4E2502L Schottky diode manufactured by MACOM. The importance of these parameters is based on their potential impact on the *CL* when adjusted. However, the simulation results show that in the usual condition for a harmonic radar transponder, parameters such as the ideality factor, breakdown voltage, and temperature coefficient have minimal or negligible effect on the *CL*. Therefore, for the specific application of a harmonic radar transponder, these parameters are typically not significant factors influencing the *CL*.

Figures 4.8a and 4.8f highlight the significance of C_{j0} and C_p in relation to *CL*. Sweeping this value demonstrates that the *CL* reaches its minimum at lower drive levels for lower C_{j0} values. As the C_{j0} increases, the *CL* experiences a sharp increase. Therefore, it is generally advisable to use diodes with lower C_{j0} to minimize *CL*. Similar behavior is observed for L_s and C_p, where maintaining low values for these parameters is recommended to minimize *CL*.

As demonstrated in Figure 4.8b, it is evident that an increase in the V_j leads to a corresponding increase in the *CL*. This effect is particularly pronounced in the lower power range. Thus, it is highly recommended to choose a diode with a low V_j in order to minimize the *CL*. By opting for a diode with a lower V_j, the overall performance of the system can be improved, especially in low-power scenarios.

Finally, the parameters of R_s and I_s have a smaller impact on the *CL*. Figure 4.8c illustrates that I_s would need to be extremely large in order to adversely impact the *CL*. On the other hand, sweeping the R_s within its typical range reveals that lower values result in better performance with lower *CL*. Hence, it is advisable to choose a diode with lower R_s to optimize the *CL* and enhance overall performance.

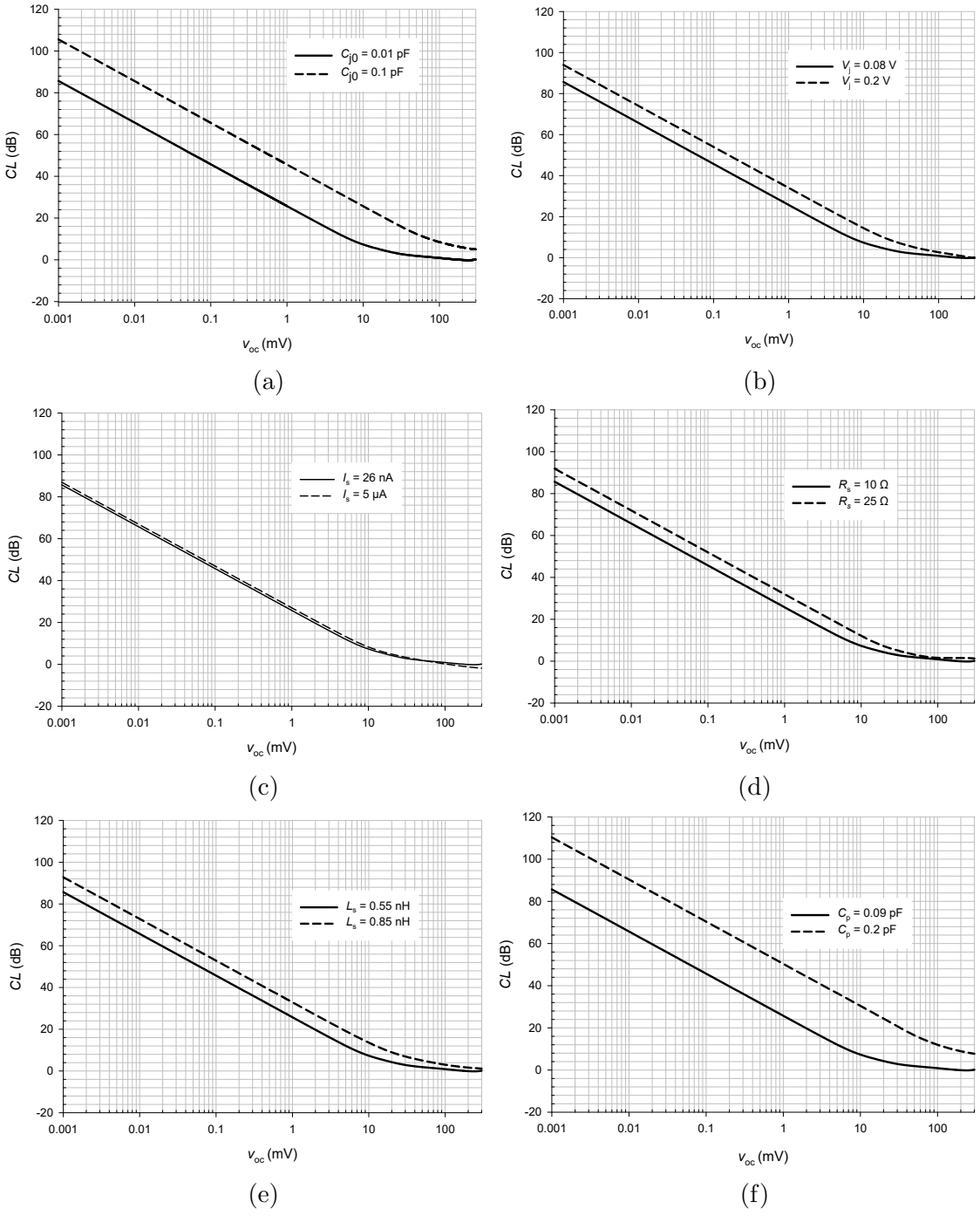


Figure 4.8: Transponder CL against V_{oc} for two values of a) C_{j0} b) V_{j} c) I_{s} d) R_{s} e) L_{s} f) C_{p}.

4.5 Design of Experiment

The existing plots in 4.4 may not provide sufficient information to accurately compare the importance of different SPICE parameters in determining the transponder *CL*. Thus far, only one parameter has been altered at a time, but now we will introduce variations in all of them simultaneously. For this purpose, one solution is to employ statistical methods such as DOE technique. This technique enables the allocation of numerical weights to each parameter, facilitating a more comprehensive assessment of their relative importance. By systematically varying the values of the SPICE parameters and analyzing their impact on the *CL*, DOE can provide valuable insights into the significance of each parameter and guide the optimization process.

4.5.1 A Suitable Range for each SPICE Parameter

The initial stage of conducting DOE involves generating a database through simulation to calculate the *CL*. This is accomplished by varying the values of diode SPICE parameters within a suitable range. The careful selection of this range is crucial to prevent inaccurate or misleading outcomes. For instance, if the upper limit for V_j is set at 0.7 V, it will mistakenly appear as a more influential parameter than it actually is because for the high value of V_j the *CL* tends to increase significantly. However, in practice, a designer would choose a low-barrier Schottky diode that does not have a V_j exceeding 0.4 V.

The suitable ranges of SPICE parameters are determined by considering the characteristics of commonly used diodes in harmonic radar transponders, such as the four Schottky diodes listed in Table 4.2. The last two columns of the table specify the selected ranges of SPICE parameters utilized for simulations. By conducting the analysis on two distinct ranges of variables, the significance of the selected range becomes more apparent. It should be noted that Range 2 was selected considering HMPS-

2820, while this particular diode is excluded in Range 1. Also, as demonstrated in Section 4.4, these six parameters have a direct impact on the *CL*. Other SPICE parameters have been excluded to prevent the dataset from becoming excessively large.

Table 4.2: Key SPICE parameters for some selected Schottky diodes and two selected ranges for DoE.

Parameter	MA4E 2502L	SMS7630 -079LF	HSMS- 2850	HMPS- 2820	Range 1	Range 2
C_{j0} (pF)	0.01	0.14	0.18	0.7	$0.01 \sim 0.2$	$0.01 \sim 0.7$
R_s (Ω)	12.8	20	25	8	$5 \sim 30$	$5 \sim 30$
I_s (μA)	0.026	5	3	0.022	$0.02 \sim 6$	$0.02 \sim 6$
V_j (V)	0.08	0.34	0.35	0.65	$0.05 \sim 0.35$	$0.05 \sim 0.65$
L_s (nH)	0.45	0.7	2	2	$0.3 \sim 2$	$0.3 \sim 2$
C_p (pF)	0.09	0.16	0.08	0.08	$0.08 \sim 0.2$	$0.08 \sim 0.2$

4.5.2 Generating the Database by Simulation

Once the SPICE parameters are varied and their appropriate ranges have been identified, it is necessary to determine the number of steps for each parameter to be swept. Opting for a significant number of steps results in an excessively large dataset, leading to longer simulation times without yielding any advantages. Conversely, employing too few steps can result in the loss of valuable information, such as the variability of *CL* across different parameter values. In this scenario, each variable that is a SPICE parameter is divided into five steps, resulting in a dataset containing $5^6 = 15625$ observations. To ensure optimal parameter selection for parameters with a wide range, it is advisable to use logarithmic steps.

As depicted in Table 4.3, each observation (set of SPICE parameters) corresponds to a *CL*. In this context, the SPICE parameters are referred to as regressors or explanatory variables, while the *CL* is termed the response variable. The response variable based on the explanatory variables is determined using harmonic balance simulation, which involves sweeping the SPICE parameters. ADS offers the conve-

nient option to export the dataset as a ".csv" file, which is highly advantageous as it can be utilized in other software for statistical analysis purposes. It is worth noting that the dataset is generated at a specific value of V_{oc} = 19 mV. This particular value corresponds to the V_{oc} obtained from the measurements conducted in Chapter 3. Selecting a constant voltage significantly reduces the dataset's size without compromising its generality because the effect of most SPICE parameters on *CL* remains largely independent of the V_{oc} value. Although there are exceptions, such as the parameter V_j, as discussed in Section 4.2.2, the single V_{oc} approach is generally sufficient for performing DOE.

Table 4.3: The dataset of CL versus diode SPICE parameters for DOE analysis.

Observations	C_{j0} (pF)	R_s (Ω)	I_s (μA)	V_j (V)	L_s (nH)	C_p (pF)	CL (dB)
1	0.01	12.8	0.026	0.08	0.45	0.09	4.5
2	0.04	12.8	0.026	0.08	0.45	0.09	8.8
⋮	⋮	⋮	⋮	⋮	⋮	⋮	⋮
15625	0.2	30	6	0.35	2	0.2	67.8

4.5.3 Implementing DOE using R

After generating the dataset, the relative importance of the SPICE parameters that act as predictors should be determined based on their effect on *CL*. Therefore, *CL* serves as the response variable. This analysis can be performed using established algorithms available in programming languages such as R. One such algorithm is *random forest*. Before explaining the Random Forest algorithm, understanding the basics of the decision tree is required. A decision tree is a simple yet powerful machine learning algorithm used for both classification and regression tasks. It works by recursively dividing the dataset into smaller and more homogeneous subsets based on the features of the data. Now, Random Forest combines the power of multiple decision trees to make more accurate predictions. It builds many trees, each trained

on a different random subset of data. To make a prediction, all trees in the forest *vote* on the outcome, and the most popular prediction wins [100].

To use this algorithm, the first step involves fitting a random forest model to the dataset. Subsequently, the relative importance of predictors can be calculated by passing the fitted regression model as an argument to the appropriate function. The code to implement this analysis can be found in Appendix A. The bar charts shown in Figure 4.9a and Figure 4.9b provide a summary of the relative importance analysis conducted using the random forest method for two sets of selected ranges of SPICE parameters. The significance, expressed as a percentage, is indicated at the top of each bar, with a total sum of 100. The results for the first range indicate that the package elements exhibit the greatest influence in determining the *CL*, followed by C_{j0} and V_j. On the other hand, I_s and R_s are identified as the parameters with the least importance. As seen in the chart, L_s is significantly more important than R_s. This is due to its much higher associated reactance, specifically $\omega L_s \gg R_s$. In the second range, Figure 4.9b, the importance of C_{j0} is higher due to its wider range.

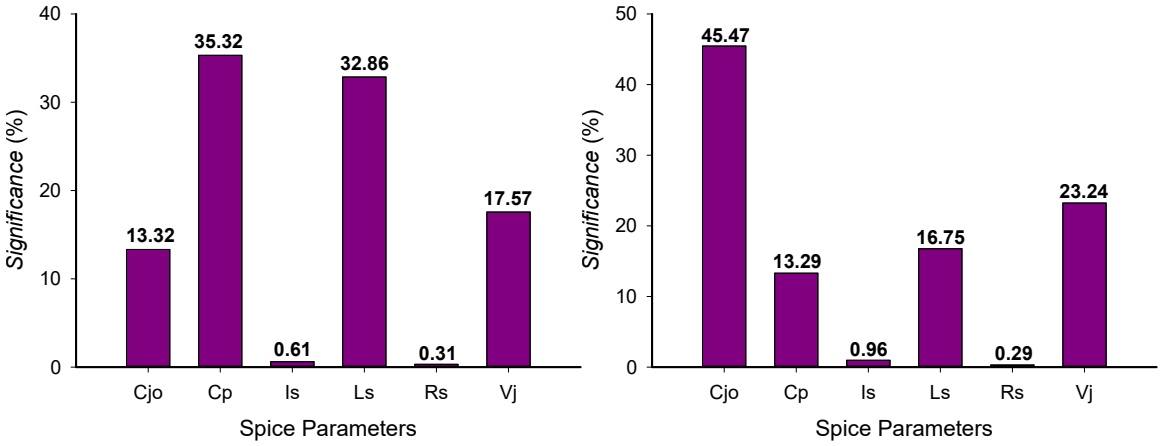


Figure 4.9: Relative importance of diode SPICE parameters in CL derived from a) range 1 b) range 2.

A random forest model was specifically chosen for this analysis, despite the availability of simpler and faster linear models. The decision to use a random forest model

was driven by the need to capture complex relationships and interactions among variables, which a linear model may not adequately capture, such as the correlation between C_{j0} and potential. However, it is important to consider that fitting a random forest model can be computationally intensive, particularly as the dataset size increases. This can pose challenges, especially when working with average computer hardware, as the training process may require significant computational resources and time.

4.6 Conclusion

In summary, when a transponder is exposed to radiated power, it exhibits two distinct power regions known as the low- and high-power regions. The boundary between these regions, referred to as the knee point, is primarily determined by the value of V_j. A higher V_j expands the region with a slope of two and leads to an increase in *CL*. The measurements conducted on the diode along the microstrip line reveal that as the RF power reaches a specific point, the *CL* also increases. Another finding pertains to the relative significance of SPICE parameters. It has been established that the value of the diode's parasitic or package elements, in addition to V_j and C_{j0}, plays a critical role in the overall performance of the transponder. These elements have a substantial impact on impedance matching and efficiency. The three most crucial parameters are capacitances (whether it is C_{j0} or C_p), L_s, and V_j. The diode with the minimum values for these parameters should be chosen, while also ensuring that it can handle the maximum anticipated drive levels. Thus, it is crucial to carefully consider and optimize these parasitic elements to maximize the transponder's performance and achieve optimal results.

Chapter 5

The Impact of Transponder Deformation on Detection Performance

5.1 Introduction

A dipole constructed using a thin metallic wire is susceptible to various forms of deformation. While certain measures have been explored to mitigate this issue, such as utilizing super-elastic nitinol wire to create a lightweight transponder resistant to deformation [51], this approach can result in reduced antenna efficiency, particularly at higher frequencies, due to increased conductor loss. Instead of focusing on engineering a deformity-resistant transponder, the objective of this chapter is to investigate the impact of deformation on the detectability and performance of a transponder constructed with either copper or stainless steel materials.

There are countless potential deformation patterns that can be envisioned for a metallic wire, but only a fraction of them warrant investigation from a practical standpoint. Moreover, the specific shape of deformation is influenced by the material

and thickness of the wire. Thin wires exhibit faster deformation and easier recovery to their original shape compared to thicker wires. As the wire thickness increases, deformation becomes more permanent, rendering the transponder susceptible to multiple deformations that lead to unpredictable and generally compromised performance, and even breaking the connections to the diode. Severe deformations can result in one or more contact points occurring at different locations on the dipole. These deformations alter the electrical length of the dipole, affecting both the radiation pattern and the impedance matching of the dipole. Consequently, there is a significant increase in harmonic *CL*. This type of deformation is more likely to occur in dipoles made with thicker wires that can retain their shape. The decision to focus the study on the simplified case of bend(s) is justified by two reasons. Firstly, intricate shapes are less likely to occur in ultra-thin wires as they do not retain the deformed shape and eventually convert into one of the simpler bend configurations that are discussed. Secondly, complex deformations can be approximated by a bend shape model that exhibits similar behavior to some extent.

In this chapter, the focus is on a more common set of deformations, referred to here as bends, which are detailed in Section 5.2. In Section 5.3, the influence of deformation on the dipole impedance as well as impedance matching is briefly investigated, along with some illustrative examples. Additionally, the numerical value of the harmonic *CL* is computed. If either one or both arms of a transponder are affected by deformation, it can impact the radiation pattern. The examination of how deformation influences the radiation pattern in such cases is presented in Section 5.4. To validate the simulation results, the radiation pattern of a transponder with a bend in one arm was measured in an ATC. The measurements were conducted at two different planes, and the findings are presented and summarized in Section 5.5. This experimental validation helps to ensure the accuracy and reliability of the simulated radiation patterns.

5.2 Definition and Modeling of the Bend

A simple bend can be characterized by three parameters, as depicted in Figure 5.1(a). The length of the deformed section, denoted as L, includes both curved and straight parts. The average radius of a cut of a torus that forms the curved section is represented by R, while the angle of the bend is denoted as θ, which is set to 45° in the figure for illustration purposes. This definition effectively models a sharp bend by selecting a small value for R and a complete curve in the arm by setting $L = \theta \cdot R$, where θ must be in radians. Figures 5.1(b) and (c) display two examples of bends, both with $\theta = 135°$ and equal L, representing a sharp bend and a complete curved bend, respectively. The radiation pattern of a transponder incorporating a $\theta = 90°$ bend is examined in Section 5.4.2.

To simplify the modeling process, deformations are represented using a combination of a cut from a torus and a cylinder. While more complex topologies like helix, elliptical torus, and polynomial-shaped wires are technically feasible, they are not considered in this study. The chosen modeling approach strikes a balance between practicality and accuracy for the examination of deformation effects on the transponder.

5.3 Deformation and Impedance Matching

As mentioned previously, dipole deformation can have an impact on the dipole impedance, subsequently influencing the harmonic *CL*. In this section, the effect of deformation on the dipole impedance is investigated by simulating several deformed dipoles. Figure 5.2 illustrates the dipole impedance before applying any deformation, where the blue and red lines represent the real and imaginary components, respectively. This plot will be included alongside the impedance plots of the deformed transponders to demonstrate the impact of the examined deformation on the real and

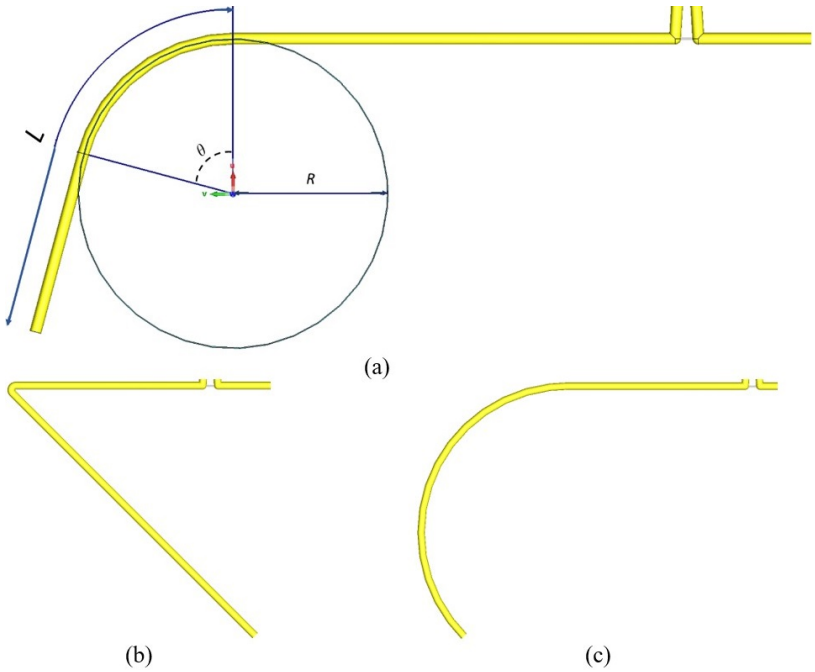


Figure 5.1: Modelling a simple bend in the transponder arm a) definition of three bend parameters, R, θ, and L b) a sharp bend with $\theta = 135°$ c) a complete curved bend with same θ.

imaginary components of the dipole impedance.

In order to investigate the impact of a mild deformation, a simulated transponder with deformation parameters of $L = 3\,\text{mm}$, $R = 0.05$ mm, and $\theta = 45°$ is examined. Figure 5.3 presents the impedance of both the deformed and undeformed transponders. The plot illustrates that there is a negligible change in impedance, particularly at the frequencies f_0 and f_h. Consequently, the harmonic CL is expected to remain almost unaffected by this mild deformation.

When a significant portion of the dipole is affected, the deformation is considered severe. Figure 5.4 displays the simulated impedance of a dipole with the deformation parameters set to $L = 9$ mm, $R = 0.05$ mm, and $\theta = 45°$. This severe deformation demonstrates a notable impact on the dipole impedance.

Upon closer examination of the impedance values at the f_0, it can be observed that there is a slight change in impedance due to a mild deformation. For the deformed transponder, the combination of dipole and loop impedance is approxi-

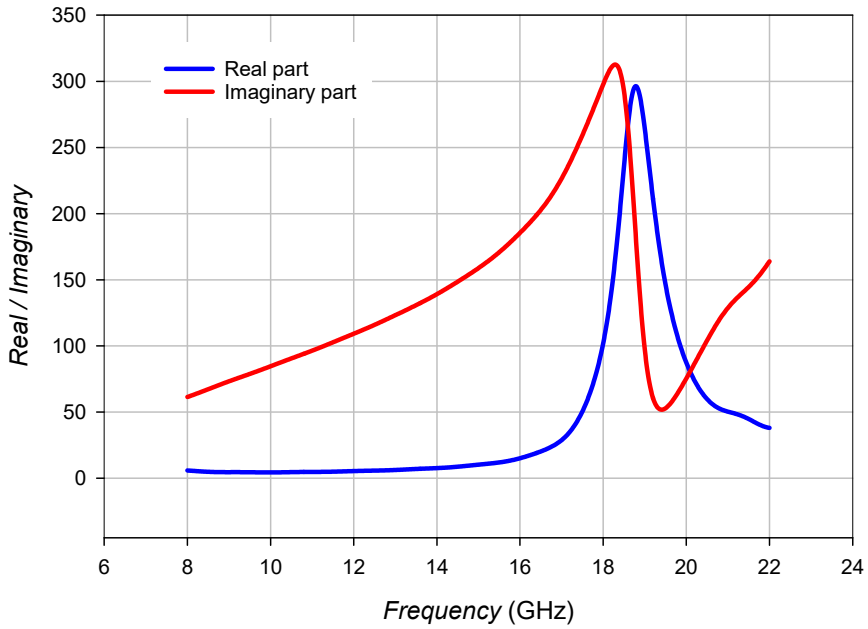


Figure 5.2: Impedance characteristics of an undistorted transponder, where the blue and red lines represent the real and imaginary components, respectively.

mately $Z_{0,\mathrm{d}} \approx 2.8 + j91\,\Omega$, whereas for the undeformed case, it is approximately $Z_0 \approx 4.46 + j90\,\Omega$. However, at f_h, the difference between the impedance of the deformed and undeformed transponders becomes more significant. According to the simulation results, the impedance for the undeformed transponder is approximately $Z_\mathrm{h} \approx 90 + j71\,\Omega$, while for the deformed transponder, it is approximately $Z_{\mathrm{h,d}} \approx 35 + j105\,\Omega$.

Referring to the link analysis in Chapter 3, the harmonic *CL* for a deformed transponder can be determined through simulation and calculation. The impedance values and the corresponding harmonic *CL* are presented in Table 5.1. The results indicate an increase of approximately 2.5 dB in loss due to the deformation. The given value would not have a substantial impact on the detection range and is not considered to be very high.

Based on this analysis, it can be concluded that deformation has a minimal impact on the dipole impedance. A 45° bend at the end of the arm exhibits negligible effects on the impedance, while a bend near the center feed moderately alters the impedance,

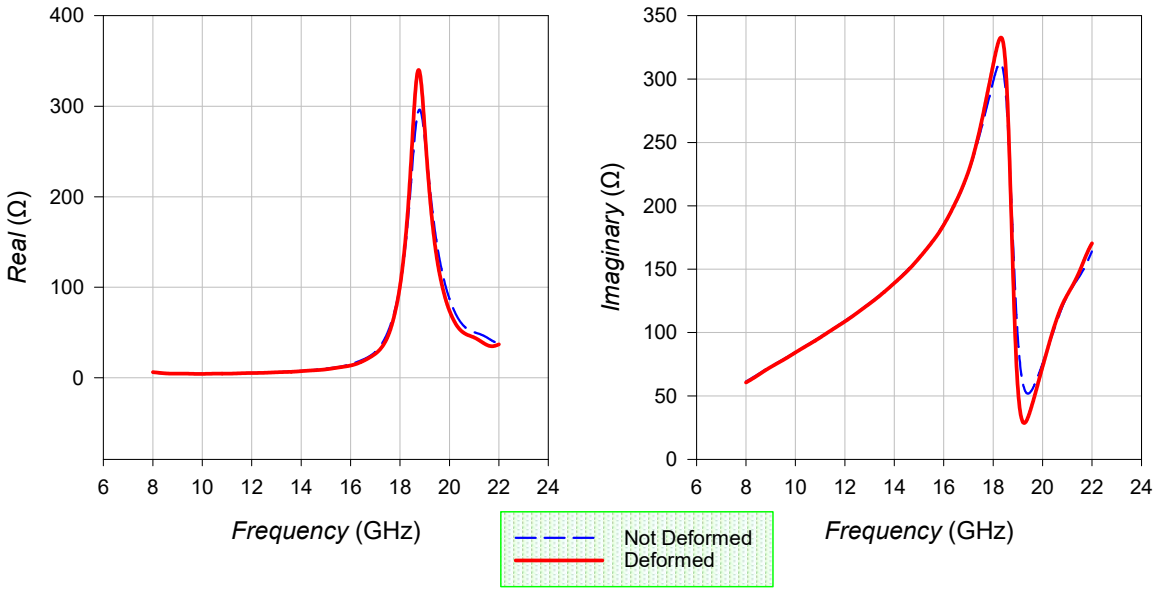


Figure 5.3: Comparison of impedance characteristics between an intact transponder (blue lines) and a slightly deformed transponder (red lines).

Table 5.1: Impedances at f_0 and f_h and resulting CL for a mildly deformed transponder ($L = 9$ mm, $R = 0.05$ mm, $\theta = 45°$).

Parameter	Undeformed	Deformed
$Z_0(\Omega)$	$4.46 + j90$	$2.8 + j91$
$Z_h(\Omega)$	$90 + j71$	$35 + j105$
Harmonic CL (dB)	4.5	7

resulting in approximately 1 dB of mismatch loss. This observation is justified because as long as there is no contact between two points of the dipole, the electrical length of the dipole remains unchanged despite deformation.

5.4 Deformation and the Radiation Pattern

In addition to the dipole impedance, deformation also has an impact on the polarization and radiation pattern of the transponder. In this section, the significance of polarization under deformation is discussed first, followed by the directivity pattern at f_0 and f_h. In each case, the individual directivity patterns are provided, and the logarithmic sum of these patterns is plotted as the total directivity pattern. Specif-

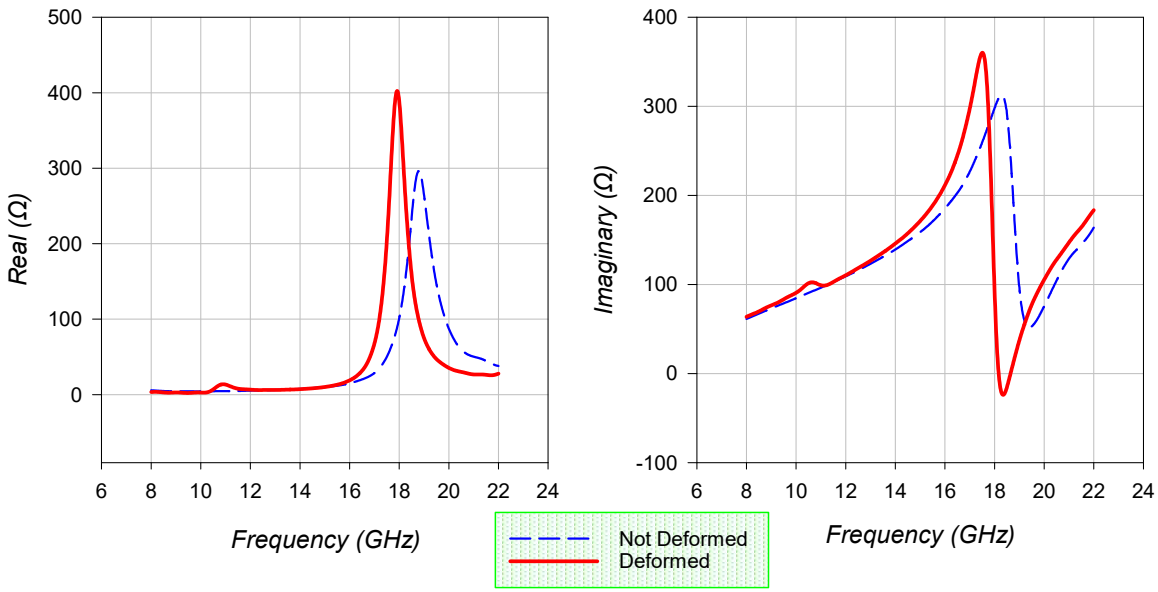


Figure 5.4: Comparison of impedance characteristics between an undistorted transponder (blue lines) and a highly deformed transponder (red lines).

ically, two cases are simulated: one with a sharp bend (small R) and another with a curved bend at one arm. For deformations affecting both arms, a specific case is selected and simulated.

5.4.1 Deformation and Transponder Polarization

In the absence of deformation, a dipole antenna exhibits purely linear polarization, and there are no polarization losses if the radar antennas are co-polarized with the transponder. However, in the case of a deformed transponder, the deformation affects its polarization, causing it to become elliptical.

Simulating the radiation pattern of a deformed transponder requires accurately selecting the polarization of the antenna used to characterize the transponder's radiation pattern. This selection is made when plotting the radiation pattern after completing the simulation. The polarization of the receiving antenna can be chosen from options such as linear, slant linear, Left Hand Circular Polarization (LHCP), and Right Hand Circular Polarization (RHCP). For example, when a linear polarization

is selected for the receiving antenna, the resulting radiation pattern aligns with the measured radiation pattern when the harmonic radar utilizes two linearly polarized antennas at frequencies f_0 and f_h.

When the transponder is not deformed, employing a circularly polarized antenna in harmonic radar ensures consistent reception regardless of the alignment of the transponder. However, using a circularly polarized antenna results in a power reduction of 3 dB at the frequencies f_0 and f_h in comparison to a linearly polarized antenna with perfect polarization alignment. It should be noted that when communicating between a linearly polarized and a circularly polarized antenna, a polarization mismatch loss of 3 dB occurs. In the case of a deformed transponder, the deformation affects the polarization of the dipole antenna, causing it to deviate from purely linear polarization. In these cases, a circularly polarized radar antenna performs better.

To ensure an accurate simulation of the radiation pattern, it is crucial to correctly define the polarization of the receiving antenna. In this study, the measurements were conducted using two linearly polarized horn antennas. Therefore, it is necessary to maintain the same polarization definition in the simulation to match the measurements. In measurements, the primary focus is on linearly polarized harmonic radar antennas, as they are more commonly used. However, circular polarization will also be briefly explored in the simulations.

5.4.2 A Sharp Bend at one Arm and the Radiation Pattern

By selecting $R = 0.05$ mm, a sharp yet practical bend is achieved on the dipole made out of thin wire. As an example, the radiation pattern of a transponder with bend parameters of $L = 6$ mm and $\theta = 90^\circ$ is simulated to demonstrate the impact of a sharp bend at one arm. The transponder configuration exhibiting such a bend is depicted in Figure 5.5. Through this example, our aim is to visualize the resulting radiation pattern of a transponder subjected to the specified deformation.

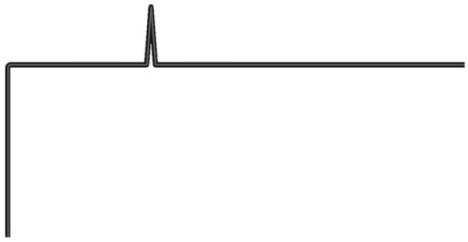


Figure 5.5: Transponder featuring a sharp arm bend with bend parameters: $R = 0.05$ mm, $L = 6$ mm, and $\theta = 90°$.

To accurately represent the elevation plane radiation pattern of the deformed transponder, it is necessary to plot the pattern at least at two perpendicular elevation planes due to the non-symmetrical structure of the transponder. In all of the radiation pattern plots that follow, when plotting at two perpendicular planes is required, the top and bottom rows of patterns correspond to the two perpendicular planes. Furthermore, the radiation pattern needs to be plotted at two frequencies: f_0, f_h, and the sum of these patterns in a logarithmic scale. The figures will consist of three columns, with the first column displaying the pattern at f_0, the second column displaying the pattern at f_h, and the third column displaying the sum pattern. To aid in understanding the alignment of the transponder in each elevation plot, the sum pattern will include a background illustration of the transponder. However, in azimuth plots, where there is only one alignment for the transponder, the background photo is not necessary. Additionally, to provide a reference, the radiation pattern of an undeformed deformed transponder will be included as a dashed red line in all plots. This allows for a visual comparison between the deformed and undeformed transponder patterns.

Figure 5.6 presents the directivity pattern of the transponder illustrated in Figure 5.5 at two perpendicular elevation planes. These plots depict the radiation pattern when RX antenna has a linear polarization at both f_0 and f_h, and is aligned with the undeformed part of the deformed dipole.

Figure 5.7 shows how the polarization of the harmonic radar antennas affects the

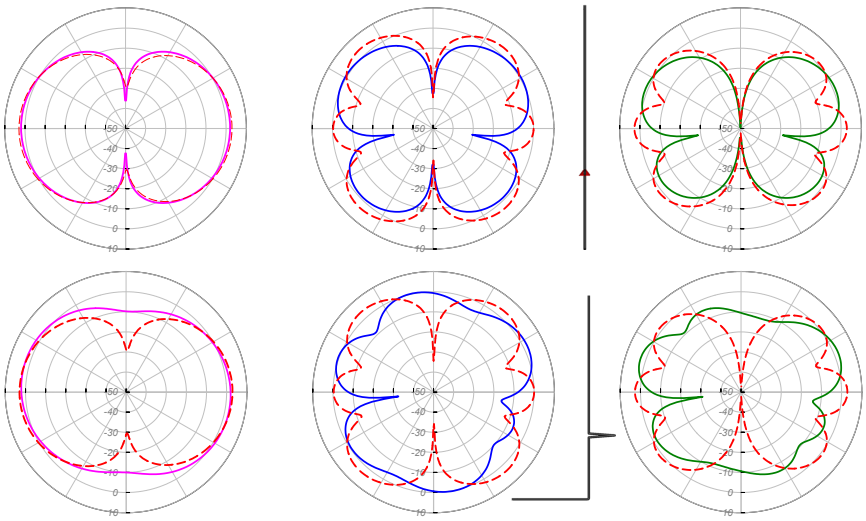


Figure 5.6: Elevation plane directivity pattern of a transponder with a sharp bend, utilizing radar antennas with linear polarization; dashed line is the non-deformed pattern.

radiation pattern of a deformed transponder. In this figure, the radiation pattern of the transponder in Figure 5.5 is plotted with the consideration of radar with two LHCP antennas. Like Figure 5.6, this figure also contains two perpendicular elevation planes and the pattern at f_0, f_h, and the sum pattern at the third column.

Comparing Figure 5.6 and Figure 5.7 explains the effect of deformation on the transponder polarization. While the first row of the plots in these figures is different, the second row is similar, with a 3 dB lower amplitude in Figure 5.7. In other words, substituting the linearly polarized antennas of a harmonic radar with the circularly polarized antennas changes the radiation pattern at a specific plane, the first row, and it is not changing in another plane, the second row.

The reason for observing different patterns at one plane and similar patterns at the other is the variation in transponder polarization at these perpendicular planes. In order to illustrate this phenomenon, Figure 5.8 showcases the simulated axial ratio of the deformed transponder at these two planes for radar with twoLHCP antennas. It is important to note that the maximum axial ratio value reported by CST is 40 dB.

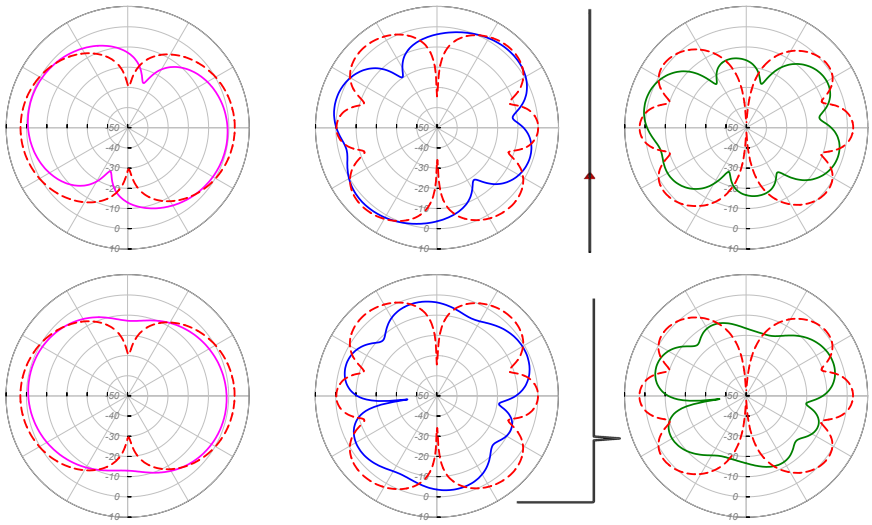


Figure 5.7: Elevation plane directivity pattern of a transponder with a sharp bend, employing LHCP antennas in the radar system; dashed line is the non-deformed pattern.

Consequently, in instances where the polarization is nearly linear, CST reports a value of 40 dB. This can be observed at certain points in the first row and every point in the second row.

Observing Figure 5.8 reveals that the first row in many directions exhibits circular or elliptical polarization, whereas the second row demonstrates absolute linear polarization at both frequencies, f_0 and f_h. A comparison of these plots with the axial ratio plots of the undeformed transponder, as provided in Figure 3.9, reveals a closer resemblance to circular polarization. Consequently, when dealing with a deformed transponder, incorporating a circularly polarized antenna in radar systems can enhance reception in certain directions for the first row, although not uniformly in all directions. This will be further elucidated later on.

When using a circularly polarized radar antenna in the second row of Figure 5.8, since polarization of the transponder is dominantly linear, there is a decrease in the received power by 6 dB without changing the shape of the radiation pattern. This reduction is caused by two polarization mismatch losses between linear and circular

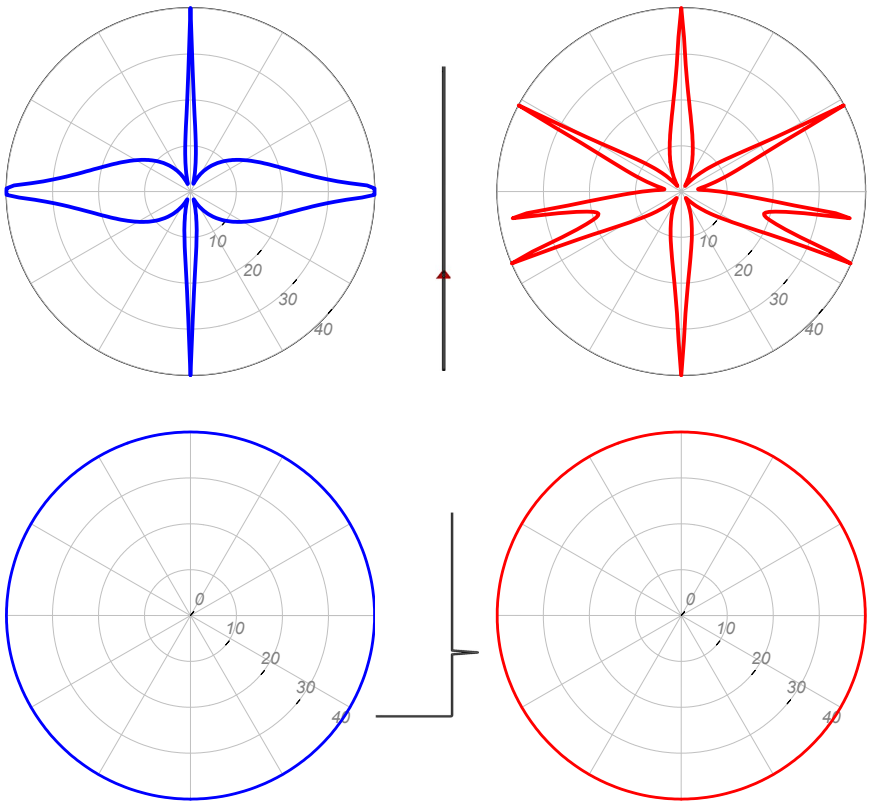


Figure 5.8: Simulated axial ratio of a deformed transponder at two orthogonal elevation planes using LHCP radar antennas. The left and right columns depict frequencies f_0 and f_h, respectively.

antennas, with each loss accounting for 3 dB. Additionally, if the received power falls within the low-power region, there is an extra 3 dB loss due to harmonic conversion, resulting in a total power loss of 9 dB.

As previously mentioned, employing a circularly polarized harmonic radar antenna does not necessarily lead to an increase in received power. By comparing the first rows of Figure 5.6 and Figure 5.7, the direction of circular polarization in the analyzed deformed transponder can be determined, whether it is LHCP or RHCP. In this simulation, two LHCP antennas are assumed for the radar. Hence, if the deformed transponder exhibits RHCP, it will result in attenuation. In the extreme case where one antenna is purely RHCP and the other is purely LHCP, they are essentially cross-polarized. Consequently, even though the deformed transponder demonstrates

circular polarization, using a circularly polarized radar antenna can have adverse effects in specific directions due to the mismatch in the direction of circular polarization. As a final point on this matter, it is important to note that the examined deformed transponder exhibits both RHCP and LHCP depending on the angle. Therefore, it is not possible to prescribe the use of a radar antenna with a specific circular polarization.

The directivity pattern of the deformed transponder depicted in Figure 5.5 can be observed at the azimuth plane through Figure 5.9 for linearly polarized harmonic radar antennas, and Figure 5.10 for LHCP harmonic radar antennas. The presence of nulls in the second and third columns of the pattern shown in Figure 5.10 can be explained by the mismatch between the direction of circular polarization of the radar antennas and the transponder. In this case, the radar antennas are assumed to have a purely LHCP, resulting in attenuation when receiving the RHCP wave emitted by the transponder.

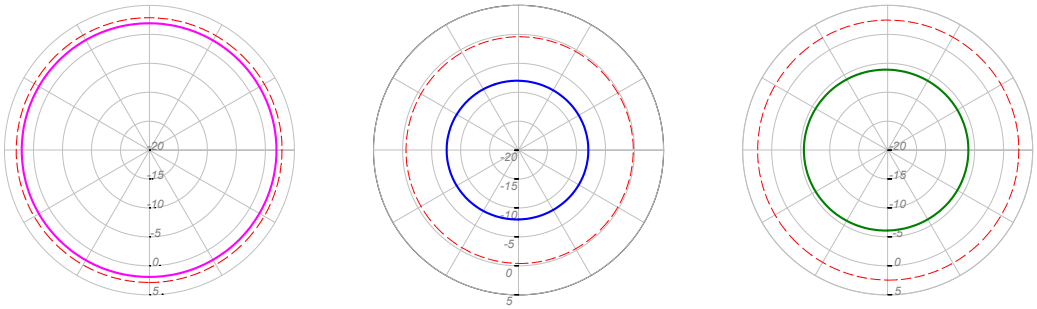


Figure 5.9: Azimuth plane directivity pattern of a transponder featuring a sharp bend, with a linearly polarized radar antennas; dashed line is the non-deformed pattern.

Finally, a thorough analysis of the plotted directivity patterns reveals that the pattern at the f_{h} is highly susceptible to deformation, leading to the emergence of nulls in the overall radiation pattern. Additionally, while the utilization of circularly polarized antennas in harmonic radar systems can enhance the radiation pattern at certain points, it can also introduce undesired nulls in the overall radiation pattern. Predicting the specific location and magnitude of these generated nulls is not always

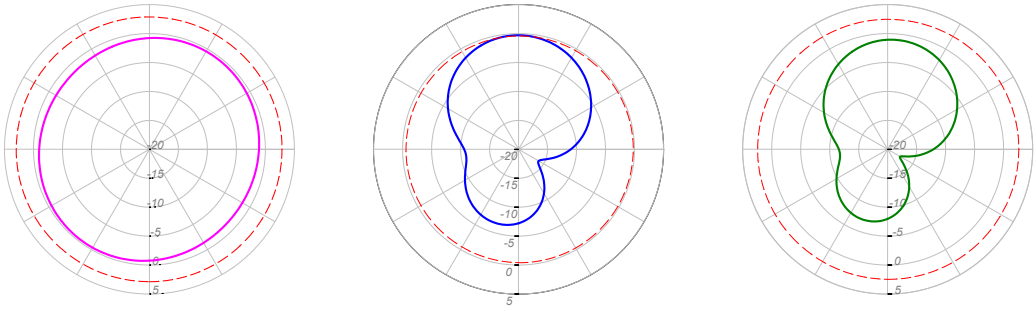


Figure 5.10: Azimuth plane directivity pattern of a transponder with a pronounced bend, utilizing LHCP antennas in the radar system; dashed line is the non-deformed pattern.

a straightforward task.

5.4.3 A Curved Bend at one Arm and the Radiation Pattern

Another potential type of deformation that can occur in the transponder is a curved bend. To explore this scenario, the bend parameters of $R = 2.86$ mm, $L = 9$ mm, and $\theta = 180°$ are selected, resulting in a curved bend applied to one arm of the transponder. The corresponding transponder with a curved bend is depicted in Figure 5.11. The radiation pattern of the transponder affected by this curved bend is then simulated and plotted at the same planes that were previously used for the case of a sharp bend.

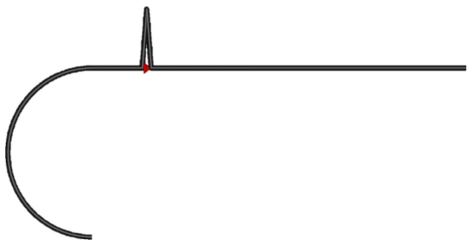


Figure 5.11: Transponder featuring a curved arm bend with bend parameters: $R = 2.86$ mm, $L = 9$ mm, and $\theta = 180°$.

Figure 5.12 showcases the directivity pattern of the transponder depicted in Figure 5.11 at two perpendicular elevation planes. These plots correspond to a scenario where RX antenna is linearly polarized, aligning the electric field vector parallel to

the undeformed section of the dipole. In order to examine the influence of radar antenna polarization on the directivity pattern, Figure 5.13 illustrates the radiation pattern of the same transponder when a LHCP antenna is employed in the harmonic radar.

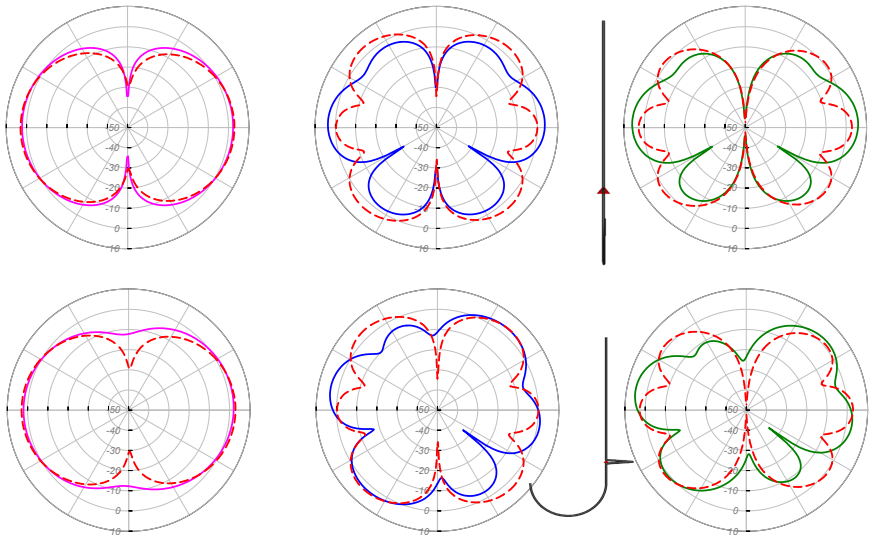


Figure 5.12: Elevation plane directivity pattern of a transponder with a curved bend, employing a linearly polarized radar antennas; dashed line is the non-deformed pattern.

Upon comparing the plots in Figure 5.12 and Figure 5.13 with the plots of a transponder with a sharp bend, it becomes evident that they exhibit a similar overall shape. The number of main and side lobes, as well as the presence of nulls, closely resemble each other. The nulls do not tend to be as deep, and the antenna becomes increasingly omnidirectional, though the maximum performance may be reduced. This implies that both the sharp bend and the curved bend have a similar effect on the transponder. The impact of utilizing a circularly polarized antenna on the transponder pattern aligns with the observations made in the previous case of a sharp bend. Therefore, there is no need to repeat those findings here.

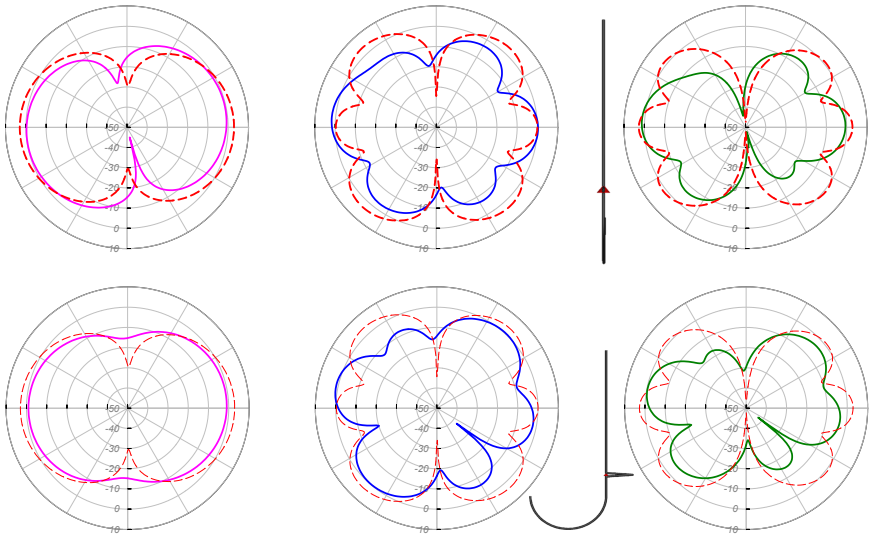


Figure 5.13: Elevation plane directivity pattern of a transponder featuring a curved bend, with radar employing two LHCP antennas; dashed line is the non-deformed pattern.

5.4.4 Bends at both Arms and the Radiation Pattern

The final case to be simulated in this chapter involves deformation at both arms of the transponder. This scenario consists of two identical bends, one at each arm, with bend parameters set as $R = 1.5$ mm, $L = 6$ mm, and $\theta = 90°$, as illustrated in Figure 5.14.

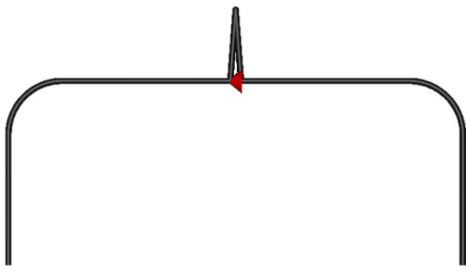


Figure 5.14: Transponder with bends at each arm, characterized by bend parameters: $R = 1.5$ mm, $L = 6$ mm, and $\theta = 90°$.

Taking into account the linear polarization of the harmonic radar antennas, the directivity pattern of the transponder affected by deformation at both arms is simulated and displayed in Figure 5.15 at two perpendicular elevation planes. These

patterns reveal that in the second row of plots, the number of nulls is reduced, and the pattern tends to approach an omnidirectional pattern. However, in contrast to the second row, the axial nulls are not eliminated in the first row. This is because the propagation from the deformed part of the transponder becomes cross-polarized in relation to the radar antennas.

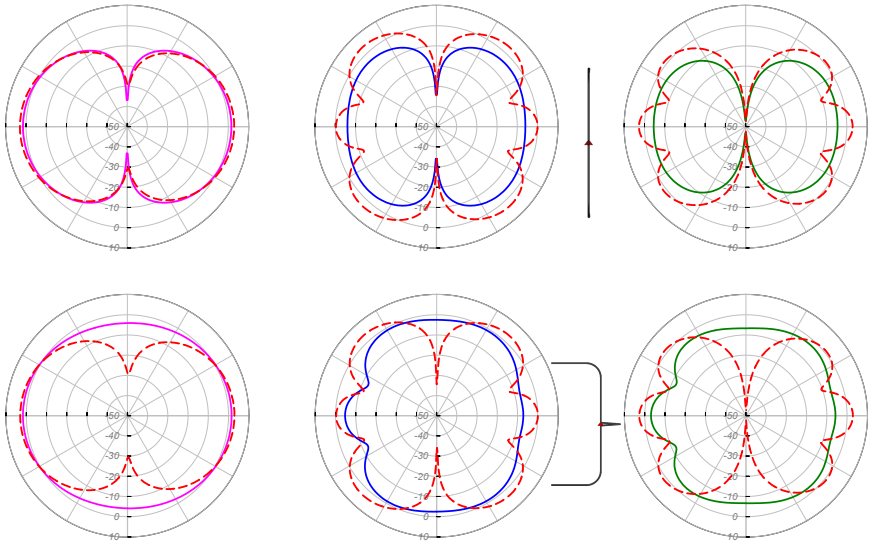


Figure 5.15: Elevation plane directivity pattern of a transponder featuring a single bend at each arm, utilizing linearly polarized radar antennas; dashed line is the non-deformed pattern.

Figure 5.16 illustrates the simulated directivity pattern of the same transponder when a harmonic radar with LHCP antennas is employed. As anticipated, the second row of this figure resembles the second row of plots in Figure 5.15, with an additional 3 dB loss at f_0 and f_h due to the polarization mismatch between the circularly polarized radar antenna and the linearly polarized transponder. However, the first row of plots in Figure 5.15 and Figure 5.16 differ. In the simulation plane corresponding to this row, the transponder polarization is closer to circular polarization at various angles, as depicted in Figure 5.17. Consequently, substituting the linearly polarized antennas of the harmonic radar with circularly polarized antennas impacts the radiation pattern. As discussed earlier, the effect also relies on the direction of circular

polarization, whether it is LHCP or RHCP. swapping between LHCP and RHCP would result in different radiation patterns.

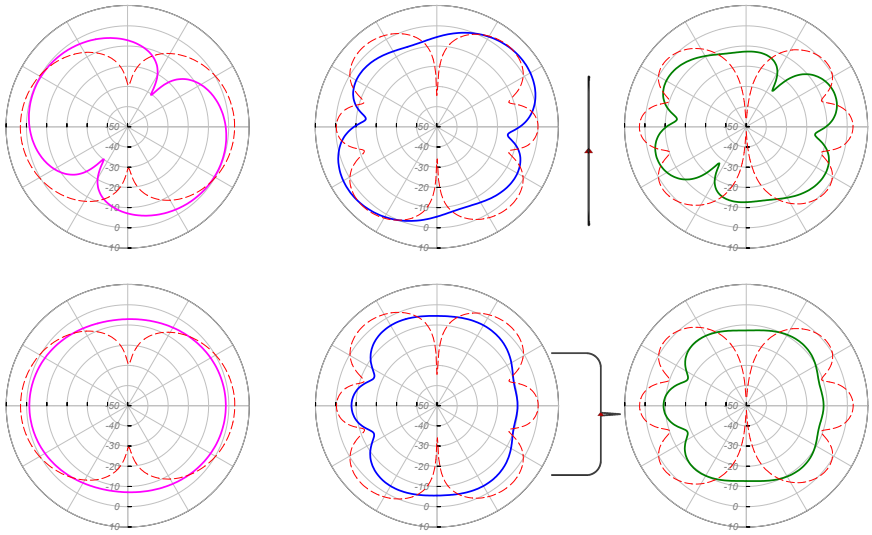


Figure 5.16: Elevation plane directivity pattern of a transponder featuring a single bend at each arm, with two LHCP antennas on the radar system; dashed line is the non-deformed pattern.

5.5 Measurement

When measuring the radiation pattern of a deformed transponder, similar to an undeformed transponder as described in Chapter 3, some considerations need to be taken into account. First, it is necessary to measure the radiation pattern in at least one additional plane to accommodate the non-symmetry resulting from the deformation. This means that the radiation pattern should be measured in two perpendicular elevation planes, just as in the simulation. Second, deformation may introduce additional side lobes and minor lobes that can be challenging to accurately capture using the previous measurement setup. Reducing the noise floor during the measurement process can help in capturing the low-power minor lobes. Lastly, it should be noted that achieving an exact replication of the deformation based on the

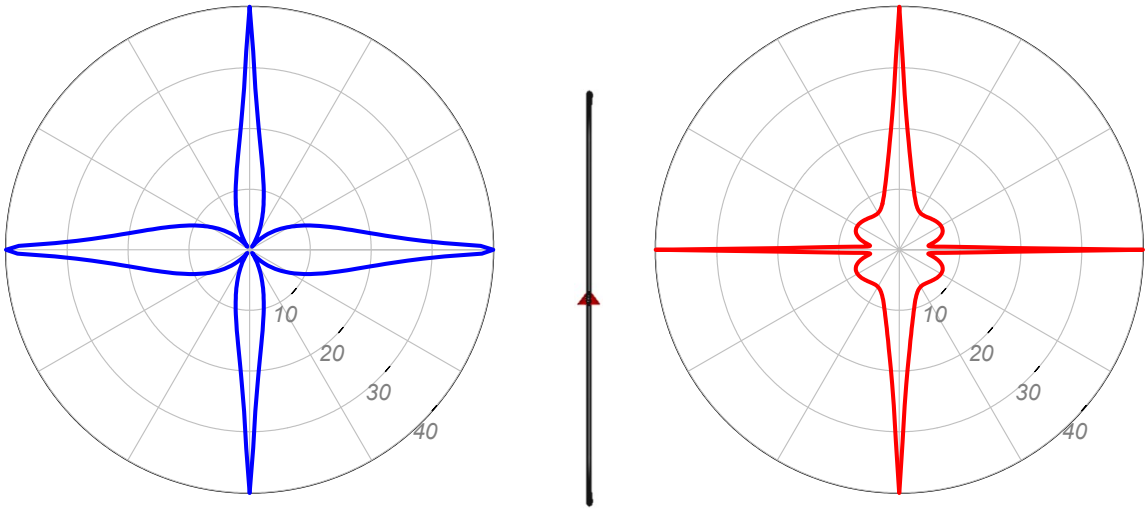


Figure 5.17: Simulated axial ratio of a deformed transponder with bends at each arm, evaluated at the elevation plane. The plot depicts circular polarization at multiple points.

specific values of R, θ, and L used in the simulation may not be feasible in the measurement setup. As a result, a higher level of discrepancy between the simulation and measurement results can be expected.

In order to enhance the accuracy of the measurement process for a deformed transponder, relative to the measurement setup in Chapter 3, two changes were implemented: a modification in the transponder mounting structure and adjustments to the VNA settings. Firstly, the styrofoam stand, which was previously used to support and secure the transponder in the correct polarity, was replaced with a piece of paper, as depicted in Figure 5.18. It should be noted that mounting the transponder on the paper requires more time to ensure precise positioning, and any misalignment could introduce measurement errors. On the other hand, using styrofoam can affect the reception and propagation of the transponder, particularly when it is positioned between the harmonic radar TX and RX antennas and the transponder itself. Thus, eliminating the styrofoam improves the accuracy of the measurements.

The second modification aimed to reduce the noise floor of the VNA in order to improve the detectability of weaker received signals. This was achieved by decreasing



Figure 5.18: Placing the transponder on a sheet of paper to mitigate the impact of styrofoam on the radiation pattern.

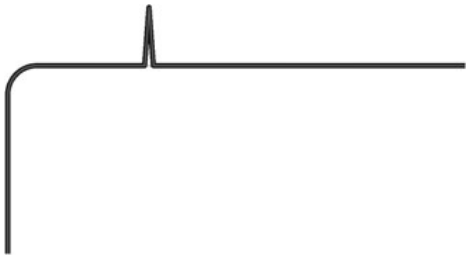
the VNA IF bandwidth, which can be done through the averaging menu. Lowering the IF bandwidth is equivalent to reducing the resolution bandwidth (RBW) which is the minimum bandwidth over which two signals can be separated and still visible. In fact, RBW affects the kTB noise floor power where k is Boltzmann's constant, T is the temperature in Kelvin (K), and B is bandwidth in Hz. kTB power changes 10 dB per decade change in B.

Table 5.2 provides the lowest selectable values of IF bandwidth and their corresponding noise floors in the VNA. The middle column indicates the appropriate number of points that should be selected to synchronize the position of the antenna rotator and the data sampled by the VNA. As the IF bandwidth decreases, the sweep time of the VNA increases. Consequently, a lower number of points must be selected to ensure synchronization between the antenna rotator and the VNA.

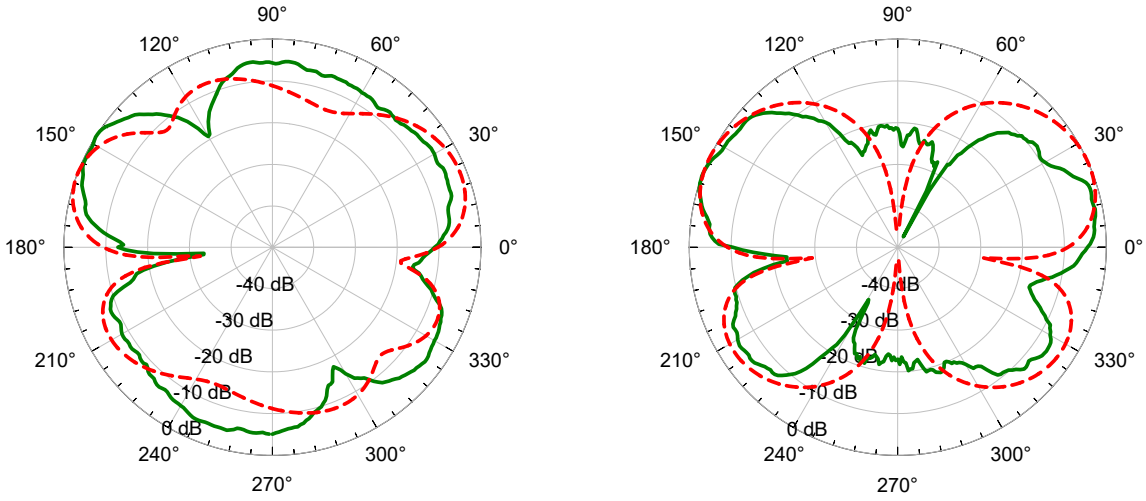
Table 5.2: IF Bandwidth and corresponding noise floor.

IF Bandwidth	# of points	Noise floor
5 Hz	360	-110 dBm
3 Hz	180	-112 dBm
1 Hz	72	-117 dBm

In Figure 5.19a, a transponder with a bend in one arm is depicted, where the bend parameters are $L = 7$ mm, $R = 1$ mm, and $\theta = 90°$. The corresponding measured radiation pattern in the elevation plane, as well as two perpendicular planes, along with the simulation result, are presented in Figure 5.19b. The measurement was conducted with a transmitted power of 22 dBm, which represents the maximum available power. Notably, there is a strong agreement between the simulated and measured radiation patterns in both planes, demonstrating the accuracy of the simulation in capturing the real-world behavior of the transponder.



(a)



(b)

Figure 5.19: Radiation pattern measurement for a deformed transponder: (a) Deformed transponder ($L = 7$ mm, $R = 1$ mm, and $\theta = 90°$) (b) Elevation pattern in two perpendicular planes, including simulation (dashed).

5.6 Conclusion

To ensure accurate performance estimation of a transponder with thin metal, it is crucial for designers to consider the potential performance degradation caused by deformation. Overestimating the maximum detection range should be avoided considering the possibility of transponder deformation. When evaluating impedance matching and *CL*, minor deformations are unlikely to significantly impact performance. However, more substantial deformations will lead to a reduction in received power, though they may still fall within acceptable limits. The effects of deformation on the radiation pattern and polarization are more intricate. Deformation can alter the radiation pattern, reducing the depth or shifting of nulls in the pattern. The antenna becomes increasingly omnidirectional, though the maximum performance may be reduced. Additionally, it can influence the degree of polarization fading as the tagged insect moves. Overall, careful consideration and analysis of the effects of deformation on various aspects of the transponder's performance are essential in order to optimize its design and functionality.

Chapter 6

Conclusion

Reducing the mass of harmonic radar transponders has made them suitable for tracking increasingly smaller insects, such as mosquitoes, ladybugs, and fruit flies, as compared to the insects that could be tracked by previous transponders. Previously, tracking such insects was challenging due to their diminutive size. Understanding the dispersal patterns of insects, which hold economic significance, is of particular interest, both within and between fields. As discussed in Chapter 3, a transponder weighing 530 µg can significantly contribute to this endeavor, especially by maintaining its efficiency within an optimal range. Since flying insects can carry only a limited payload that depends on their mass, reducing the mass of a transponder enables entomologists to tag smaller insects. The simulation technique presented in this chapter, utilizing link analysis, is valuable for predicting and optimizing the transponder's performance. Additionally, the conducted measurements play a crucial role in validating the simulations. Notably, the introduced technique for measuring the radiation pattern provides a comprehensive understanding of the overall radiation pattern, surpassing the individual patterns previously observed.

In Chapter 4, two distinct power regions in a transponder exposed to radiated power are examined. It reveals that the boundary between these regions is primarily

determined by the diode junction potential. A higher junction potential adversely impacts the *CL* for a given drive level. Significantly, as the incident power density reaches a high level, the *CL* initially stabilizes and remains constant. However, for extremely high values, the *CL* starts to increase once again. This increase is primarily attributed to the dependency of C_{j0} to drive level. Additionally, it was concluded that diode parameters like parasitic/package components, junction potential, and C_{j0} are important. The crucial parameters to prioritize are C_p, L_s, and junction potential when selecting a diode. Opting for the diode with the smallest values for these parameters is essential.

Wire-type harmonic radar transponders are susceptible to deformation, which can significantly impact performance. In Chapter 5, various types of deformations and their effects on transponder impedance matching and radiation pattern are examined. The findings are further supported by measuring the radiation pattern in a specific case. Additionally, practical considerations for enhancing the measurement of the radiation pattern are also discussed. Simulation results indicate that mild deformation does not significantly impact the impedance of the transponder. In the case of radiation patterns, the impact of deformation becomes more complex. Deformation affects the polarization characteristics of the transponder, and the polarization of the radar antenna plays a crucial role in determining the reception from a deformed transponder. Consequently, a deformed transponder may vary in its detectability, exhibiting either an increased or decreased level of detectability. It is evident that a certain degree of deformation is beneficial, considering that the relative orientation of the transponder is anticipated to change during operation.

6.1 Future Work

Tackling the challenges of working at higher frequency ranges, such as the millimeter wave band, is undoubtedly worthwhile. It opens up opportunities to enhance the capabilities of radar systems by making them lighter and more compact. This not only improves portability but also provides a more precise spatial resolution, which is particularly valuable in scenarios where object tracking is of utmost importance. Additionally, higher frequency ranges enable the utilization of highly directional antennas, resulting in improved reception of signals and enhancing the overall performance of the radar system.

To assess the real-world performance of harmonic radar transponders, it is crucial to conduct field testing in the field with a real harmonic radar, which was not undertaken in this study. These tests are essential for evaluating the reliability, accuracy, and robustness of the system under diverse environmental conditions and insect behaviors. By collecting empirical data through field experiments, the effectiveness of the transponder technology can be validated for ecological studies and specific target insects. This data will provide valuable insights into the practical applicability of harmonic radar transponders and further support their utility in insect tracking and related research endeavors.

One challenge encountered when using a bare die Schottky diode is the soldering process required for its connection to the antenna. However, this type of diode offers the advantage of potentially higher efficiency, which can be attributed to the reduced C_{p} and L_{s}. While the wire constitutes a significant portion of the transponder mass, using a smaller diode can reduce the overall mass of the transponder. It would be more important at higher frequencies.

Using GaAs Schottky diodes could be also considered for improving the transponder performance due to their higher frequency operation and better temperature stability compared to the silicon Schottky diodes. It is important to note, however,

that GaAs Schottky diodes have an elevated value of V_{j}, which necessitates careful consideration, especially when the transponder is anticipated to function under low drive levels. This situation can result in heightened conversion loss due to the high V_{j}.

For further advancement in the discussed topic in Chapter 5, it would be helpful to analyze the radiation pattern more comprehensively, such as by utilizing the Poincaré sphere. The Poincaré sphere allows for a broader analysis of polarization, encompassing both circular and elliptical polarization. Note that circular polarization can be viewed as a specific case of the more general elliptical polarization, which involves a specific amplitude and phase relationship between the two polarization component vectors. By examining the radiation pattern in this manner, a deeper understanding of the polarization characteristics can be gained.

Bibliography

[1] A. Mishra and C. Li, "A review: Recent progress in the design and development of nonlinear radars," *Remote Sensing*, vol. 13, p. 4982, Dec. 2021.

[2] P. Nallabolu, L. Zhang, H. Hong, and C. Li, "Human presence sensing and gesture recognition for smart home applications with moving and stationary clutter suppression using a 60-GHz digital beamforming FMCW radar," *IEEE Access*, vol. 9, pp. 72857–72866, 2021.

[3] G. Boiteau and B. Colpitts, "Electronic tags for the tracking of insects in flight: effect of weight on flight performance of adult colorado potato beetles," *Entomologia Experimentalis et Applicata*, vol. 100, no. 2, pp. 187–193, 2001.

[4] R. Ala, C. D. Rouse, and B. G. Colpitts, "An extra low-mass harmonic radar transponder for insect tracking applications," *IEEE Transactions on Radar Systems*, pp. 1–1, 2023.

[5] R. Ala and B. G. Colpitts, "Development of extra low mass harmonic radar transponders," in *2021 IEEE 19th International Symposium on Antenna Technology and Applied Electromagnetics (ANTEM)*, (Winnipeg, MB, Canada), pp. 1–2, IEEE, Aug. 2021.

[6] R. Ala, B. G. Colpitts, and N. Kozma, "Evaluation and improvement of the performance of harmonic RADAR transponders," in *2020 IEEE International*

Radar Conference (RADAR), (Washington, DC, USA), pp. 659–664, IEEE, Apr. 2020.

[7] K. Gallagher, R. Narayanan, G. Mazzaro, A. Martone, and K. Sherbondy, "Static and moving target imaging using harmonic radar," *Electronics*, vol. 6, p. 30, Apr. 2017.

[8] M. Skolnik, *Introduction to Radar Systems*. McGraw-Hill, 2001.

[9] R. O. Hstger, "Harmonic radar systems for near-ground in-foliage nonlinear scatterers," *IEEE Transactions on Aerospace and Electronic Systems*, vol. AES-12, no. 2, pp. 230–245, 1976.

[10] D. Mascanzoni and H. Wallin, "The harmonic radar: a new method of tracing insects in the field," *Ecological Entomology*, vol. 11, pp. 387–390, Nov. 1986.

[11] J. Riley, "Remote sensing in entomology," *Annual review of entomology*, vol. 34, no. 1, pp. 247–271, 1989.

[12] R. Maggiora, M. Saccani, D. Milanesio, and M. Porporato, "An innovative harmonic radar to track flying insects: the case of vespa velutina," *Scientific Reports*, vol. 9, Aug. 2019.

[13] A. Noskov, J. Bendix, and N. Friess, "A review of insect monitoring approaches with special reference to radar techniques," *Sensors*, vol. 21, p. 1474, Feb. 2021.

[14] P. Z. Peebles Jr., *Radar Principles*. Wiley, 2004.

[15] L. Zhu, N. Alkhaldi, H. M. Kadry, S. Liao, and P.-Y. Chen, "A compact hybrid-fed microstrip antenna for harmonics-based radar and sensor systems," *IEEE Antennas and Wireless Propagation Letters*, vol. 17, no. 12, pp. 2444–2448, 2018.

[16] "Furuno." https://www.furuno.com. Accessed: November 14, 2023.

[17] "Recco." https://www.recco.com. Accessed: November 14, 2023.

[18] D. Milanesio, M. Saccani, R. Maggiora, D. Laurino, and M. Porporato, "Design of an harmonic radar for the tracking of the asian yellow-legged hornet," *Ecology and Evolution*, vol. 6, pp. 2170–2178, Mar. 2016.

[19] C. Ju and H. Son, "Autonomous tracking of micro-sized flying insects using uav: A preliminary results," *Journal of the Korean Society of Industry Convergence*, vol. 23, pp. 125–137, 2020.

[20] M. E. O'Neal, D. A. Landis, E. Rothwell, L. Kempel, and D. Reinhard, "Tracking Insects with Harmonic Radar: a Case Study," *American Entomologist*, vol. 50, pp. 212–218, 10 2004.

[21] H. M. Aumann and N. W. Emanetoglu, "A wideband harmonic radar for tracking small wood frogs," in *2014 IEEE Radar Conference*, (Cincinnati, OH, USA), pp. 0108–0111, 2014.

[22] G. J. Mazzaro, A. F. Martone, and D. M. McNamara, "Detection of RF electronics by multitone harmonic radar," *IEEE Transactions on Aerospace and Electronic Systems*, vol. 50, no. 1, pp. 477–490, 2014.

[23] Z.-M. Tsai, P.-H. Jau, N.-C. Kuo, J.-C. Kao, K.-Y. Lin, F.-R. Chang, E.-C. Yang, and H. Wang, "A high-range-accuracy and high-sensitivity harmonic radar using pulse pseudorandom code for bee searching," *IEEE Transactions on Microwave Theory and Techniques*, vol. 61, pp. 666–675, Jan. 2013.

[24] B. Colpitts, D. Luke, and G. Boiteau, "Harmonic radar for insect flight pattern tracking," in *2000 Canadian Conference on Electrical and Computer Engineer-*

ing. Conference Proceedings. Navigating to a New Era (Cat. No.00TH8492), vol. 1, pp. 302–306 vol.1, 2000.

[25] M. Skolnik, *Radar Handbook, Third Edition*. Electronics electrical engineering, McGraw-Hill Education, 2008.

[26] O. Guillaume, A. Coulon, J.-f. Le Galliard, and J. Clobert, "Animal-borne sensors to study the demography and behavior of small species," in *Sensors for Ecology: Towards Integrated Knowledge of Ecosystems* (J.-F. L. Galliard, J.-M. Guarini, and F. Gaill, eds.), pp. 43–61 p., CNRS, 2012.

[27] S. Hansen, C. Bredendiek, and N. Pohl, "Active reflector tag for millimeter wave harmonic radar at 61/122 ghz ism band based on 130 nm-bicmos sige:c technology," in *2020 IEEE/MTT-S International Microwave Symposium (IMS)*, (Los Angeles, CA, USA), pp. 611–614, 2020.

[28] K. Rasilainen, J. Ilvonen, A. Lehtovuori, J.-M. Hannula, and V. Viikari, "Harmonic transponders: Performance and challenges," *Progress in Electromagnetics Research M*, vol. 41, pp. 139–147, 2015.

[29] A. Lavrenko, B. Litchfield, G. Woodward, and S. Pawson, "Design and evaluation of a compact harmonic transponder for insect tracking," *IEEE Microwave and Wireless Components Letters*, vol. 30, pp. 445–448, Apr. 2020.

[30] V. Palazzi, L. Roselli, M. M. Tentzeris, P. Mezzanotte, and F. Alimenti, "Energy-efficient harmonic transponder based on on-off keying modulation for both identification and sensing," *Sensors*, vol. 22, p. 620, Jan. 2022.

[31] D. Psychoudakis, W. Moulder, C.-C. Chen, H. Zhu, and J. L. Volakis, "A portable low-power harmonic radar system and conformal tag for insect tracking," *IEEE Antennas and Wireless Propagation Letters*, vol. 7, pp. 444–447, 2008.

[32] K. Rasilainen, J. Ilvonen, and V. Viikari, "Antenna matching at harmonic frequencies to complex load impedance," *IEEE Antennas and Wireless Propagation Letters*, vol. 14, pp. 535–538, 2015.

[33] Z. Ye, Y. Ling, M. Yang, Y. Xu, L. Zhu, Z. Yan, and P.-Y. Chen, "A breathable, reusable, and zero-power smart face mask for wireless cough and mask-wearing monitoring," *ACS Nano*, vol. 16, no. 4, pp. 5874–5884, 2022. PMID: 35298138.

[34] B. Colpitts and G. Boiteau, "Harmonic radar transceiver design: Miniature tags for insect tracking," *IEEE Transactions on Antennas and Propagation*, vol. 52, pp. 2825–2832, Nov. 2004.

[35] A. S. Sedra and K. C. Smith, *Microelectronic Circuits*. New York, NY: Oxford University Press, 8th ed., 2014.

[36] C. A. Balanis, *Antenna Theory: Analysis and Design*. Hoboken, NJ: Wiley, 4th ed., 2016.

[37] K. Rasilainen and V. V. Viikari, "Transponder designs for harmonic radar applications," *International Journal of Antennas and Propagation*, vol. 2015, pp. 1–9, 2015.

[38] J.-M. Hannula, K. Rasilainen, and V. Viikari, "Characterization of transponder antennas using intermodulation response," *IEEE Transactions on Antennas and Propagation*, vol. 63, no. 6, pp. 2412–2420, 2015.

[39] O. M. Bucci, A. de Bonitatibus, and I. Pinto, "Harmonic radar cross-section of bistatic nonlinear responder," *Alta Frequenza*, vol. 53, pp. 172–176, June 1984.

[40] V. V. Belyaev, A. T. Mayunov, and S. N. Razin'kov, "Improving the accuracy of experimental prediction of the detectability of nonlinear objects by radar," *Measurement Techniques*, vol. 42, pp. 1068–1074, Nov. 1999.

[41] X. Gu, S. Hemour, and K. Wu, "Improving conversion loss performance of fully passive harmonic transponder at low temperature," in *2019 IEEE Wireless Power Transfer Conference (WPTC)*, (London, UK), pp. 395–398, 2019.

[42] N. Alkhaldi, "Design and practical implementation of harmonic-transponder sensors." Ph.D. thesis, Wayne State University, 2019.

[43] D. Dardari, "Detection and accurate localization of harmonic chipless tags," *EURASIP Journal on Advances in Signal Processing*, vol. 2015, Aug. 2015.

[44] M.-L. Hsu, T.-H. Liu, T.-C. Yang, H.-C. Jhan, H. Wang, F.-R. Chang, K.-Y. Lin, E.-C. Yang, and Z.-M. Tsai, "Bee searching radar with high transmit–receive isolation using pulse pseudorandom code," *IEEE Transactions on Microwave Theory and Techniques*, vol. 64, no. 12, pp. 4324–4335, 2016.

[45] A. Lavrenko, Z. Barry, R. Norman, C. Frazer, Y. Ma, G. Woodward, and S. Pawson, "Autonomous swarm of uavs for tracking of flying insects with harmonic radar," in *2021 IEEE 93rd Vehicular Technology Conference (VTC2021-Spring)*, (Helsinki, Finland), pp. 1–5, 2021.

[46] J. Chapman, D. Reynolds, and A. Smith, "Migratory and foraging movements in beneficial insects: A review of radar monitoring and tracking methods," *International Journal of Pest Management*, vol. 50, no. 3, pp. 225–232, 2004.

[47] A. Mishra, J. Wang, D. Rodriguez, and C. Li, "Utilizing passive intermodulation response of frequency-modulated continuous-wave signal for target identification and mapping," *IEEE Sensors Journal*, vol. 21, no. 16, pp. 17817–17826, 2021.

[48] E. Cant, A. Smith, D. Reynolds, and J. Osborne, "Tracking butterfly flight paths across the landscape with harmonic radar," *Proceedings of the Royal Society B: Biological Sciences*, vol. 272, pp. 785–790, Apr. 2005.

[49] S. Lioy, D. Laurino, R. Maggiora, D. Milanesio, M. Saccani, P. J. Mazzoglio, A. Manino, and M. Porporato, "Tracking the invasive hornet vespa velutina in complex environments by means of a harmonic radar," *Scientific Reports*, vol. 11, June 2021.

[50] E. A. Capaldi, A. D. Smith, J. L. Osborne, S. E. Fahrbach, S. M. Farris, D. R. Reynolds, A. S. Edwards, A. Martin, G. E. Robinson, G. M. Poppy, and J. R. Riley, "Ontogeny of orientation flight in the honeybee revealed by harmonic radar," *Nature*, vol. 403, pp. 537–540, Feb. 2000.

[51] N. D. Miller, T. J. Yoder, N. C. Manoukis, L. A. F. N. Carvalho, and M. S. Siderhurst, "Harmonic radar tracking of individual melon flies, zeugodacus cucurbitae, in Hawaii: Determining movement parameters in cage and field settings," *PLOS ONE*, vol. 17, p. e0276987, Nov. 2022.

[52] F. Meloche and P. Albert, "A lighter transponder for harmonic radar," in *2006 European Radar Conference*, (Manchester, UK), pp. 233–236, IEEE, Sept. 2006.

[53] J. Kiriazi, J. Nakakura, K. Hall, N. Hafner, and V. Lubecke, "Low profile harmonic radar transponder for tracking small endangered species," in *2007 29th Annual International Conference of the IEEE Engineering in Medicine and Biology Society*, (Lyon, France), pp. 2338–2341, IEEE, Aug. 2007.

[54] K. Rasilainen, J. Ilvonen, A. Lehtovuori, J.-M. Hannula, and V. Viikari, "On design and evaluation of harmonic transponders," *IEEE Transactions on Antennas and Propagation*, vol. 63, pp. 15–23, Jan. 2015.

[55] X. Gu, N. N. Srinaga, L. Guo, S. Hemour, and K. Wu, "Diplexer-based fully passive harmonic transponder for sub-6-GHz 5g-compatible IoT applications," *IEEE Transactions on Microwave Theory and Techniques*, vol. 67, pp. 1675–1687, May 2019.

[56] A. Lavrenko and J. Cavers, "Two-region model for harmonic radar transponders," *Electronics Letters*, vol. 56, pp. 835–838, Aug. 2020.

[57] H. Aumann, E. Kus, B. Cline, and N. W. Emanetoglu, "An asymmetrical dipole tag with optimum harmonic conversion efficiency," in *Proceedings of the 2012 IEEE International Symposium on Antennas and Propagation*, (Chicago, IL), IEEE, July 2012.

[58] M. Ritamaki, A. Ruhanen, V. Kukko, J. Miettinen, and L. Turner, "Contactless radiation pattern measurement method for UHF RFID transponders," *Electronics Letters*, vol. 41, no. 13, p. 723, 2005.

[59] H. Aniktar, D. Baran, E. Karav, E. Akkaya, Y. S. Birecik, and M. Sezgin, "Getting the bugs out: A portable harmonic radar system for electronic countersurveillance applications," *IEEE Microwave Magazine*, vol. 16, no. 10, pp. 40–52, 2015.

[60] T. Aballo, L. Cabria, J. A. Garcia, T. Fernandez, and F. Marante, "Taking advantage of a schottky junction nonlinear characteristic for radiofrequency temperature sensing," in *2006 European Microwave Conference*, (Manchester, UK), pp. 318–321, 2006.

[61] L. Chioukh, H. Boutayeb, D. Deslandes, and K. Wu, "Noise and sensitivity of harmonic radar architecture for remote sensing and detection of vital signs," *IEEE Transactions on Microwave Theory and Techniques*, vol. 62, no. 9, pp. 1847–1855, 2014.

[62] L. Zhu, T. D. Hà, Y.-H. Chen, H. Huang, and P.-Y. Chen, "A passive smart face mask for wireless cough monitoring: A harmonic detection scheme with clutter rejection," *IEEE Transactions on Biomedical Circuits and Systems*, vol. 16, no. 1, pp. 129–137, 2022.

[63] V. Viikari, M. Kantanen, T. Varpula, A. Lamminen, A. Alastalo, T. Mattila, H. Seppa, P. Pursula, J. Saebboe, S. Cheng, M. Al-Nuaimi, P. Hallbjorner, and A. Rydberg, "Technical solutions for automotive intermodulation radar for detecting vulnerable road users," in *VTC Spring 2009 - IEEE 69th Vehicular Technology Conference*, (Barcelona, Spain), pp. 1–5, 2009.

[64] J. A. Kosinski, W. D. Palmer, and M. B. Steer, "Unified understanding of RF remote probing," *IEEE Sensors Journal*, vol. 11, no. 12, pp. 3055–3063, 2011.

[65] G. J. Mazzaro, A. F. Martone, K. I. Ranney, and R. M. Narayanan, "Nonlinear radar for finding rf electronics: System design and recent advancements," *IEEE Transactions on Microwave Theory and Techniques*, vol. 65, no. 5, pp. 1716–1726, 2017.

[66] Z. Ye, M. Yang, Y. Ren, C.-H. J. Hung, C.-T. M. Wu, and P.-Y. Chen, "Review on recent advances and applications of passive harmonic RFID systems," *IEEE Journal of Radio Frequency Identification*, vol. 7, pp. 118–133, 2023.

[67] P. V. Nikitin and K. V. S. Rao, "Harmonic scattering from passive UHF RFID tags," in *2009 IEEE Antennas and Propagation Society International Symposium*, (North Charleston, SC, USA), pp. 1–4, 2009.

[68] K. Wincza, S. Gruszczynski, and J. Borgosz, "Dual-band capacitive feed antenna for nonlinear junction detection device," in *2008 14th Conference on Microwave Techniques*, (Prague, Czech Republic), pp. 1–4, 2008.

[69] B. Kubina, J. Romeu, C. Mandel, M. Schüßler, and R. Jakoby, "Design of a quasi-chipless harmonic radar sensor for ambient temperature sensing," in *SENSORS, 2014 IEEE*, (Valencia, Spain), pp. 1567–1570, 2014.

[70] X. Gao, A. Singh, O. Boric-Lubecke, and V. M. Lubecke, "Small-scale displacement measurement with passive harmonic rf tag using doppler radar," in

2013 IEEE International Wireless Symposium (IWS), (Beijing, China), pp. 1–4, 2013.

[71] A. Kumar and A. Lavrenko, "Compact folded meander-line harmonic tag antenna for insect tracking," in *2023 17th European Conference on Antennas and Propagation (EuCAP)*, (Florence, Italy), pp. 1–5, 2023.

[72] U. Olgun, D. Psychoudakis, C.-C. Chen, and J. L. Volakis, "High gain lightweight array for harmonic portable RFID radar," in *2009 IEEE Antennas and Propagation Society International Symposium*, (North Charleston, SC, USA), pp. 1–4, 2009.

[73] P.-H. Jau, Z.-M. Tsai, N.-C. Kuo, J.-C. Kao, K.-Y. Lin, F.-R. Chang, E.-C. Yang, and H. Wang, "Signal processing for harmonic pulse radar based on spread spectrum technology," *IET Radar, Sonar & Navigation*, vol. 8, no. 3, pp. 242–250, 2014.

[74] O. Hüppop, M. Ciach, R. Diehl, D. R. Reynolds, P. M. Stepanian, and M. H. M. Menz, "Perspectives and challenges for the use of radar in biological conservation," *Ecography*, vol. 42, no. 5, pp. 912–930, 2019.

[75] M. S. Binetti, C. Campanale, C. Massarelli, and V. F. Uricchio, "The use of weather radar data: Possibilities, challenges and advanced applications," *Earth*, vol. 3, pp. 157–171, Feb. 2022.

[76] International Telecommunication Union (ITU), "Radio Regulations," 2020.

[77] L. Zhu, H. Huang, M. M.-C. Cheng, and P.-Y. Chen, "Compact, flexible harmonic transponder sensor with multiplexed sensing capabilities for rapid, contactless microfluidic diagnosis," *IEEE Transactions on Microwave Theory and Techniques*, vol. 68, no. 11, pp. 4846–4854, 2020.

[78] S. Karuppuswami, M. I. M. Ghazali, A. Kaur, and P. Chahal, "Multi-band harmonic rf tags for barcode applications in a cluttered environment," in *2017 IEEE 67th Electronic Components and Technology Conference (ECTC)*, (Orlando, FL, USA), pp. 1861–1867, 2017.

[79] C. Hilton and J. A. Nanzer, "Narrowband passive rf tags for frequency-selective harmonic doppler radar tracking," *IEEE Transactions on Antennas and Propagation*, vol. 71, no. 2, pp. 1216–1222, 2023.

[80] M. Ivanou and V. Chertkov, "Nonlinear junction locator with the possibility of identifying nonlinear objects," in *Proc. 6th Mater. Junior Res. Conf.*, pp. 134–137, Apr. 2014.

[81] F. Alimenti and L. Roselli, "Theory of zero-power RFID sensors based on harmonic generation and orthogonally polarized antennas," *Progress In Electromagnetics Research*, vol. 134, pp. 337+, February 2013.

[82] R. D. Brazee, E. S. Miller, M. E. Reding, M. G. Klein, B. Nudd, and H. Zhu, "A transponder for harmonic radar tracking of the black vine weevil in behavioral research," *Transactions of the ASAE*, vol. 48, no. 2, pp. 831–838, 2005.

[83] L. Rong and W. Hai-yong, "The re-radiation characteristics of nonlinear target in harmonic radar detection," in *2008 China-Japan Joint Microwave Conference*, (Shanghai, China), pp. 661–664, 2008.

[84] J.-W. Kim, K.-S. Min, I.-H. Kim, and C.-J. Park, "Triple band spiral antenna for non-linear junction detector," in *2012 International Symposium on Antennas and Propagation (ISAP)*, (Nagoya, Japan), pp. 802–805, 2012.

[85] B. Razavi, *RF Microelectronics*. Pearson Education, 2011.

[86] X. Gu, W. Lin, S. Hemour, and K. Wu, "Readout distance enhancement of battery-free harmonic transponder," *IEEE Transactions on Microwave Theory and Techniques*, vol. 69, no. 7, pp. 3413–3424, 2021.

[87] Y. Jiang, X. Gu, and C. Cui, "A design method of harmonic mixers based on schottky diodes applied for millimeter wave components," *Radio Science*, vol. 57, no. 3, p. e2021RS007359, 2022. e2021RS007359 2021RS007359.

[88] C.-H. Hsieh, T.-C. Hong, C.-Y. Yang, Y.-H. Chen, X.-R. Yu, W.-H. Lu, R. W. Chuang, Z.-M. Tsai, Y.-J. Lee, Y. Li, W.-F. Wu, T.-S. Chao, S. Samukawa, Y.-H. Wang, W.-K. Yeh, and J.-H. Tarng, "A Harmonic Radar Tag With High Detection Range Utilizing Ge FinFETs CMOS Technology," *IEEE Electron Device Letters*, vol. 43, no. 11, pp. 1798–1801, 2022.

[89] M. Yang, Z. Ye, C.-H. Sun, L. Zhu, M. Hajizadegan, and P.-Y. Chen, "A lightweight, zero-power intermodulation sensor based on the graphene oscillator," *IEEE Sensors Journal*, vol. 23, no. 3, pp. 3243–3250, 2023.

[90] D. Milanesio, M. Saccani, R. Maggiora, D. Laurino, and M. Porporato, "Recent upgrades of the harmonic radar for the tracking of the asian yellow-legged hornet," *Ecology and Evolution*, vol. 7, pp. 4599–4606, May 2017.

[91] H.-D. Chen and Y.-H. Tsao, "Broadband capacitively coupled patch antenna for RFID tag mountable on metallic objects," *IEEE Antennas and Wireless Propagation Letters*, vol. 9, pp. 489–492, 2010.

[92] S. A. McCormick, "Simulation comparisons of three different meander line dipoles," tech. rep., Defense Technical Information Center, Jan. 2015.

[93] K. Rasilainen and V. Viikari, "Effect of shape and surroundings on harmonic transponder performance," in *2016 10th European Conference on Antennas and Propagation (EuCAP)*, (Davos, Switzerland), pp. 1–5, 2016.

[94] G. Storz and A. Lavrenko, "Compact low-cost FMCW harmonic radar for short range insect tracking," in *2020 IEEE International Radar Conference (RADAR)*, (Washington, DC, USA), pp. 642–647, IEEE, Apr. 2020.

[95] K. Rasilainen, J. Ilvonen, J.-M. Hannula, and V. Viikari, "Designing harmonic transponders using lumped-component matching circuits," *IEEE Antennas and Wireless Propagation Letters*, vol. 16, pp. 246–249, 2017.

[96] J. Riley and A. Smith, "Design considerations for an harmonic radar to investigate the flight of insects at low altitude," *Computers and Electronics in Agriculture*, vol. 35, pp. 151–169, Aug. 2002.

[97] "Copper Magnet Wire Data." https://mwswire.com/wp-content/uploads/2016/11/Resistance-Copper-Wires.pdf. Accessed: November 14, 2023.

[98] M. A. Merlini, A. G. B. Colpitts, S. Gill, B. G. Colpitts, and B. R. Petersen, "Channel modelling and efficient time-domain simulation of a harmonic transponder tag," in *Proceedings of the 6th International Conference on Telecommunications and Remote Sensing*, (Delft, Netherlands), ACM, Nov. 2017.

[99] M. Polívka and J. Frolík, "Characterizing harmonic transponder performance jointly over frequency and power," in *2023 17th European Conference on Antennas and Propagation (EuCAP)*, (Florence, Italy), pp. 1–5, 2023.

[100] A. Liaw and M. Wiener, "Classification and regression by randomforest," *R News*, vol. 2, no. 3, pp. 18–22, 2002.

Appendix A

Design of Experiment:

Implementing R Code

```
# Add libraries
library(randomForest)
library(ggplot2)
# Read the CSV file
dataset1 <- read.csv("final.csv", header = TRUE)

# Assign new column names
new_names <- c("Cp", "Ls", "Rs", "Is", "Vj", "Cj0",
"ConversionLoss")  # Replace with your desired column names
colnames(dataset1) <- new_names

model <- randomForest(ConversionLoss~., dataset1)

# Calculate variable importance using the importance() function:
var_importance <- importance(model)
```

```
# Scale the values of variable importance between 0 and 1
scaled_importance <- 100*var_importance/sum(var_importance)
# Print the scaled importance values
print(scaled_importance)

# Calculate variable importance using the importance() function
var_importance <- importance(model)

# Scale the values of variable importance between 0 and 1
scaled_importance <- 100*var_importance/sum(var_importance)

# Print the scaled importance values
print(scaled_importance)

# Convert the scaled importance values to a data frame
importance_df <- data.frame(variable = rownames(scaled_importance),\
importance = scaled_importance)

# Create a bar plot with adjusted plot dimensions
ggplot(importance_df, aes(x = variable, y = IncNodePurity)) +
  geom_bar(stat = "identity", fill = "steelblue", size = 35) +
  labs(x = NULL, y = "Scaled Importance") + theme_minimal() +
  theme(axis.text.x = element_text(face = "bold.italic", size = 15),\
  axis.text.y = element_text(face = "bold.italic", size = 15))
```

Vita

Candidate's full name: Ramin Ala

University attended:
University of Isfahan, B.Sc., 2007
K. N. Toosi University of Technology, M.Sc., 2010

Journal Publication:

1. R. Ala, C. D. Rouse and B. G. Colpitts, "An Extra Low-Mass Harmonic Radar Transponder for Insect Tracking Applications," in *IEEE Transactions on Radar Systems*, vol. 1, pp. 146-154, 2023, doi: 10.1109/TRS.2023.3286270.

Conference Publications:

2. R. Ala, B. G. Colpitts and N. Kozma, "Evaluation and improvement of the performance of harmonic RADAR transponders," *2020 IEEE International Radar Conference (RADAR)*, Washington, DC, USA, 2020, pp. 659-664, doi: 10.1109/RADAR42522.2020.9114545.

3. R. Ala and B. G. Colpitts, "Development of extra low mass harmonic radar transponders," *2021 IEEE 19th International Symposium on Antenna Technology and Applied Electromagnetics (ANTEM)*, Winnipeg, MB, Canada, 2021, pp. 1-2, doi: 10.1109/ANTEM51107.2021.9518747.